Title: Graphitic Carbon Nitride Quantum Dots (g-C3N4 QDs): From Chemistry to Applications

Authors: Mohammed Majdoub, PhD; Dineshkumar Sengottuvelu, PhD; Sasan Nouranian; Ahmed Al-Ostaz, PhD

To be cited as: 10.1002/cssc.202301462

Link to VoR: https://doi.org/10.1002/cssc.202301462

Graphitic Carbon Nitride Quantum Dots (g-C_3N_4 QDs): From Chemistry to Applications

Mohammed Majdoub[‡a*], Dineshkumar Sengottuvelu[‡a*], Sasan Nouranian[ab], Ahmed Al-Ostaz[ac]

[a] Center for Graphene Research and Innovation, University of Mississippi, University, MS 38677, United States

[b] Department of Chemical Engineering, University of Mississippi, University, MS 38677, United States

[c] Department of Civil Engineering, University of Mississippi, University, MS 38677, United States

*Corresponding authors: mmajdoub@olemiss.edu , dsengott@olemiss.edu

‡Equal Contribution in this work

Graphical Abstract

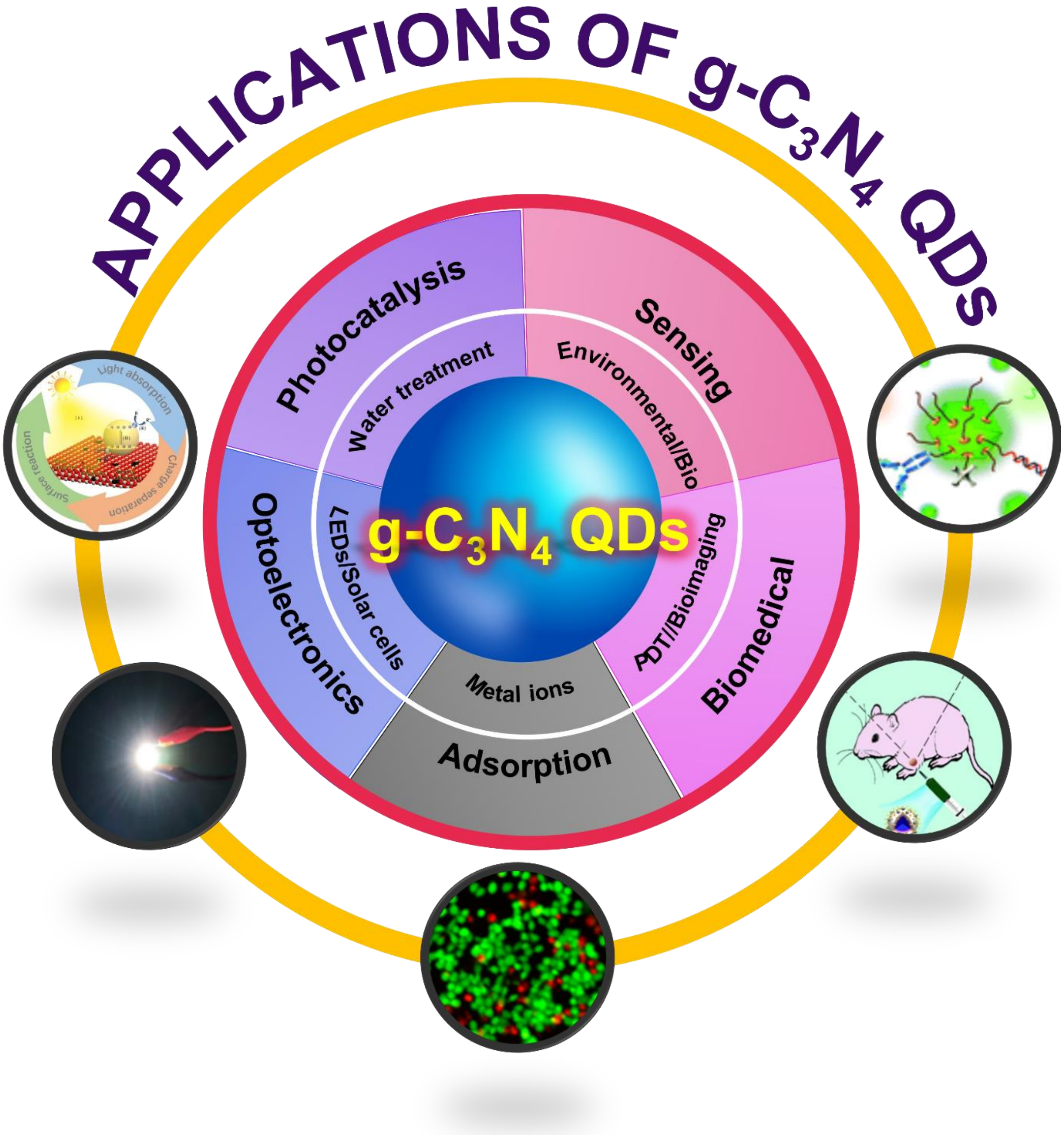

Contents/Outline

Abstract

Since their emergence in 2014, graphitic carbon nitride quantum dots (g-C_3N_4 QDs) have attracted much interest from the scientific community due to their distinctive physicochemical features, including structural, morphological, electrochemical, and optoelectronic properties. Owing to their desirable characteristics, such as non-zero band gap, ability to be chemically functionalized or doped, possessing tunable properties, outstanding dispersibility in different media, and biocompatibility, g-C_3N_4 QDs have shown promise for photocatalysis, energy devices, sensing, bioimaging, solar cells, optoelectronics, among other applications. As these fields are rapidly evolving, it is very strenuous to pinpoint the emerging challenges of the g-C_3N_4 QDs development and application during the last decade, mainly due to the lack of critical reviews of the innovations in the g-C_3N_4 QDs synthesis pathways and domains of application. Herein, an extensive survey is conducted on the g-C_3N_4 QDs synthesis, characterization, and applications. Scenarios for the future development of g-C_3N_4 QDs and their potential applications are highlighted and discussed in detail. The provided critical section suggests a myriad of opportunities for g-C_3N_4 QDs, especially for their synthesis and functionalization, where a combination of eco-friendly/single step synthesis and chemical modification may be used to prepare g-C_3N_4 QDs with, for example, enhanced photoluminescence and production yields.

Keywords: g-C_3N_4 QDs, sensing, bioimaging, solar cells, optoelectronics

1. Introduction

The phenomenal growth of industrial sectors over the course of the last several decades has exerted a great amount of pressure on sustainability and the environment. In this day and age of rapidly advancing technology, sustainability has emerged as an important factor that has an impact on both academic and industrial spheres. As a result, it is serving as a guiding principle in a wide variety of fields of research, including optoelectronics, biomedical, photochemistry, energy harvesting, and many others [1–6]. Combining the abundant solar light with the technologies that are currently available via the use of photoinduced materials, is an essential direction. In this regard, semiconductors (TiO_2, CdS, CdSe, CdTe, PbTe, perovskite, etc.) are among those that are considered to be interesting candidates as photomediated materials in the fields of photocatalysis, optoelectronics, photovoltaic instruments, transistors, and other related fields [7–14]. These materials absorb light, which results in the formation of excited electrons. The essential and important characteristics of a semiconductor material are its appropriate band gap and absorption range, stimulated electron lifetimes, and charge migration that delays recombination. In spite of the significant amount of work that has been invested in the development of these types of materials, their use in a wide variety of applications has been hampered by a number of drawbacks. These drawbacks are primarily attributable to the fact that the metal content of these materials causes toxicity issues, as well as the fact that their synthesis requires scarce and finite resources [15]. As a result, it is necessary to look for alternative candidate materials that have features comparable to or even better than those of the original material, but can be manufactured using more environmentally friendly synthetic methods [16].

From this perspective, carbon nitrides (C_3N_4) have attracted a significant amount of interest from researchers over the course of the last decade. These compounds are polymeric-based product that is mostly composed of carbon and nitrogen atoms [17]. Back in 1834, Liebig [18] was able to describe the creation of a linear polymer that consisted of linked tri-s-triazine units through secondary nitrogen atoms and labeled it "melon." This event is considered to be the beginning of the history of carbon nitrides. However, the incredible potential of this polymer-like material with a mysterious origin wasn't completely recognized until recent years. This was mainly due to the features of the material, which include its insolubility in a variety of mediums, chemical inertness, stability, and the fact that its structure is unknown. Teter and Hemley [19] did not come up with their five different structures of C_3N_4 until 1996. These structures are referred to as α-, β-, cubic-, pseudocubic-, and graphitic-C_3N_4 (g-C_3N_4). Following that, many other structures of g-C_3N_4 were investigated, including s-triazine, triazines, and heptazine (tri-s-triazine). Importantly, experimental and theoretical investigations found that the tri-s-triazine-based g-C_3N_4 was around 30 kJ mol^{-1} more stable than the s-triazine-based one, confirming the fact that these units are the most often acknowledged for single layer g-C_3N_4 [20,21]. Many metal-free nitrogen-rich precursors including urea [22,23], thiourea [24,25], cyanamide,[26] dicyandiamide [27,28], and melamine [29–31] are used to synthesize 2D stacked g-C_3N_4. Thermal condensation under air or inert environment at 450-650 °C is most prevalent [32–34]. Nonetheless, the precursor and thermal treatment may greatly impact the obtained physicochemical characteristics of the resulting g-C_3N_4, giving rise to a family of materials with customized traits such as porosity, light absorption, photoluminescence, surface charge, band gap, and so on [35–37].

The practical applications of bulk stacked g-C_3N_4 in a variety of optoelectronic, biomedical, and photocatalytic fields are hindered by a number of drawbacks, including a low specific surface area and a poor quantum yield. To overcome these shortcomings, a significant amount of work has been put towards either manipulating the nanostructure/nanomorphology of bulk g-C_3N_4 (nanosheets, nanotubes, nanorods, wires, prisms, hollow spheres, etc.), or hetero-/metal-atoms doping into bulk g-C_3N_4 [38–46]. Due to the fact that strong quantum confinement and edge effects can occur with such a small size, unusual optical and electronic properties can be induced when the size of the bulk g-C_3N_4 is brought down to 10 nm, resulting in quantum dots (QDs) with quantum confinement phenomenon [47]. Furthermore, g-C_3N_4 QDs have wider band gap and distinctive photophysical traits and photoexcited charge carriers than bulk g-C_3N_4 [48]. Hence, g-C_3N_4 QDs are used for a wide array of domains, including photocatalysis, biomedical, optoelectronics, sensing, and so forth [49–54].

g-C_3N_4 QDs are one of the youthful icons of the carbon family. Since its emergence in 2014 [47], g-C_3N_4 QDs have attracted great interest from the scientific community, owing to their distinctive physicochemical features including structural, morphological, electrochemical, and optoelectronic properties. Offering numerous characteristics such as non-zero band gap, ability to be chemically functionalized/doped, highly tunable properties, outstanding dispersibility, and biocompatibility, g-C_3N_4 QDs seems to be great nominees for a wide array of applications. In comparison with the common carbon-based QDs, g-C_3N_4 QDs are proprietary of electron-rich features, basic surface moieties, and H-bonding motifs owing to the existing N and H atoms.

Hence, they are regarded as interesting nominees to further complement carbon-based QDs in functional materials applications. Because of the prominent quantum confinement and edge effects, the optical and physical characteristics of g-C_3N_4 QDs are distinct from those of other members of the carbon materials family. For example, compared with carbon nanodots and graphene QDs, g-C_3N_4 QDs display noteworthy photoluminescence (PL) quantum yields. Thus, they have become promising alternative materials on the account of their distinctive electrical and optical traits [55–57]. Other significant distinctions include a non-zero bandgap as a consequence of the quantum confinement, excellent dispersibility as a consequence of the large edge effect and amphiphilic nature, and highly tunable chemical and physical properties. These distinctions, along with others, have contributed to the creation of clear boundaries between the applications of bulk g-C_3N_4 and g-C_3N_4 QDs [58]. These characteristics, in addition to biocompatibility, low toxicity, chemical stability, size similarity to biomolecules, steady photoluminescence, and high surface grafting, provide some distinctive benefits and, hence, hold promise for potential applications. Because of their exceptional properties, g-C_3N_4 QDs have the potential to be designed into high-performance electronic, photonic, and energy-related devices. Some examples of these devices include, but are not limited to, solar cells, photodetectors, light-emitting diodes (LEDs), and supercapacitors [59–63]. g-C_3N_4 QDs have also shown to have various applications in the disciplines of biomedical engineering, catalysis, sensing, nano-additives, and so forth [53,64–67].

Up to now, more than 10000 articles have been published containing the keyword graphitic carbon nitride "g-C_3N_4" (04/10/2023, from Scopus abstract and citation database and "g-C_3N_4" was used as keyword in the Scopus search engine). In addition to this enormous production, researchers around the world produced up to the writing of these sentences over +300 reviews (04/10/2023, from Scopus abstract and citation database and "g-C_3N_4" was used as keyword in the Scopus search engine). However, articles which target the "g-C_3N_4 QDs development and usage in a broad range of technological fields" have built at least 8% to 10% of the present scientific production in terms of research articles, and practically <0.1% in terms of reviews. For this reason, the development and discussion of this important aspect of the g-C_3N_4 bibliography would be a huge addition and a necessity for the development of this field of research. As this domain continues to expand at a rapid rate, reviews and surveys on the most recent advancements in many facets of g-C_3N_4 QDs are much needed. In this respect, there is an immediate demand for a timely, thorough, and in-depth review on the latest fulfillments of g-C_3N_4 QDs, which hold a great potential as interesting 0D carbon-based materials in a wide range of applications. For instance, Wang et al. [49] published a review on the different synthesis pathways of g-C_3N_4 QDs and their direct use as photocatalyst for organic pollutant degradation. Similarly, Goren et al. [64] also reported a review on the environmental aspects of g-C_3N_4 QDs by describing their utilization for hazardous contaminant degradation in wastewater by photodegradation.

In this review, the comprehensive/extensive survey is conducted on the g-C_3N_4 QDs development, characteristics, and field of applications, providing a steady and comparative discourse **(Fig. 1)**. The broad field of g-C_3N_4 QDs utilization in optoelectronics, sensing, biomedical, and photocatalysis is extensively discussed. Furthermore, scenarios for future development of g-C_3N_4 QDs and future insights of their application are highlighted and discussed in detail. The summary and outlook given in this survey refers to the unlimited research opportunities in g-C_3N_4 QDs, especially in synthesis and functionalization approaches where eco-friendly/single step synthesis and chemical modifiers can be used to prepare g-C_3N_4 QDs with enhanced photoluminescence quantum and production yields. We believe that this paper will inspire readers to conduct research with the aim of exploring new synthesis and functionalization strategies for this 0D carbon-based material in a wide range of applications.

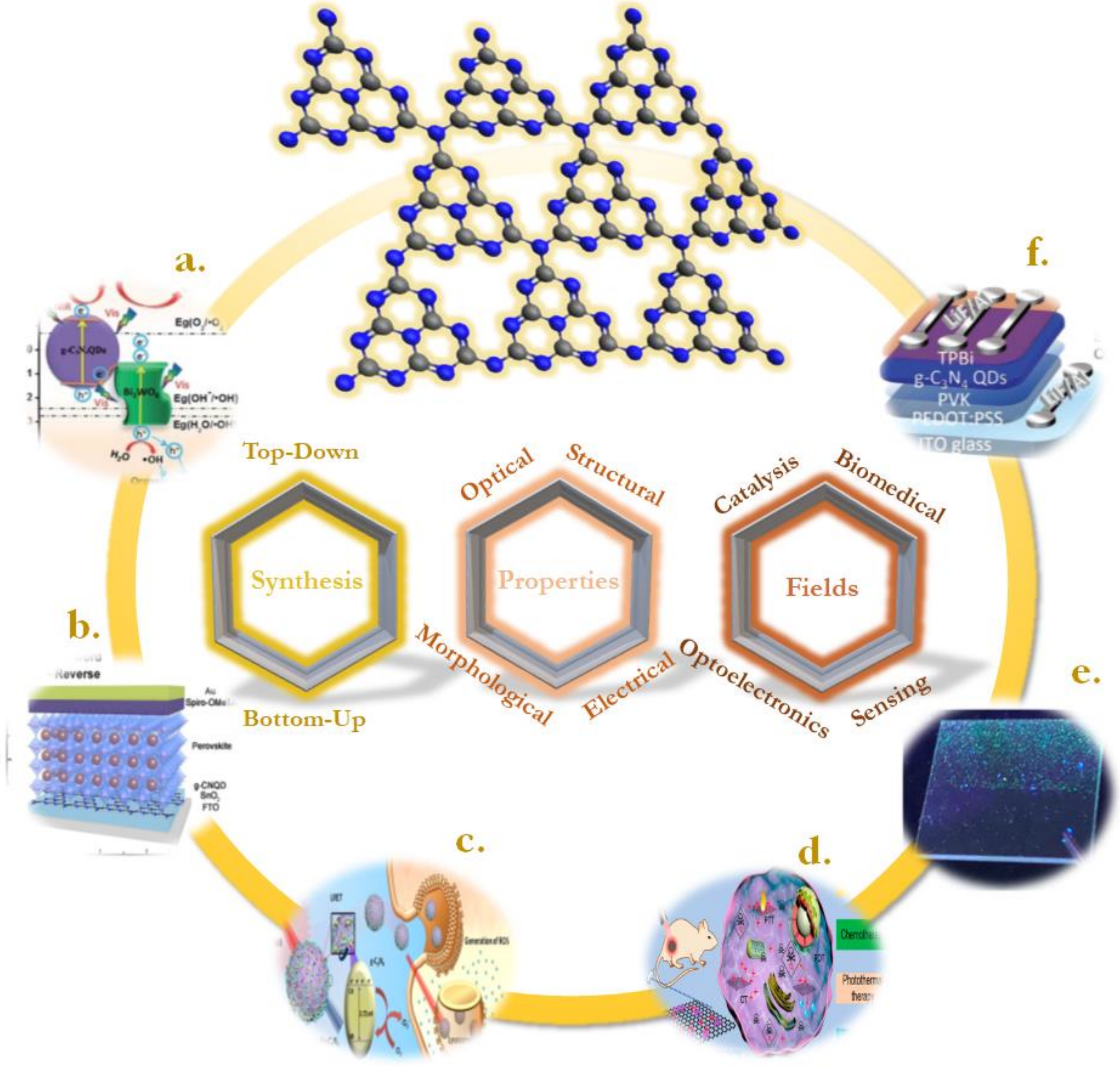

Fig. 1. Illustration of the g-C_3N_4 research overview. a) Photocatalysis, Reproduced with permission from [68]. b) Photodetector and solar cells, Reproduced with permission from [63]. c) Photodynamic Therapy, Reproduced with permission from [69]. d) Photo-Chemotherapy, Reproduced with permission from [70]. e) Optoelectronic films, Reproduced with permission from [51]. f) Quantum dot light-emitting diode (QLED), Reproduced with permission from [71].

2. Synthesis pathways of g-C_3N_4 QDs

Matching the carbon- and graphene-based QDs, the synthesis routes of g-C_3N_4 can be immediately recognized and classified into two major approaches. These routes are referred to as top-down and bottom-up strategies. When using the top-down strategy, the synthesis of g-C_3N_4 QDs begins with the production of macroscopic g-C_3N_4 structures (bulk) using thermal polymerization (calcination) of low-cost, accessible, N-rich, and O-rich precursors such as urea [22,23], thiourea [24,25], cyanamide [26], dicyandiamide [27,28], and melamine [29–31] (**Fig. 2**). This is then followed by a number of treatments, such as hydrothermal treatment [47,72–74][75–84], evaporation-condensation/hydrolysis techniques [48,85], and ultrasonication [53,86–96]. to produce two-dimensional nanosheets, one-dimensional nanowires or nanoribbons, and finally zero-dimensional quantum dots (QDs). For the bottom-up approach, g-C_3N_4 QDs may be produced using microwave-aided solvothermal route [97–109], solid-phase reactions [58,69,110–117], or chemical vapor deposition (CVD) [60,65,118]. The most widely used precursors are urea or thiourea as N-containing compounds. On the other hand, glucose, sucrose, or citric acid are used as the C-source.

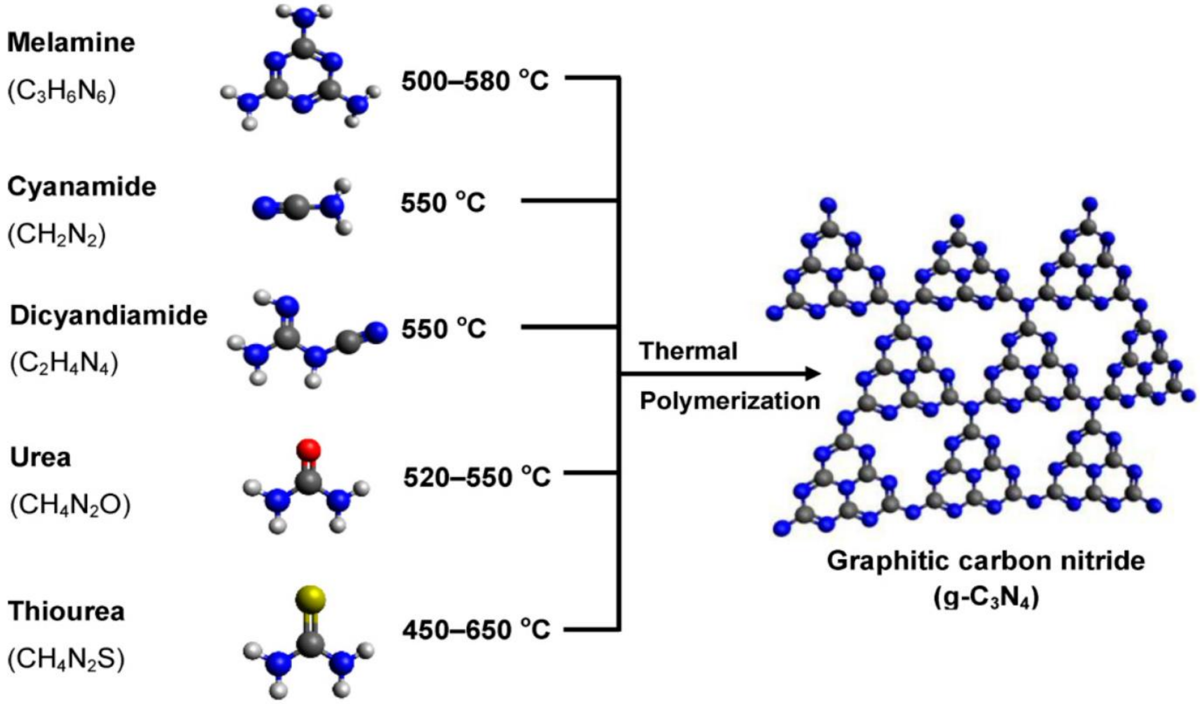

Fig. 2. Bulk g-C_3N_4 synthesis routes from different precursors. Carbon, nitrogen, hydrogen, and oxygen are represented by black, blue, white, red, and yellow spheres. Reproduced with permission from [31].

2.1. Top-Down approaches

The synthesis of g-C_3N_4 QDs through a top-down approach entails generally a multi-step process. This involves the initial preparation of a bulk g-C_3N_4 nanostructure as template, followed by its gradual reduction by means of subsequent cutting to form nanosized g-C_3N_4 QDs. The synthetic pathway frequently necessitates elevated energy consumption due to the fact that the production of bulk g-C_3N_4 template is executed at temperatures exceeding 400 °C. The present section covers the synthesis g-C_3N_4 QDs through top-down routes. Despite the intricate processes, high costs, structural imperfections, and use of strong acids, bases, or oxidizers associated with the top-down approaches to produce g-C_3N_4 QDs, particular benefits remain captivating. These include simple operation, improved uniformity, and the ability to mass produce.

2.1.1. Hydrothermal

The hydrothermal method is a straightforward, environmentally friendly, and cost-effective procedure that has seen widespread use in recent years for the synthesis of a broad variety of nanomaterials, including carbon-based QDs [119–121]. Using hydrothermal solution, it is also possible to progressively exfoliate 3D g-C_3N_4 into 0D QDs. This is accomplished by taking advantage of the thermal shear force that is created under conditions of high temperature and pressure. Similar to other synthesis techniques, the combination of several pretreatments prior to the hydrothermal treatment is widely used to yield g-C_3N_4 QDs. For example, Wang et al. [47] first reported the synthesis of g-C_3N_4 QDs via hydrothermal route in 2014. They used a multi-step procedure, consisting mainly of heat etching by thermal oxidation to exfoliate bulk g-C_3N_4 into g-C_3N_4 nanosheets, followed by acidic cutting to yield g-C_3N_4 nanoribbons, and finally reaching the QDs state by hydrothermal cutting at 200 °C with a pH of 5 (**Fig. 3a**). The produced suspensions were utilized as photocatalyst for H_2 evolution in the presence of a co-catalyst (Pt) and sacrificial agent (triethanolamine). Their findings revealed the formation of H_2 at rates of 48.05 and 109.96 mmol h^{-1} for bulk g-C_3N_4 and g-C_3N_4 QDs–g-C_3N_4 hybrids, respectively.

With the same mindset, Li et al. [76] described the use of a binary process to yield g-C_3N_4 QDs. Their reported approach consists primarily of an oxidation process by ultrasonication using mixed nitric and sulfuric acids, followed by hydrothermal treatment at 80 °C for 4 h. The resulting suspension was dialyzed to yield pure g-C_3N_4 QDs. The reported QD size was about 20 nm, which is significantly larger than those recorded by Wang et al. [47] which was around 10 nm. This comparison suggests that thermal oxidation promotes higher nanosheet etching than the wet oxidation protocol, thus producing smaller QDs.

One step hydrothermal treatment was also used for the synthesis of g-C_3N_4 QDs. This was suggested by Zhan et al. [75] who suspended bulk g-C_3N_4 in a combination of concentrated KOH and ethanol solution, followed by hydrothermal treatment in autoclave at 180 °C for 16 h (**Fig. 3b**). It is worth mentioning that KOH presence enables the facile exfoliation of bulk g-C_3N_4 via K^+ and OH^- intercalation in the interlayer interface. The authors reported an average QD diameter of 3.3 nm. Scholars have used hydrothermal thermal route to combine different nanomaterials and g-C_3N_4 QDs. For example, Zhang et al. [81] reported the use of the same protocol described by Wang et al. [47] to yield g-C_3N_4 QDs. This latter was electrodeposited on 3D TiO_2 nanotube arrays (TNA) to yield 3D g-C_3N_4/TNA hybrid system that was applied in visible light-driven photocatalytic hydrogen production (**Fig. 3c**).

2.1.2. Ultrasonication

Ultrasonic waves have the ability to produce low- and high-pressure waves within a liquid medium, resulting in the creation and subsequent implosion of diminutive vacuum bubbles. Cavitation results in the generation of a high-velocity impact jet, which induces a robust hydrodynamic shear force. Hence, the energy inherent in ultrasound waves can be harnessed to facilitate the exfoliation of voluminous three-dimensional g-C_3N_4 into two-dimensional nanosheets, one-dimensional nanowires or nanoribbons, and ultimately into zero-dimensional quantum dots. Indistinguishable from the hydrothermal pathway, ultrasonication technique is often coupled with other pretreatments for the purpose of bulk g-C_3N_4 exfoliation and cutting to QDs. Overall, the process of converting bulk g-C_3N_4 into porous g-C_3N_4 involves initial oxidation using strongly oxidizing acids, followed by exfoliation into porous nanosheets under conditions of high temperature and pressure. Subsequently, a procedure involving ultrasound bath treatment is executed to disintegrate the nanosheets into QDs, which is succeeded by a conclusive purification process by centrifugation and dialysis. From this angle, Zhang et al. [53] employed a mixed solution of sulfuric and nitric acids to break down bulk g-C_3N_4, followed by a hydrothermal treatment of the oxidized products suspended in ammonia solution, resulting in the production of porous g-C_3N_4 nanosheets. Subsequently, the nanosheets underwent sonication in water, ultimately resulting in the formation of QDs (**Fig. 3d**). In their initial state, the produced g-C_3N_4 QDs exhibit a distribution of diameters that vary between 2 and 6 nm, and a median thickness of approximately 0.35 nm, which is similar to the thickness of a C-N monolayer, as depicted in **Fig. 3d**. Furthermore, it is noteworthy that the surface of single-layer QDs exhibits a negative charge, thereby conferring exceptional stability to the suspension of g-C_3N_4 QD over a period of several weeks.

With the same mindset, Wang and coworkers [93] conducted a study wherein they utilized a modified Hummers' method to prepare single-layer g-C_3N_4 QDs (**Fig. 3e**). In brief, H_2SO_4 and $NaNO_3$ were used for an initial oxidation of bulk g-C_3N_4, resulting in the formation of an intermediate possessing a chain-like structure. This latter underwent further oxidation with $KMnO_4$

to yield reduced-size flakes of g-C_3N_4, followed by the addition of H_2O_2 and ice water to stop the reaction. Subsequently, the g-C_3N_4 QDs were acquired through ultrasonication. The reported QDs were relatively larger than previous studies, which were up to 31 nm. Finally, the produced g-C_3N_4 QDs were mixed with graphene oxide (GO) and subjected to hydrothermal treatment to yield a hybrid hydrogel-based catalyst for oxygen reduction reaction.

Alternatively, many studies in the state of the art used one-step ultrasonication treatment to break down g-C_3N_4 form the bulk form to the QD state. In this regard, Wang et al. [122] utilized sonication to produce g-C_3N_4 QDs from a water suspension of bulk g-C_3N_4, which was synthesized by calcining dicyandiamide for 10 h. The product obtained through sonication was observed to be a heterojunction comprising of g-C_3N_4 QDs and g-C_3N_4 nanosheets. The QDs, having diameters less than 10 nm, were found to be embedded within the nanosheets. In another study, Cui and colleagues [94] described the production of phenyl-modified g-C_3N_4 QDs through the ultrasonication of an aqueous suspension of bulk g-C_3N_4 containing phenyl groups, followed by a centrifugation process to eliminate the unexfoliated bulk g-C_3N_4. The prepared products were referred to as g-C_3N_4 nanosheets, as supported by the observations made through atomic force microscopy (AFM) and transmission electron microscopy (TEM), which revealed that the nanosheets possess diameters of several tens of nanometers and thicknesses of 5-6 nm. The introduction of phenyl groups onto g-C_3N_4 QDs has been observed to have an impact on the π-electron delocalization within the conjugated carbon nitride network. This effect has been found to result in a notable increase in the quantum yield, with values reaching up to 48% in aqueous media.

Wang's research group [86], reported another example of synthesizing g-C_3N_4 QDs through the process of sonication. In order to enhance the efficacy of QDs, the researchers produced fluorine-doped g-C_3N_4 QDs utilizing bulk fluorine-doped g-C_3N_4, synthesized using melamine and ammonia fluoride precursors. It is noteworthy that the exfoliation of fluorine-doped g-C_3N_4 was carried out in ethylene glycol rather than water. The utilization of ethylene glycol as a solvent in the fabrication process served a dual purpose. Firstly, it functioned as a scavenger for the active C and N radicals present in the doped nanosheets, thereby preventing their restacking. Secondly, the viscous nature of the ethylene glycol served to restrict the aggregation of QDs. The doped QDs exhibited a size distribution ranging from 1.5 to 2.0 nm when suspended in ethylene glycol.

Additionally, these QDs demonstrated a greater fluorescence intensity when compared to undoped g-C_3N_4 QDs.

2.1.3. Evaporation-condensation/hydrolysis

In addition to the methods previously mentioned, there have been reports of utilizing one-pot evaporation-condensation and hydrolysis techniques [48,85] to produce g-C_3N_4 QDs. In their study, Yin et al. [85] employed a household microwave oven to apply heat to a crucible containing a combination of bulk g-C_3N_4 powder and SiC_2 particles for 5 min (**Fig. 3f**). Subsequently, centrifugation was performed to eliminate the larger particles from g-C_3N_4 QDs. In the course of the evaporation-condensation process, the presence of SiC_2 particles can furnish ample vibrational kinetic energy to facilitate the cleavage of the g-C_3N_4 layers, thereby engendering diminutive g-C_3N_4 fragments that can be utilized for the subsequent production of QDs. In contrast to traditional techniques, the employment of the proposed microwave-assisted methodology presents a more convenient and efficient alternative, resulting in a potential yield of g-C_3N_4 QDs of up to 40%. Additionally, the synthesized g-C_3N_4 QDs demonstrated notable levels of crystallinity, exceptional fluorescence, and a relatively dense size distribution. The aforementioned benefits render the evaporation-condensation technique a viable option for the production of g-C_3N_4 QDs on a mass scale.

In another study, Zhang et al. [48] employed a protic solvent to trigger the hydrolysis of bulk g-C_3N_4 in an H_2SO_4 solution, resulting in a combination of g-C_3N_4 QDs and nanoleaves. The obtained QDs exhibited limited sizes, ranging from 2 to 4 nm, while the resulting nanoleaves displayed lengths that varied between 200 to 500 nm. The findings of the authors indicate that g-C_3N_4 nanorods can be synthesized utilizing CH_3OH as an alternative protic solvent. The g-C_3N_4 QDs prepared in this study demonstrated a notably high quantum yield of 46%, which surpasses the quantum yield of a majority of g-C_3N_4 QDs synthesized through alternative techniques.

2.2. Bottom-Up approaches

The process of synthesizing carbon-based QDs utilizing organic molecules as a precursor through a singular step is referred to as bottom-up synthesis. Generally speaking, the breakdown of organic molecules comprises three distinct stages. One notable observation is that organic molecules have a propensity to generate macromolecular intermediates via condensation reactions, including but not limited to amidation, aldol condensation, Schiff base condensation, and radical reaction. The second point to consider is that external pressure, temperature, or microwave exposure can result in the degradation of chemical bonds within macromolecules present in the reaction system. This degradation can lead to the formation of carbon-based fragments and free radicals. The third observation is that the carbon-based fragments further undergo carbonization, resulting in the formation of nanoscale carbon-based QDs. The interactions between free radicals and carbon-based QDs can lead to the formation of functional groups within the layered carbon-based QDs, resulting in a reduction of defects. g-C_3N_4 QDs, being a variant of carbon-based QDs, are expected to undergo a comparable formation process through pyrolysis or carbonization of specific molecular precursors. To date, a variety of organic molecules rich in nitrogen have been utilized as precursors, such as formamide, N,N-dimethyl formamide (DMF), melamine, guanidine hydrochloride, urea, dicyandiamide, and organic amines. The bottom-up approach involves utilizing the target atoms as fundamental units for the facile fabrication of heterogeneous doping. This approach enables precise control over the nanostructure of g-C_3N_4 QDs, which is contingent upon the specific properties that are being engineered.

2.2.1. Solid-phase approaches

Solid-phase synthesis denotes the occurrence of a chemical reaction between solid reactants, in which the original chemical bonds are broken and new chemical bonds are formed. In contrast to the high-temperature synthesis of bulk g-C_3N_4 (> 450 °C), the solid-phase method can be employed to prepare g-C_3N_4 QDs at comparatively lower temperatures. Zhou and colleagues [58] have documented the synthesis of a specific variant of g-C_3N_4 QDs that exhibit high fluorescence. Their synthesis involved utilizing urea and sodium citrate as precursors at 180 °C for a duration of 1 h (**Fig 3g**). The synthesized g-C_3N_4 QDs exhibited a limited range of sizes, measuring between 2.6-5.5 nm, and possessed a standard topographic height of 1.5-2.5 nm. Additionally, these g-C_3N_4 QDs demonstrated a substantial quantum yield of 42%. The present study highlights that the emission of the synthesized g-C_3N_4 QDs can be modulated by varying the molar ratio of the two reactants.

Following this, the solid phase method has been utilized to prepare g-C_3N_4 QDs with varying characteristics using alternative precursors such as urea and citric acid, thiourea and sodium citrate, melamine and EDTA, and cyanuric chloride, 4-diamino-6-phenyl-1,3,5-triazine (DPT), and 2,4,6-trihydrazino-1,3,5-triazine (THDT) [112,113,123,124]. For example, He et al. synthesized sulfur-doped

$g\text{-}C_3N_4$ QDs using thiourea and sodium citrate. The doped QDs exhibited reduced average diameters and a slightly enhanced light absorption edge in comparison to the undoped QDs. In another work, Fan et al. [112] presented a straightforward and efficient method for synthesizing $g\text{-}C_3N_4$ QDs with strong fluorescence. This was achieved through a solid-phase pyrolysis process of melamine and EDTA at a temperature of 350 ℃ for a duration of 1 h. The as-prepared $g\text{-}C_3N_4$ QDs exhibited a high degree of dispersion with minimal aggregation. The particles were found to be predominantly distributed within the size range of 3-8 nm, with an average diameter of 5 nm. Furthermore, the $g\text{-}C_3N_4$ QDs had the capability to generate potent chemiluminescence (CL) when $K_3[Fe(CN)_6]$ was present. Using the same approach, Patir and Gogoi [125] produced a variant of $g\text{-}C_3N_4$ QDs that were doped with sulfur and oxygen. Their synthesis involved utilizing thiourea and ethylenediaminetetraacetic acid disodium salt with a molar ratio of 1:2 as precursors in a solid-phase method. The reaction was carried out at a temperature of 200 ℃ for a duration of 2 h. The synthesized $g\text{-}C_3N_4$ QDs exhibited a broad range of sizes, spanning from 3-13 nm, with a quantum yield of 13.4%.

In another work, Through the copolymerization of melamine with carefully chosen monomers, including cyanuric chloride, 4-diamino-6-phenyl-1,3,5-triazine (DPT), and 2,4,6-trihydrazino-1,3,5-triazine (THDT), Wu et al. [123] designed $g\text{-}C_3N_4$ QDs (CN, CN-DPT, and CN-THDT QDs) (average size ≈ 200 nm) with distinct two-photon catalytic capacities to generate reactive oxygen species (ROS). These $g\text{-}C_3N_4$ QDs were shown to have excellent biocompatibilities, allowing them to be administered to tumor cells for imaging and treatment based on their *in vitro* cytotoxicity assessment (**Fig. 3i**).

2.2.2. Microwave-assisted approaches

The first documented production of $g\text{-}C_3N_4$ QDs was achieved through employment of the microwave-assisted solvothermal technique [99]. Microwave irradiation can induce the breakdown of chemical bonds in carbon-containing and nitrogen-containing precursors, leading to the rapid formation of $g\text{-}C_3N_4$ QDs through polymerization or carbonization processes. The heat released during this process is responsible for the observed effect. Microwave irradiation can provide uniform thermal energy, thereby ensuring an even size distribution of the produced QDs. The utilization of microwave-assisted solvothermal technique to produce $g\text{-}C_3N_4$ QDs has gained significant popularity thanks to its cost-effectiveness and superior efficacy. Liu et al. [99] conducted microwave heating of a mixture comprising CCl_4 and 1,2-ethylenediamine (EDA) to obtain photoluminescent g-C_3N_4 QDs with diameters ranging from 2-4 nm (**Fig. 3h**). This work can be considered pioneering since the production of g-C_3N_4 QDs can also be achieved through reflux heating or solvothermal heating of CCl_4 and EDA. Subsequently, the production of fluorescent g-C_3N_4 QDs was conducted through the application of microwave irradiation to an N,N-dimethylformamide solution or organic amines such as dimethylamine, ethylamine, or tripropylamine in the presence of acids such as chlorosulfonic acid, H_2SO_4, HCl, or HNO_3 [126]. Literature has also documented the microwave-assisted solvothermal production of g-C_3N_4 QDs with a limited size distribution, utilizing either one or two organic precursors such as formamide, chitosan, guanidine hydrochloride and EDTA, folic acid, citrate, and urea or thiourea [99,100,107–109]. The synthesis of amino-functionalized or sulfur and oxygen co-doped g-C_3N_4 QDs is particularly achieved through the utilization of an amine-terminated precursor (chitosan) or sulfur-containing precursor (thiourea).

The growth of g-C_3N_4 QDs through hydrothermal or solvothermal methods is typically prolonged. Consequently, a rapid and efficient technique has been devised by integrating the hydrothermal or solvothermal approach with the microwave methodology. One example is the growth of graphene quantum dots (GQDs), which can be expedited to a matter of minutes or seconds through the utilization of microwave-assisted techniques. Furthermore, the g-C_3N_4 QDs synthesized through the above-mentioned integrated approach frequently exhibit comparatively elevated production and quantum yields. A study conducted by Achadu and Revaprasadu [127] involved the synthesis of thymine-modified g-C_3N_4 QDs through the utilization of diaminomaleonitrile and thymine-1-acetic acid as precursors, with distilled water serving as the solvent. The synthesis was carried out using a microwave-assisted hydrothermal method at a temperature of 180 °C for a duration of 5 min. The produced thymine-modified g-C_3N_4 QDs exhibited a size range of 3 to 8 nm and demonstrated favorable water solubility and exceptional optical characteristics, including a fluorescence quantum yield of up to 46%.

In another work, Pandey and colleagues [128] achieved the controllable synthesis of nitrogen-doped GQDs and g-C_3N_4 QDs by regulating the ratio of precursors, including citric acid and urea, using solid-phase microwave-assisted heat (SMPA) technology at a temperature of 250 °C for a duration of 5 min. The atomic ratio, surface functionalization, and atomic structure of the as-prepared quantum dots were significantly influenced by the citric acid to urea ratio, as illustrated in **Fig. 3j**. The g-CNQDs synthesized under a citric acid to urea ratio of 1:3 exhibited a size distribution of 3.5 nm and a quantum yield of 26.3%.

2.2.3. CVD approach

The quasi-chemical vapor deposition technique involves situating a substrate mounted on a crucible, while introducing a precursor containing carbon and nitrogen at the crucible's base. Upon subjecting the crucible to thermal heating within a furnace, the precursor undergoes sublimation and subsequently decomposes into QDs on the substrate. Thus, the synthesis of composites consisting of substrate and g-C_3N_4 QDs is achieved through a direct process. Typically, in order to obtain uncontaminated g-C_3N_4 QDs, the substrate that has been coated with QDs is submerged in an appropriate solvent and subsequently subjected to sonication to facilitate the detachment of the QDs from the substrate. To date, there have been reports on the synthesis of g-C_3N_4 QDs in conjunction with a TiO_2 nanotube array (TiO_2-NTA) substrate through a quasi-chemical vapor deposition process [60,65]. Li et al. [65] and An et al. [60] synthesized TiO_2-NTAs/g-C_3N_4 QDs composites through the thermal treatment of melamine or dicyandiamide at 550 °C for a duration of several hours (**Fig. 3k**). The formation of g-C_3N_4 can be achieved through the thermal decomposition of melamine or dicyandiamide, as it is a widely recognized synthesis protocol. Remarkably, in the quasi-chemical vapor deposition procedure, the minuscule molecules that arise from the disintegration of the precursor undergo polymerization into QDs. Moreover, the TiO_2-NTA substrate exhibits the capability to impede the subsequent polymerization of QDs to macroscopic particles or nanosheets. It is noteworthy that Li et al. [65] observed g-C_3N_4 QDs confined within the interior of TiO_2-NTAs, whereas An et al. [60] demonstrated g-C_3N_4 QDs decorated on the surface of TiO_2-NTAs. The observed inconsistency may have arisen due to the distinct compositions of the two TiO_2-NTA specimens that were synthesized using disparate techniques. The average diameter of g-C_3N_4 QDs enclosed within the TiO_2-NTAs was approximately 2.4 nm, comparatively smaller than the diameter of QDs coated on the surface of TiO_2-NTAs, which measured at approximately 5.2 nm. This observation suggests that the degree of confinement within the interior of TiO_2-NTAs is more pronounced.

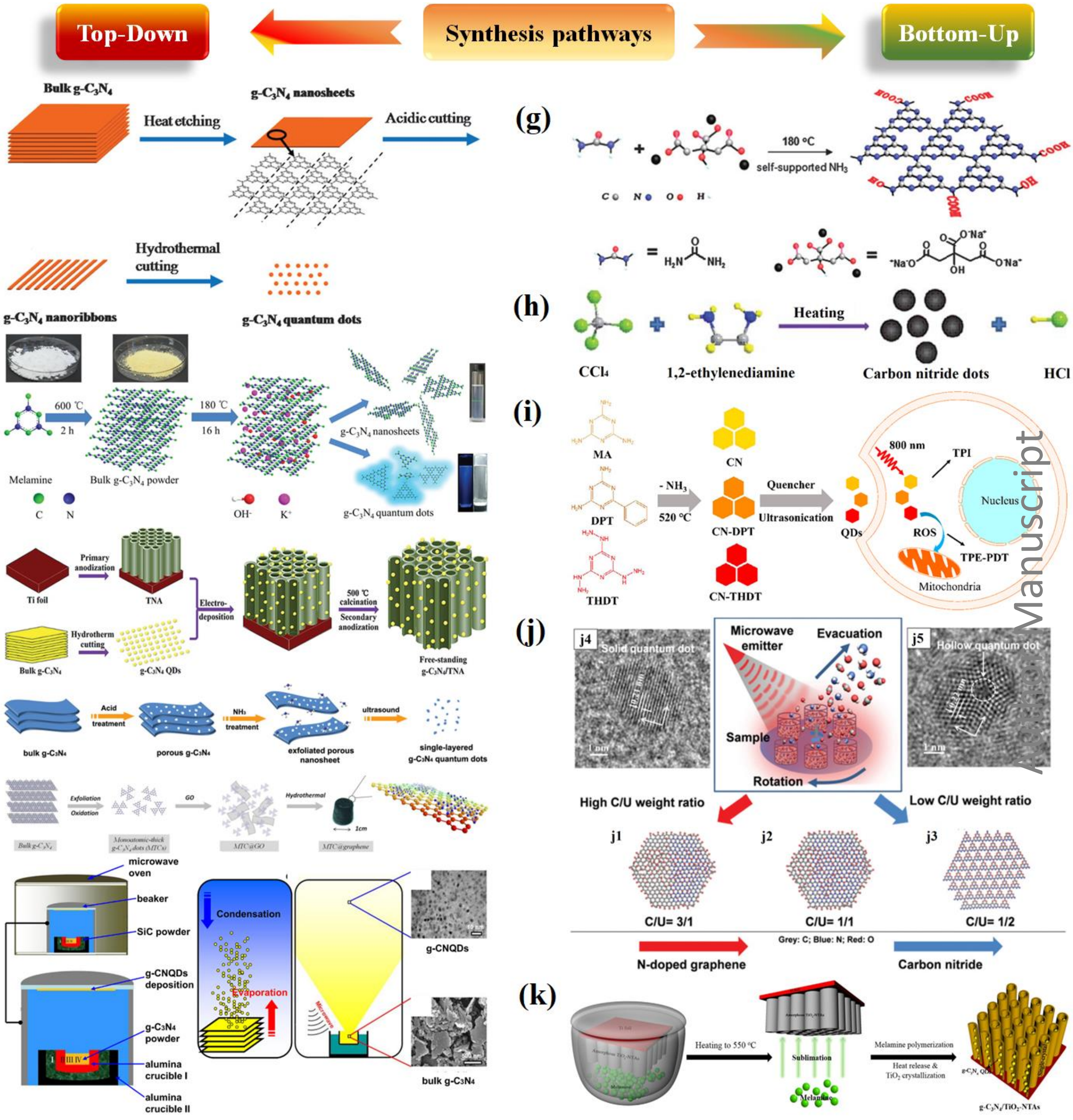

Fig. 3. Top-down and bottom-up synthesis pathways of g-C_3N_4 QDs. (a) Hydrothermal synthesis of g-C_3N_4 QDs with heat etching and acid cutting pre-treatments. Reproduced with permission from [47]. (b) Illustrative representation of size-controlled g-C_3N_4 nanosheets and QDs synthesis via ethanol-thermal treatment in the presence of KOH. Reproduced with permission from [75]. (c) Illustrative representation of the production procedure of 3D g-C_3N_4/TNA. Reproduced with permission from [81]. (d) Schematic illustration of the ultrasonication route to produce single-layered

$g\text{-}C_3N_4$ QDs. Reproduced with permission from [53]. (e) Synthetic protocol for the $g\text{-}C_3N_4$ QDs preparation via ultrasonication route. Reproduced with permission from [93]. (f) illustration of the fabrication device, the evaporation–condensation process, and distribution of $g\text{-}C_3N_4$ during the transport process. Reproduced with permission from [85]. (g) Formation mechanism by bottom-up route of highly fluorescent $g\text{-}C_3N_4$ QDs using a solid-state reaction. Reproduced with permission from [58]. (h) Illustration of the formation process of $g\text{-}C_3N_4$ QDs by microwave assisted route from CCl_4 and 1,2-ethylenediamine (EDA) to obtain photoluminescence $g\text{-}C_3N_4$ QDs. Reproduced with permission from [99]. (i) Illustration of the Preparation via solid-state reaction of Three $g\text{-}C_3N_4$ QDs as Dual-Functional Nanoplatforms for two-photon imaging (TPI) and two-photon excited photodynamic therapy (TPE-PDT) in breast cancer. Reproduced with permission from [123]. (j) illustrative representation of two-dimensional atomic structures produced during SPMA process with different citric acid/urea weight ratios simulated by molecular dynamics software. Reproduced with permission from [128]. (k) Illustrative representation of $g\text{-}C_3N_4$ QDs/TiO_2-NTAs operatory procedure via CVD technique. Reproduced with permission from [65].

3. Characterization and physicochemical properties of $g\text{-}C_3N_4$ QDs

The optical, electrical, and catalytic properties of $g\text{-}C_3N_4$ QDs are determined by factors such as size, functional groups, and dopants due to their spatial electronic structure and quantum size effect. It is essential to fine-tune these characteristics to produce $g\text{-}C_3N_4$ QDs with clearly defined features, which will, in turn, promise that their use will be more efficient in many applications, such as photocatalysis, sensing, optoelectronics, and biomedical. In the past few years, the identification of $g\text{-}C_3N_4$ QDs nanostructures utilizing various techniques, including X-ray photoelectrons spectroscopy (XPS), has received considerable interest. For example, the deconvoluted XPS spectra of C1s, N1s, and O1s were employed to study the composition and chemical bonding between C, N, and O atoms of $g\text{-}C_3N_4$ QDs (**Fig. 4.**) [129]. The C1s spectra of bulk $g\text{-}C_3N_4$ exhibited two peaks at 284.6 and 288.2 eV attributed to the C─N─C/C─C (sp^2), and $C─(N)_3$ sp^3-tertiary nitrogen bond, respectively. Additionally, its N1s spectra confirm the typical peaks of $g\text{-}C_3N_4$ at 398.9, 400.2, and 401.2 eV, which are ascribed to C─N─C (sp^2-hybridized nitrogen), $N─(C)_3$ (bridging nitrogen), and N─H (the free amino groups), respectively [130]. For the case of $g\text{-}C_3N_4$ QDs, the high-resolution C1s spectra display a doublet peak, deconvoluted into three separate peaks at 284.6, 285.7, and 288.2 eV. These peaks correspond, in order, to the C─N─C/C─C/C─H, C─O, and $C─(N)_3$ bonds, respectively. The fact that the intensity of the peak at 284.6 eV compared to that at 288.2 eV is substantially higher than that for bulk $g\text{-}C_3N_4$ is noteworthy, and the appearance of the C=O bond suggests the participation of carboxylate groups in the formation of $g\text{-}C_3N_4$ QDs via acidification reaction. This deduction is further confirmed by the high-resolution O1s spectrum analysis, which shows that carboxylate groups are present in the substance. Furthermore, the deconvoluted N1s spectra of $g\text{-}C_3N_4$ QDs exhibit three peaks at 398.5, 399.6, and 400.8 eV, corresponding to the sp^2 N atoms involved in the tris-s-triazine rings

$(C-N=C)$, $N-(C)_3$ or $H-N-(C)_2$, and $C-N-H$ bonds, respectively. This indicates that the triazine units of bulk g-C_3N_4 are preserved within g-C_3N_4 QDs [131]. For example, Juan et al. [58] measured a large oxygen content in the g-C_3N_4 QDs synthesized by low-temperature treatment using urea as a precursor. The authors observed that the $C-O$ and $O-C=O$ bonds were responsible for the peaks in binding energy found at 286.07 and 289.02 eV, respectively. These peaks point to the presence of oxygen-rich groups. These findings, in conjunction with the existence of $N-C=N$ bonds, point to the heptazine heterocyclic ring unit as being the fundamental component of the g-C_3N_4 QDs substructure. According to the XPS results, the oxygen content of g-C_3N_4 QDs increases, while the nitrogen content decreases, suggesting that oxygen-containing groups are introduced and nitrogenous groups are degraded during the reaction process. Similar results were found when comparing the g-C_3N_4 nanosheets to those described above. Notably, g-C_3N_4 QDs were observed to have small redshifts in their N1s and O1s spectra. These findings show that oxygen-rich groups may be successfully introduced to g-C_3N_4 QDs, which dramatically improves their suitability for use in solution-based applications without significantly altering their optical properties [75]. This example demonstrates very clearly why such an analysis is necessary to define and confirm the structure of surface-modified g-C_3N_4 QDs.

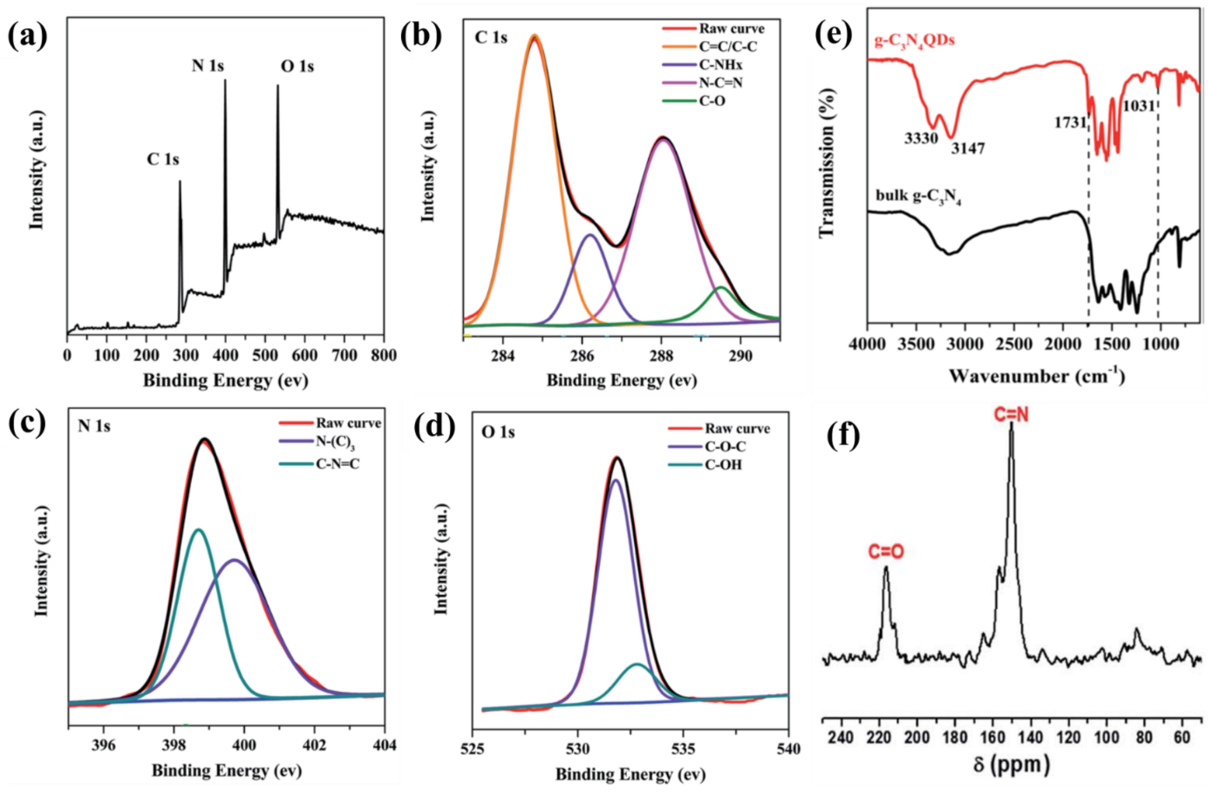

Fig. 4. XPS survey spectra (a) and high-resolution C1s (b), N1s (c) and O1s (d) XPS spectra of g-C_3N_4 QDs. FTIR spectra of bulk g-C_3N_4 and g-C_3N_4 QDs (e). Reproduced with permission from [132]. (f) The solid state ^{13}C NMR spectrum of the g-C_3N_4 QDs. Reproduced with permission from [129].

In addition to XPS, the chemical composition and structural information on g-C_3N_4 QDs can be obtained using Fourier-transform infrared (FTIR) spectroscopy. As seen in **Fig. 4e**, the spectrum of g-C_3N_4 QDs is very similar to that of bulk g-C_3N_4, with similar absorption bands at approximately 1409 cm^{-1} (C─N) [133] and 1580 cm^{-1} (C═N) [48,133]. Moreover, the g-C_3N_4 QDs display additional strong bands at 1032 and 1731 cm^{-1}, which can be assigned to the stretching modes of C─O and C═O [132], respectively. The bands at 1213 and 1317 cm^{-1} are attributed to the secondary and tertiary amines C_2─N and C_3─N[104], respectively. The broad band at approximately 3400 cm^{-1} corresponds to the stretching mode of O─H/N─H, which is consistent with the results of the XPS analysis and suggests that hydrolysis may be taking place. Despite this, there is a disappearance of some stretching vibrations between 800 and 1800 cm^{-1} in the spectra of the g-C_3N_4 QDs. This can be attributed to a partial break in the triazine rings, which is caused by the small sizes of the QDs. Zheng et al. [134] have confirmed the carbon nitride (CN) backbone structure in g-C_3N_4 QDs, obtained by light-triggered self-assembly mechanism, by the bands observed at 724, 840, and 1572 cm^{-1}, which are ascribed to the bending vibration of C─NH─C, the characteristic triazine ring breathing mode [135], and the C═N stretching mode in heterocyclic CN, respectively [136]. A band at 625 cm^{-1}, corresponding to the wagging mode of NH or NH_2, is presumably developed from the edge NH_2 groups or connecting NH species. A peak at 906 cm^{-1} due to the out-of-plane bending vibration of the aromatic C-H is observed, likely indicating the presence of pyrimidine groups in g-C_3N_4-QDs [135]. The band at 1300 cm^{-1} corresponds to the C─O vibrations in the C─OH group [137], whereas the bands at 1391 cm^{-1} and 1668 cm^{-1} correspond to the OH bending mode and C═O stretching mode in the -COOH groups [125,138], respectively. Thus, the as-prepared g-C_3N_4-QDs have an overall triazine-based structure with carboxyl (-COOH), hydroxyl (-OH), and amine (-NH_2) functional groups, rendering them excellent dispersion in aqueous media.

One of the most powerful techniques for analyzing the carbon environment of semicrystalline or amorphous materials is solid-state nuclear magnetic resonance spectroscopy (ssNMR). Teter and Hemley [19] predicted theoretically that, for an ideal hexagonal graphitic material, the characteristic peak in ^{13}C magic angle spinning (MAS) NMR should be at 150 ppm. The carbonyl groups from the precursor were successfully formed at the rim of the g-C_3N_4 QDs networks synthesized by the bottom-up approach, as confirmed by the solid-state ^{13}C-NMR spectra of the g-C_3N_4 QDs [129]. When compared to the negligible resonance signals in the range of 160–220 ppm previously reported for g-C_3N_4, the clearly detectable peak at 210 ppm is an indication of the C═O bond (**Fig. 4f**), and the peak that is originated at 150–160 ppm could be attributed to the C─N═C bonds, although there were no signals found coming from saturated sp^3 carbon atoms in g-C_3N_4 QDs [139,140]. Sudip and Mriganka [104] recorded ^{13}C NMR of g-C_3N_4 QDs in DMSO-d_6. The CN_3 group of the hexagonal graphitic C_3N_4 moiety is responsible for the distinctive peak of g-C_3N_4 QDs at 151 ppm in its spectral profile. The peak at 161.2 ppm can be attributed to the sp^2-hybridized carbon of s-triazine rings. Zhen et al. [134] observed only a single resonance at 164.3 ppm using ^{13}C liquid-state NMR spectrum of g-C_3N_4 QDs. This resonance is assigned to the C(e) atoms (N_2─CN or terminal $CN_2(NH_x)$) in triazine units. There is an absence of the typical signals corresponding to the C(i) atoms (CN_3) in heptazine units at around 156 ppm. Hence, a triazine-based crystal structure has been confirmed by NMR.

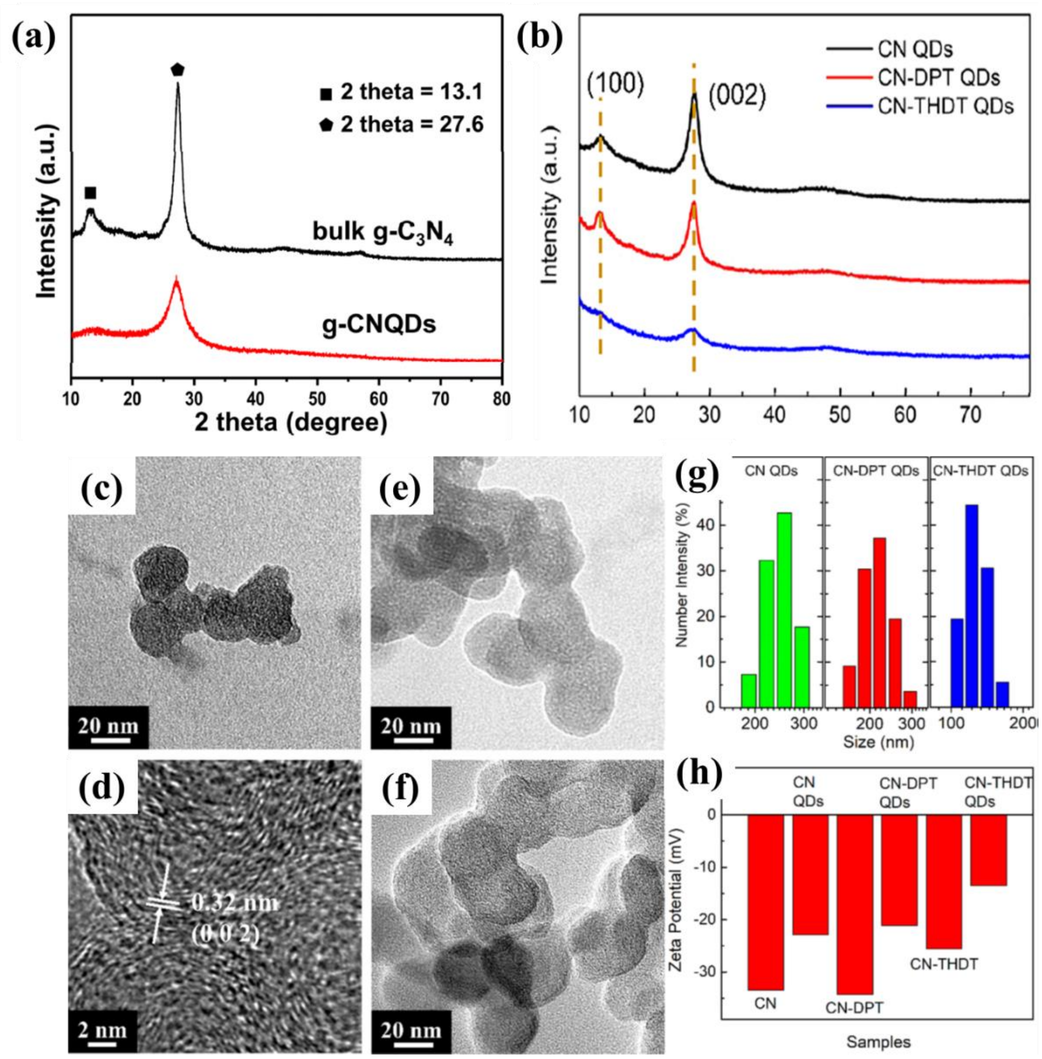

Fig. 5. XRD pattern of bulk g-C_3N_4 and g-C_3N_4 QDs (a, b) Reproduced with the permission from [85], TEM image and the high resolution-TEM image of CN-QDs (c, d) TEM images of CN-DPT and CN-THDT QDs (e, f). Zeta potential of carbon nitride quantum dots in pure water (g, h) Reproduced with permission from [123].

The degree of carbonization and the defect concentration changes of g-C_3N_4 QDs have been studied and validated by X-ray diffraction (XRD). Overall, determination of the graphitic structure and measurement of the lattice constant have both benefited from XRD studies. For example, Xiaoxia et al. [123] confirmed that calcination creates the ordered lattice structure of g-C_3N_4 QDs synthesized by bottom-up approach, which is shown by the dominant peaks at 27.4° and 13.0° (**Figs. 5a** and **5b**). When compared to g-C_3N_4 QDs, the diffraction peaks of CN-DPT-QDs and CN-THDT QDs are slightly shifted to a low angle. This may be due to the fact that functional monomers were added to the CN-QDs, which caused the layer structure to become disordered [141]. According to the XRD spectra, the interplanar distance at 27.6° is 0.32 nm, which is the same as the HRTEM result for the three g-C_3N_4 QDs [47]. The CN-QDs have a clear diffraction ring, and the XRD results show that the interplanar distance is 0.312 nm, matching the lattice plane (002). Similar to CN-QDs, the interplanar distances of CN-DPT and CNTHDT-QDs are 0.330 and 0.329 nm, respectively, and match the lattice plane of (002) from the XRD results. The fact that the diffraction peaks of g-C_3N_4 QDs and those of bulk g-C_3N_4 are quite similar and agree with one another strongly suggests that the two substances have the same fundamental crystal structure. Both the strong peak at 27.5°, which corresponds to the (002) plane, and the relatively weak peak at 13.1°, which is attributed to the (100) plane, can be seen in the diffraction pattern [132]. Both distinctive diffraction peaks reflect, respectively, the inter-planar stacking of the aromatic ring structure and the in-planar tri-s-triazine unit packing motif [83]. Furthermore, when compared with bulk g-C_3N_4, the relative intensity of the (100) peak for g-C_3N_4 QDs is much lower, which indicates that the in-plane repeated unit structure may be damaged to some degree after solvothermal treatment [142]. This is shown by the fact that the relative intensity of the peak is much lower.

The interlayer structural packing and geometric nanostructure of g-C_3N_4 QDs (002) can be better understood using TEM investigations. On average, the size of the structural packing of the (002) interlayers was observed to be 0.33 nm. Indeed, the synthesis method, temperature, and chemical precursors all play a role in determining this number. By calculating the lattice plane separation of the indexed (002) crystallographic plane of g-C_3N_4 and g-C_3N_4 QDs, TEM images allow us to see minor structural changes in the g-C_3N_4 QDs layers, validating the XRD results. The g-C_3N_4 QDs synthesized by hydrothermal cutting of g-C_3N_4 nanoribbons are shown to be in the range of 5–9 nm in typical TEM images (**Figs. 6a-d**), with an average diameter of 6.7 nm. The g-C_3N_4 QDs have a lattice spacing of 0.336 nm, which corresponds to the (002) plane of hexagonal g-C_3N_4 (JCPDS 87-1526) [47]. For example, Ying et al. [85] obtained highly crystalline g-C_3N_4 QDs with a mean diameter of 3.5±0.5 nm by the microwave-assisted evaporation-condensation approach. In addition, the representative high-resolution TEM (HRTEM) image of an individual dot with a regular circular form, placed on an amorphous carbon-coated copper grid, is shown **in Figs. 6b** and **7a**. The as-obtained g-C_3N_4 QDs had good crystalline quality, which is indicated by the presence of a distinct lattice image in **Fig. 7b**. Consistent with the reference value of the hexagonal g-C_3N_4 phase (The International Centre for Diffraction Data, ICDD-PDF, Card no. 78-1747, space group R3m), the lattice-resolved images have constant spacings of 0.31 and 0.24 nm, which can be assigned to the (100) and (110) planes, respectively, demonstrating the successful formation of high-quality g-C_3N_4 QDs. Consider that the exceptional crystalline quality of as-prepared g-C_3N_4 QDs will allow for an investigation of their inherent features and its clinical uses, such as *in vivo* imaging of tumor vasculature. A statistical analysis of over a hundred g-C_3N_4 QDs reveals that their diameters are within the limited range of 2.2-5.5 nm, with an average size of 3.5±0.5 nm, pointing to the great homogeneity of the g-C_3N_4 QDs formed by the evaporation-condensation technique (**Fig. 7c**). In a study by Xiaoxia et al. [143], g-C_3N_4 QDs synthesized by copolymerizing melamine with other monomers were about 30 nm in size with slightly agglomerated structures, as observed in their TEM images (**Figs. 5c**, **5e**, and **5f**). The clear lattice stripes have interplanar distances of 0.32, 0.34, and 0.33 nm for CN, CN-DPT, and CN-THDT QDs, respectively, which are graphene-like (**Fig. 5d**).

AFM is one of the best tools to study the sizes and thicknesses of g-C_3N_4 QDs. AFM images in **Figs. 7d** and **7e** show that the typical topographic height is about 3–4 nm, meaning that the randomly measured g-C_3N_4 QDs are almost the same thickness and are made up of about 8–11 layers of C–N sheets [85]. In a study by Zhiping et al. [144], the thicknesses of water-soluble g-C_3N_4 QDs synthesized by the chemical oxidation of bulk g-C_3N_4 with nitric acid, followed by hydrothermal process, are reported. The thicknesses of as-prepared g-C_3N_4 QDs by light-triggered self-assembly approach are in the range of 0.9-1.2 nm, which correspond to 3-4 layers of the individual C-N planes (**Figs. 7f** and **7g**) [134].

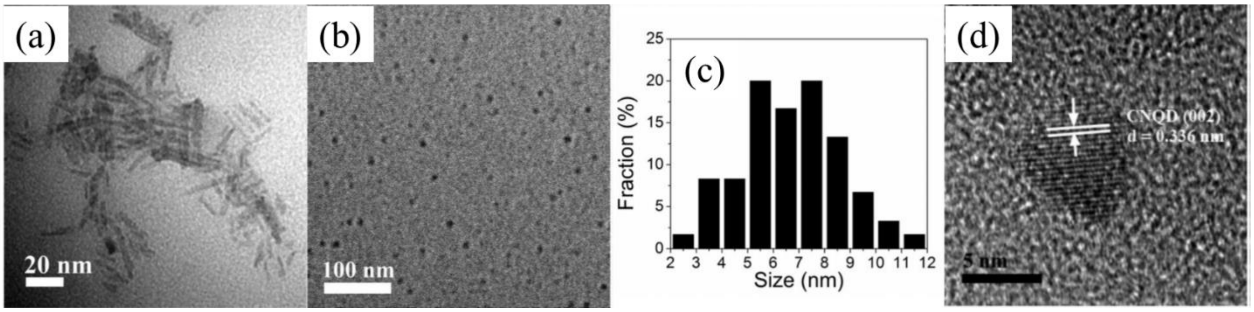

Fig. 6. TEM images of g-C_3N_4 nanoribbons and quantum dots (a, b). Particle size distribution and HRTEM image of g-C_3N_4QD (c, d). Reproduced with permission from [47].

Figs. 5g-5h show the size distribution and zeta potential of g-C_3N_4 QDs dispersed in water. The average sizes of CN, CN-DPT, and CNTHDT-QDs are 246, 213, and 133 nm, which are all larger than the particle sizes measured by TEM. This is due to the fact that g-C_3N_4 QDs in an aqueous medium tend to stick together. Dynamic light scattering (DLS) technique was used to measure storage stability of three different g-C_3N_4 QDs [143]. It can be observed that the sizes of the three different g-C_3N_4 QDs got larger as the amount of storage time increased, which is evidence that agglomeration took place in water. The size distributions of the three g-C_3N_4 QDs are observed to be different (about 200 nm). This could passively target tumor cells because of the increased permeability and retention effect. **Fig. 5h** shows that the zeta potential of three g-C_3N_4 QDs is a little bit lower than that of their corresponding compounds. Since C─N bonds are unstable and easy to break with immediate ultrasonication at a high temperature, a tertiary amine (R_3─N) is converted to a secondary amine (R_2─NH) and a primary amine (R─NH_2) when the three g-C_3N_4 QDs are made. The zeta potential of three g-C_3N_4 QDs goes up when there are more R_2─NH and R─NH_2 groups [123].

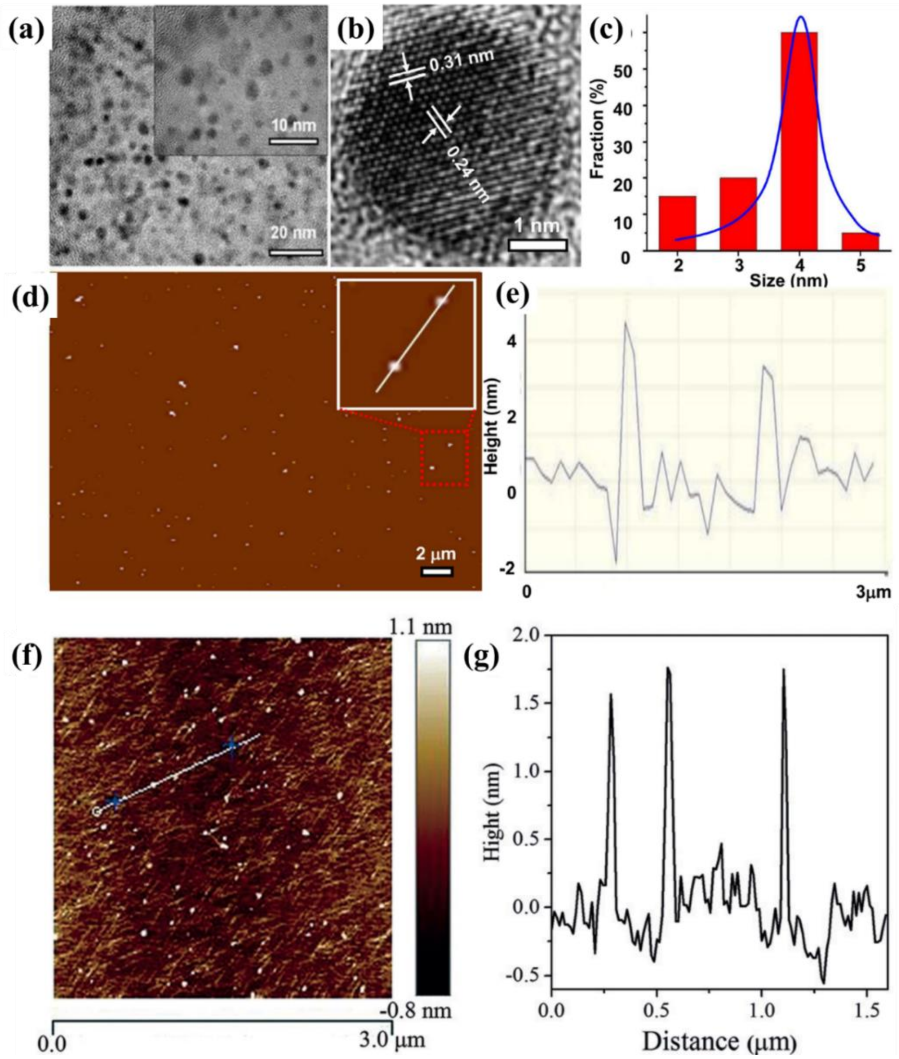

Fig. 7. TEM image (a); high-resolution TEM image (b); size distribution (c) AFM image (d) and height profile (e) of g-C_3N_4 QDs. Reproduced with permission from [85]. AFM image (f) and height profile (g) of g-C_3N_4 QDs. Reproduced with permission from [144].

The g-C_3N_4 QDs have excellent solubility in water and most organic polar solvents such as DMF, DMSO, DMAc, etc., due to the presence of hydrophilic groups. These solutions are stable for several months without any precipitation taking place [15,104,145]. Because of the unique electronic configuration and quantum size effect, g-C_3N_4 QDs exhibit intriguing optical properties [48], including PL, CL, and light absorption that can be adjusted, making them potential candidates for use in many applications such as photocatalysis, light-emitting devices, photodetectors, etc. In general, g-C_3N_4 QDs have a broad optical absorption band that extends from the UV to the visible light region, with the typical absorption peak concentrated in the UV range. Compared to g-C_3N_4 in bulk, the absorption spectra of g-C_3N_4 QDs exhibit significant blue shifts [132,146]. This is probably because the size effect makes the conduction and valence bands move in opposite directions. For example, the prominent peak from 200 to 270 nm with a shoulder centered at 262 nm is caused by the π–π* electronic transition of the tri-s-triazine ring in g-C_3N_4 [144,147]. Thus, UV-Visible spectroscopy confirms the presence of s-triazine rings in g-C_3N_4 QDs. Additionally, the n–π* electronic transition of the C-N bond in the heptazine heterocycle structure causes a second broad peak between 300 and 340 nm [148]. Sometimes, the absorption spectra exhibit new absorption shoulders caused by the passivation of oxygen or heteroatoms on g-C_3N_4 QDs [58,78,149]. Such optical properties have been reported by Yuan et al. [129], where a white-light-emitting g-C_3N_4QD powder shows two major absorption peaks at around 265 and 320 nm. These peaks are ascribed to the π–π* and n–π* transitions of the sp^2 π -conjugation domains and C–O/C═N bonds, respectively [146]. Wu et al. [78] observed two peaks in the absorption spectrum of phosphorus-doped g-C_3N_4 QDs, one at 230 nm due to the π–π* transition and another at 402 nm, which are attributed to the n–π* of p-π orbital between the phosphorus and C–N framework.

The phenomenon of a molecule absorbing the energy of an incident photon is described by PL as the excitation of an electron to a higher energy level, followed by the emission of a photon when the excited electron relaxes. Hence, the bandgap of g-C_3N_4 QDs determines the operative wavelengths that can be a part of the PL spectra of g-C_3N_4 QDs. PL would not be observed in perfect graphene or 0D materials with zero energy bandgap. However, these materials can display PL if certain modifications are made, such as the addition of surface groups, modification of the concentration of dopants, or engineering of the physical dimensions of the material. These factors determine the two primary processes that are used to control PL in g-C_3N_4 QDs as follows: (1) quantum confinement, which is governed by the size of the g-C_3N_4 QDs, and (2) bandgap modification due to the difference in the energy levels of electrons associated with the sp^2 carbons of g-C_3N_4 and electrons associated with the surface groups, dopants, and edge states. Modifying these parameters can achieve the emission range from deep UV to visible blue, green, red, and near infrared (NIR) light. PL is a property used in biological research because some molecules are observed to "glow" when exposed to a certain wavelength of light. This makes it possible to visually isolate an area of interest. Since g-C_3N_4 QDs have many different PL emission windows, they can be used with other molecular dyes whose PL ranges don't overlap [78,123,150,151]. This keeps the cells and tissues being imaged from their intrinsic auto-fluorescence. These merits show the potentiality of g-C_3N_4 QDs in various applications such as biosensing, bioimaging, and photodynamic therapy.

The distinctive PL properties of g-C_3N_4 QDs have been correlated to their synthesis, chemical composition, and surface treatment. The PL property of g-C_3N_4 QDs has been proposed as a means to explain how g-C_3N_4 QDs interact with photons. g-C_3N_4 QDs exhibit tunable optical properties due to their unique electronic structure that can be altered by changing their physical and chemical properties. For example, Jiang et al. [78] demonstrated that phosphorus-doping into the g-C_3N_4 lattice can effectively engineer the bandgap of g-C_3N_4 QDs. Phosphorus-doped g-C_3N_4 QDs can be produced using a straightforward hydrothermal approach (**Fig. 8a**). As shown in **Figs. 8b-d**, if the doping concentration is increased, a greater number of p electrons are injected, leading to a further narrowing of the bandgap (**Fig. 8d**). Changing the doping concentration of phosphorus-doped g-C_3N_4 QDs allows for the emission wavelength to be tuned across the whole visible spectrum from 385 to 762 nm (**Figs. 8b** and **8c**). A quantum yield greater than 90% is achieved because of the direct bandgap that is present in phosphorus-doped g-C_3N_4 QDs. Changing the molar ratio of urea-to-sodium citrate precursors from 3:1 to 6:1, 9:1, and 12:1 allows for tunable emission from g-C_3N_4 QDs (**Figs. 9d** and **9e**). Fluorescent emission shifts from green to dark blue at the same excitation wavelength of 365 nm when sodium citrate concentration is increased. The fluorescence spectra of g-C_3N_4 QDs synthesized by varying the molar ratios of precursors (**Fig. 9f**) show distinct emission peaks at 450 nm, 467 nm, 536 nm, and 526 nm, respectively, confirming the tunable emission property. The sodium citrate serves as the carbon source and yields g-C_3N_4 QDs with negative surface functional groups (carboxyl and hydroxyl groups). The fluorescent behavior is strongly dependent on the surface states of g-C_3N_4 QDs, in a manner that is similar to that of carbon dots and graphene QDs (GQDs) [15,152–155].

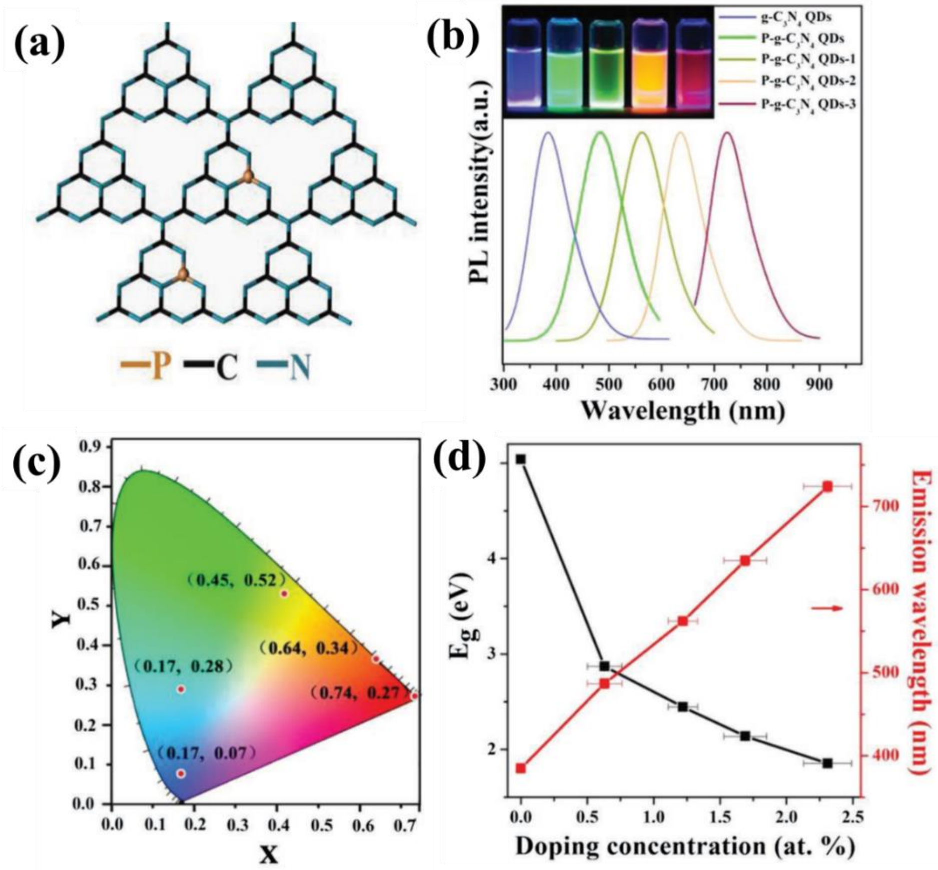

Fig. 8. Band gap tuning of phosphorus-doped g-C_3N_4 QDs. (a) PL spectra of g-C_3N_4 QDs and P-g-C_3N_4 QDs obtained by varying doping concentration. Inset: Photograph of the g-C_3N_4 QDs and P-g-C_3N_4 QDs in aqueous solution under the illumination UV light. b) CIE coordinates of g-C_3N_4 QDs and P-g-C_3N_4 QDs in aqueous solution. c) Relationship between emission maxima, bandgap (E_g) and doping concentration of P-g-C_3N_4 QDs. Reproduced with permission from [78].

Changing the molar ratio of the two reactants by varying the quantity of sodium citrate alters the content of carbon- and oxygen-rich groups, thereby influencing the surface states of g-C_3N_4 QDs. The emission peak of g-C_3N_4 QDs is red-shifted from 467 to 574 nm, if the excitation wavelength is changed from 360 nm to 500 nm **(Fig. 9a** and **Fig. 9b)** [58]. The fluorescence emission of g-C_3N_4 QDs is excitation-dependent, which is similar to the majority of luminous carbon dots and GQDs due to the optical selection of different-sized nanoparticles (quantum effect) and different emissive traps on the surfaces of g-C_3N_4 QDs (**Fig. 9c**) [15,145,150,156–159]. In the vast majority of cases, the PL emission wavelength of g-C_3N_4 QDs produced through various methods is red-shifted with respect to the excitation wavelength, and the emission intensity changes with an increase in the excitation wavelength [53,58,78,112]. For example, Sen Liu et al. [99] reported that fluorescent g-C_3N_4 QDs synthesized by the polymerization of CCl_4 and 1,2-ethylenediamine exhibit excitation wavelength-dependent PL emission ranging from 430 to 550 nm, corresponding to the excitation wavelengths ranging from 360 to 540 nm, respectively. This excitation wavelength-dependent PL behavior was also observed by other groups.

Overall, a higher degree of homogeneity in size and composition would lead to excitation wavelength-independent PL emission. This is true for g-C_3N_4 QDs that are synthesized from materials with a higher degree of crystallinity, since they do not contain any defects or put differently, have a high degree of homogeneity. An excitation wavelength-independent feature was found for g-C_3N_4 QDs in a few investigations, which is an important fact to take into consideration. For example, Cui et al. [139] and Han et al. [85] found that the intensity of PL emission changed, but the emission wavelength remained the same, when the excitation wavelengths for phenyl-modified g-C_3N_4 QDs and g-C_3N_4 QDs are increased from 300 to 400 nm and from 310 to 380 nm, respectively. In other studies, g-C_3N_4 QDs exhibited a pH-dependent PL feature, and the pH environment was found to have different effects on the PL emission intensity and wavelength of g-C_3N_4 QDs synthesized by different protocols [75,99,109,112,160]. This is because the pH environment affects the g-C_3N_4 QDs differently, depending on the method used to prepare them. Interestingly, Ting et al. [129] reported dual color emissive g-C_3N_4 QDs, synthesized via solid-phase reaction treatment at 195 °C using a precursor. When exposed to the UV (365 nm) light, the g-C_3N_4 QDs show bright white emission (**Fig. 10a**), and when the UV light is turned off, yellow phosphorescence emission is observed at ambient conditions (**Fig. 10b**). **Fig 10d** shows the prompt PL spectra of g-C_3N_4 QDs, which exhibit characteristic dual emission bands of blue-yellow fluorescence and phosphorescence, centered at 440 and 520 nm, respectively. The delayed spectra of g-C_3N_4 QDs display a single band at 570 nm. This finding demonstrates that the emission band observed at 440 nm is a transient emission. As a result, the short-lived and long-lived species are both involved in the process of light emission. Time-resolved decay curves confirm the presence of both short-lived and long-lived species, with lifetimes of 3.8 ns and 235 ms, respectively, under ambient conditions (**Fig. 10e**). Under low-temperature reaction conditions, carbonyl groups (–C-O) are generated at the rim of the g-C_3N_4 QDs rather than amino groups (–NH_2). This plays a key role in promoting intersystem crossing (ISC) and inducing intermolecular electronic coupling, which yields intense yellow phosphorescence emission (**Fig. 10f** and **Fig. 10g**).

Fluorescence quantum yield (PLQY) is an important parameter that, along with PL wavelength, determines the utility of g-C_3N_4 QDs as imaging probes and active components in optoelectronic and bioimaging applications. PLQY is defined as the ratio of photons emitted by a PL molecule to photons absorbed by the molecule at the excitation wavelength [15,161–163]. A relative PLQY is calculated by comparing the absorbance and emission of a molecule to a molecular dye with a known PLQY and a similar PL emission window. There has been a wide range of relative PLQY values reported for g-C_3N_4 QDs, ranging from 14.5 to 96% [58,78,104,129,132,138,159].

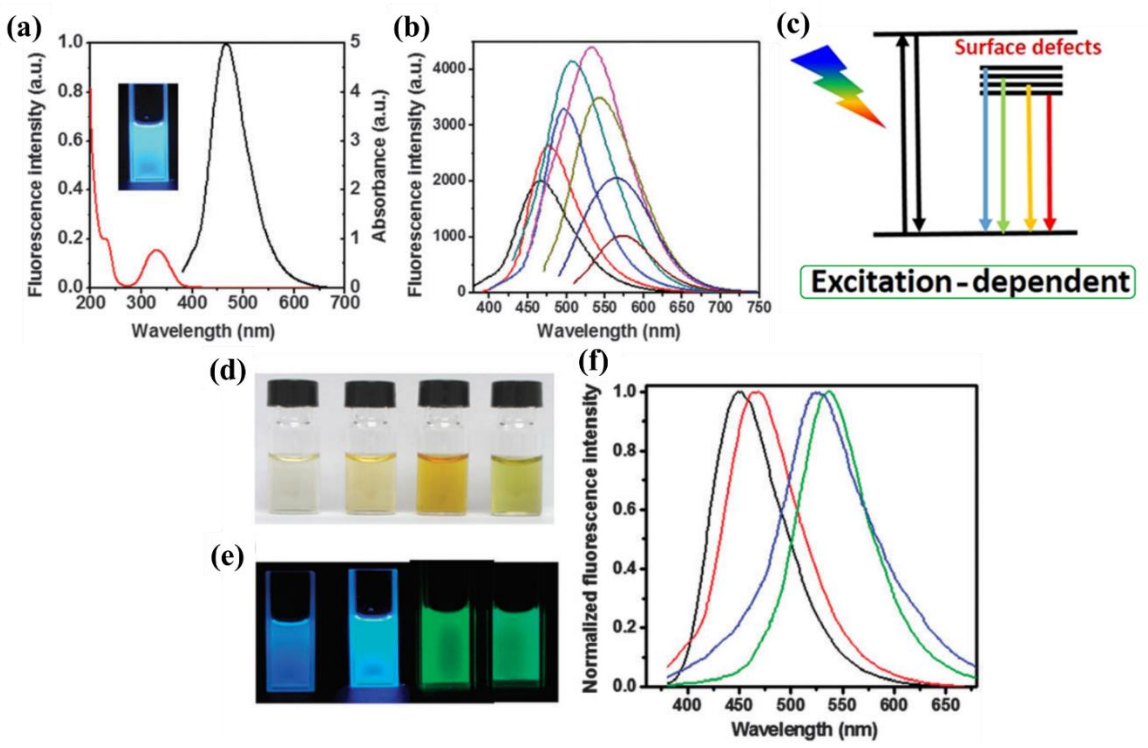

Fig. 9. (a) UV & PL emission spectra of g-C_3N_4 QDs, (b) excitation dependent emission spectra, Reproduced with permission from [58]. (c) Schematic illustration of passivation of states. Reproduced with permission from [159]. Tunable emission property of g-C_3N_4 QDs with different molar ratios of two precursors, (d) photograph of g-C_3N_4 QDs in water under visible light and (e) 365 nm UV light, (f) corresponding PL spectra of g-C_3N_4 QDs excited at 365 nm. Reproduced with permission from [58].

In recent years, upconversion photoluminescence (UCPL) has received considerable interest. It refers to an optical process, where high-energy photons are emitted when the molecule absorbs two or more low-energy photons, and is caused by anti-Stokes luminescence, i.e., the excitation wavelength is longer than the emission wavelength [164–168]. UPCL emission has been observed in g-C_3N_4 QDs in several studies. Long-wavelength light (705–862 nm) was used by Wang et al. [47] to excite g-C_3N_4 QDs that were obtained from a hydrothermal cutting process. They observed luminescence in the range of 350 to 600 nm, with the strongest emission occurring at 440 nm. This suggests that g-C_3N_4 QDs have UCPL properties. Yang et al. [131] also observed that g-C_3N_4 QDs emit visible light (350–600 nm) with the strongest emission at 450 nm when exposed to the NIR light (700–820 nm). This again proves that g-C_3N_4 QDs have UCPL properties. There are two possible ways to explain the upconversion emission mechanism: the multiphoton active process and the anti-Stokes photoluminescence. Several researchers have addressed that the upconversion emission of g-C_3N_4 QDs is caused by the multiphoton active process due to the energy difference between the light that excites the material and the light that it gives off. But in the future, more studies are needed to fully unravel the relevant intrinsic mechanisms.

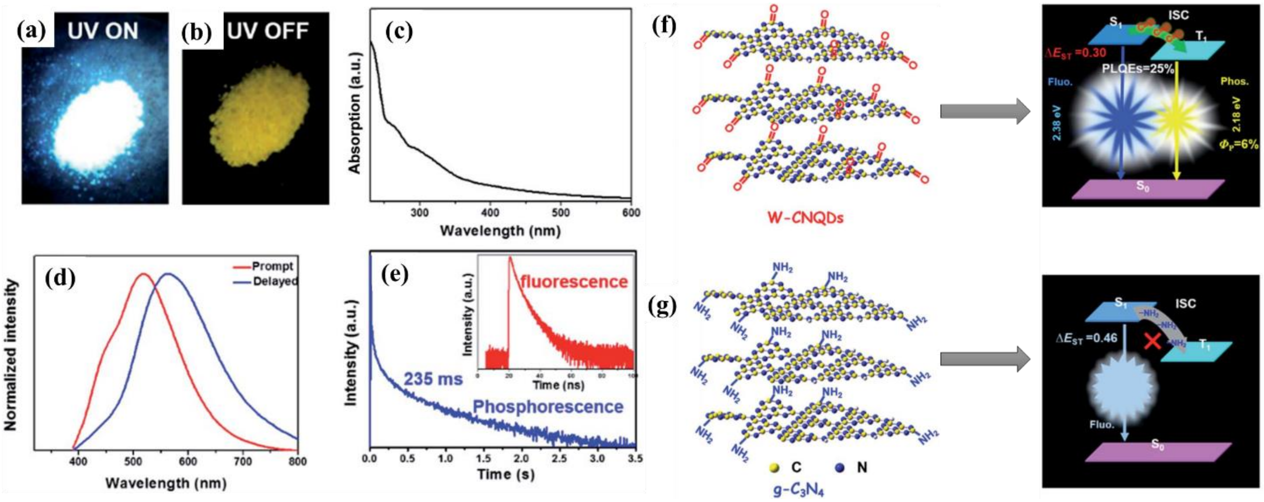

Fig. 10. Photograph of g-C_3N_4 QDs under UV light on (a) and off (b). Absorption spectrum (c), Prompt (red line) and delayed (blue line, 5 ms) PL spectra (d) excited at 380 nm. Time-resolved decay spectra (e) measured at 520 nm for long lifetime and at 440 nm for short lifetime (inset) of g-C_3N_4 QDs. Schematic illustration of the chemical structures and energy-level diagrams of the corresponding photophysical processes of (f) g-C_3N_4 QDs and (g) g-C_3N_4 (S_0: ground state, S_1: singlet excited state, T_1: triplet excited state, ΔE_{ST}: energy gap, ISC: intersystem crossing). Reproduced with permission from [129].

Density functional theory (DFT) calculations provide significant theoretical predictions and guidance for g-C_3N_4 QDs with respect to their electronic, optical, and photocatalytic properties. For example, Ting et al. [129] performed time-dependent DFT calculations of white light-emitting g-C_3N_4 QDs and conventional g-C_3N_4 to confirm the mechanism of yellow phosphorescence observed in g-C_3N_4 QDs. The calculated ΔE_{ST} of white light-emitting g-C_3N_4 QDs (0.32eV), which is smaller than the traditional g-C_3N_4 (amino groups at the rim) (0.42eV), allows for an effective ISC process from S_1 to T_1 states (**Fig. 10f** and **Fig. 10g**). In addition, the higher number of energy transition channels in g-C_3N_4 QDs (carbonyl groups at the rim; five channels; $S_1 \rightarrow T_1$, T_2, T_4, T_5, T_6), as compared to the conventional g-C_3N_4 (three channels; $S_1 \rightarrow T_1$, T_4, T_5) also contributes to the enhanced ISC (**Fig. 11a** and **Fig. 11b**). It is generally known that charge transfer characteristics can result in a small ΔE_{ST} when hole natural transition orbitals (NTOs) and electron NTOs are spatially separated (**Fig. 11c** and **Fig. 11d**) [169]. It is hypothesized that the intense phosphorescence emission can be attributed to the carbonyl groups, boosting the ISC and inducing intermolecular electronic coupling [170]. In a relevant work, Xiaodong et al. [53] performed DFT calculations to investigate the π-conjugated electronic structure of g-C_3N_4 with different layers. **Figs. 11e-h** show the highest occupied molecular orbital (HOMO)–lowest unoccupied molecular orbital (LUMO) transition, which is attributed to the π-π* charge transfer of g-C_3N_4 and is essential for the two-photon absorption (TPA) characteristics of the molecules. The stabilities of single- and double-layer molecules are indicated by the large negative values. Compared to its equivalents with fewer layers, the single-layer form of g-C_3N_4 exhibits the highest degree of reactivity. Therefore, lowering the lateral size and thickness of g-C_3N_4 to a single C-N layer enables its penetration through the cell membranes and entering the nucleus, thereby displaying TPA characteristics (**Figs. 11i-k**). The wide bandgap of g-C_3N_4 limits its efficiency in photocatalytic and solar cell applications. Arkamita et al. [84] investigated a variety of strategies for overcoming these obstacles by tailoring the size, substrate, functionalization, and doping of hydrogen-passivated g-C_3N_4 QDs (**Figs. 11 l-r**) [171–173]. Comprehensive DFT-based computations is performed, revealing that modified g-C_3N_4 QDs have more effective visible or NIR light responses compared to pure g-C_3N_4 QDs, making them better functional materials for solar cell or photocatalytic applications. The passivated g-C_3N_4 QDs have shown improved catalytic activity in the H_2 evolution reaction compared to the original g-C_3N_4 QDs. In addition, these g-C_3N_4 QDs are well-suited for use in solar cell applications due to the width of the optical gap they exhibit.

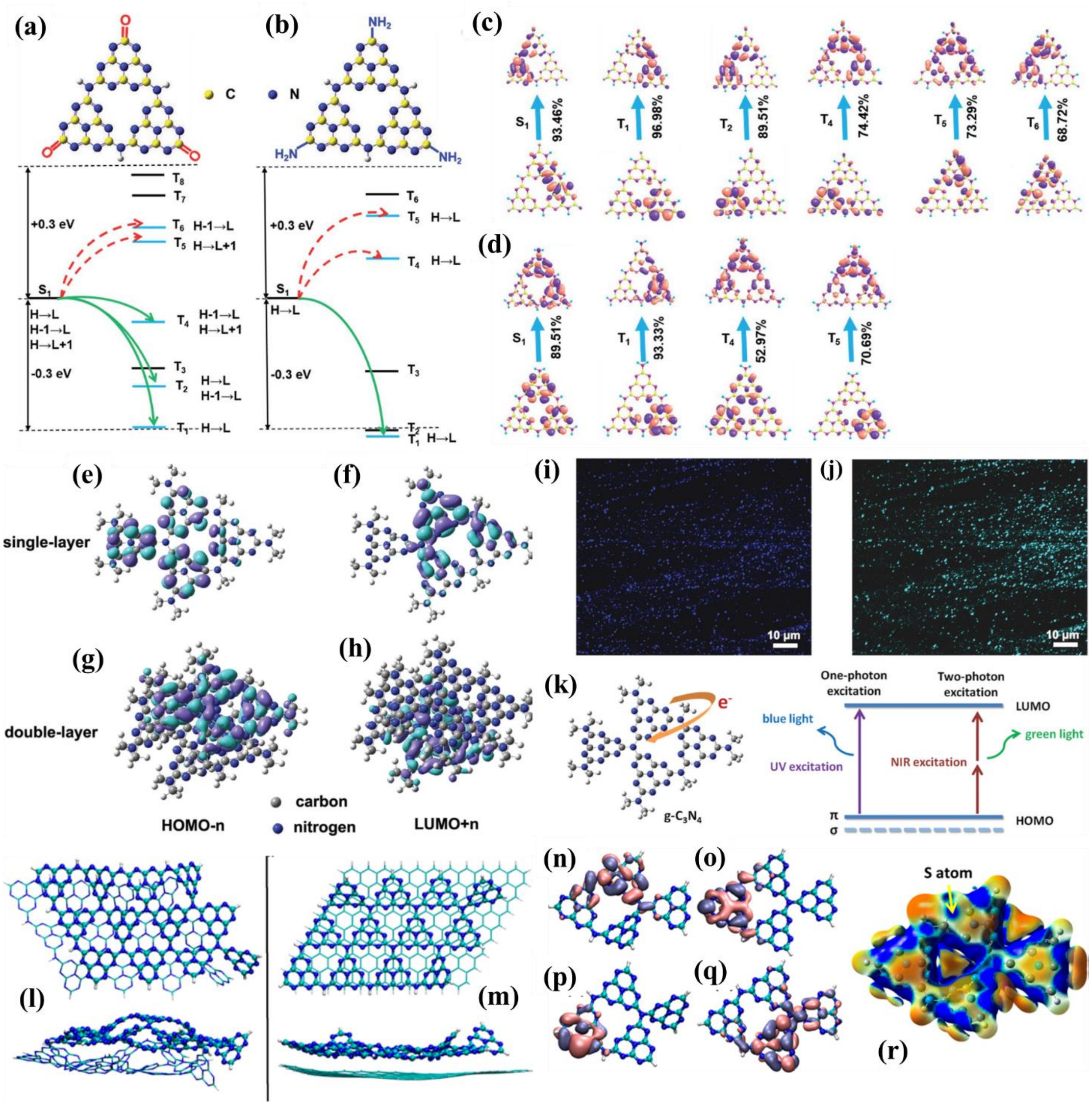

Fig. 11. Schematic illustration of the TD-DFT calculated energy level diagrams, main orbital configurations and expected ISC channels of (a) g-C_3N_4 QDs and (b) g-C_3N_4 in the singlet (S_1) and Triplet (T_n) energy states. H and L denotes to HOMO and LUMO, respectively. NTO diagrams (hole orbitals (bottom) and electron orbitals (top)) of (c) g-C_3N_4 QDs and (d) g-C_3N_4. Reproduced with permission from [129]. HOMO-n and LUMO+n orbital diagrams of the single layered (e&f) and double layered (g&h) g-C_3N_4 respectively. One (i) and two-photon (j) luminescence image of g-C_3N_4 QDs dispersed in a glass substrate, respectively. (k) Schematic illustration of one and two-photon excited fluorescence of g-C_3N_4 QDs. Reproduced from Ref. [53] with the permission from Royal Society of Chemistry. Effect of substrates: Top and side views of (l) bilayer b-C_3N_4 QDs and (m) b-C_3N_4 QD+GQD. Effect of S or P doping leads to charge transfer from the dopants: (n) SOMO of S−C_3N_4 QD_{ed}, (o) SOMO of S−C_3N_4 QD_{mid}, (p) SOMO of P−C_3N_4 QD_{ed}, and (q) SOMO of P−C_3N_4 QD_{mid}. (r) Electrostatic potential (ESP) plot of S−C_3N_4 QD_{ed}; the red parts indicate electron-rich, and the blue part indicates electron-deficient sites. Reproduced with permission from [84].

4. Applications of g-C_3N_4 QDs

4.1. Photocatalysis

g-C_3N_4 QDs with semiconducting properties with optical absorption in the visible light spectrum are commonly utilized as photosensitizers in conjunction with conventional wide-gap photocatalysts that are solely responsive to UV light. This is done to augment the efficacy of solar radiation for photocatalytic processes. The favorable solubility in water and chemical robustness of g-C_3N_4 QDs may facilitate the production of g-C_3N_4 QD hybrid materials on a large scale. Furthermore, g-C_3N_4 QDs are conjoined with photocatalysts that are activated by visible light to broaden the spectral responsive range of the photocatalytic system toward the NIR region, thanks to the upconversion PL characteristics of g-C_3N_4 QDs. Certain semiconductors have a conductive band potential that is in close proximity to or surpasses that of $O_2/{\cdot}O_2^-$. This can have a detrimental effect on the generation of ${\cdot}O_2^-$, a highly reactive species that plays a crucial role in the photocatalytic process [174]. The construction of hybrid photocatalysts using g-C_3N_4 QDs has the potential to enhance the photocatalysis process and increase the production of CO_2 due to the significantly lower conduction band potential of g-C_3N_4 QDs [114,175]. In addition, the heterojunctions that arise from the combination of g-C_3N_4 QDs and other semiconductors exhibit the capacity to impede the recombination of electrons and holes, thereby elevating the efficiency of charge separation. This is due to the fact that the photoinduced g-C_3N_4 QDs can function simultaneously as proficient electron donors and acceptors [77]. The utilization of g-C_3N_4 QD compounds as photocatalysts is a viable approach to enhance the photocatalytic reactions. To date, several composite photocatalysts utilizing g-C_3N_4QD have been synthesized and utilized for a range of applications, including hydrogen evolution, environment remediation, and organic pollutant photodegradation.

As it is known in the literature, Titanium dioxide (TiO_2) is a widely used photocatalyst due to its favorable attributes such as excellent stability, cost-effectiveness, proficient charge transfer, and non-toxicity. The potential application of TiO_2 in photocatalysis is restricted due to its wide band gap (3.0-3.2 eV), which primarily exhibits photoactivity under UV irradiation. Efforts have been undertaken to develop composites of g-C_3N_4 QDs/TiO_2 in order to tackle the problem of organic contamination. For instance, Li et al. [175] produced a range of hybrid photocatalysts consisting of Z-scheme rutile TiO_2 (rTiO_2) that were loaded with varying quantities of g-C_3N_4 QDs (g-C_3N_4 QDs-rTiO2). These photocatalysts were utilized for the purpose of visible-light-driven photocatalytic degradation of Rhodamine B (RhB) and NO oxidation. The utilization of hybrid catalysts resulted in significantly improved removal efficiencies of RhB and NO in comparison to pure g-C_3N_4 and rTiO2 (**Figs. 12a-c**). Notably, the hybrid catalyst with 15 wt% QDs exhibited the most optimal photocatalytic performance among all the hybrid catalysts. The enhancement of visible-light absorption and consequent generation of photo-induced electrons and holes is facilitated by the integration of g-C_3N_4 QDs (**Fig. 12d**). The transfer of photo-induced electrons from the conduction band (CB) of rTiO_2 to the valence band (VB) of g-C_3N_4 QDs, followed by their excitation to the CB of g-C_3N_4 QDs, enables the separation of charge carriers. This is due to the distinct CB and VB edges of g-C_3N_4 QDs and rTiO_2. The electrons located in the conduction band of g-C_3N_4 QDs and the holes present in the valence band of rTiO_2 engage in a reaction with the adsorbed oxidant (O_2) and reductant (OH^-/H_2O), respectively. This reaction results in the production of $\cdot$OH and $\cdot O_2^-$ radicals, which possess a potent oxidizing ability. These radicals are accountable for the ensuing oxidation of pollutants. Furthermore, a number of scholars have documented the heightened photocatalytic efficacy of TiO_2 nanotubes arrays (NTAs) that have been modified with g-C_3N_4 QD as either a membrane or electrode in the process of decomposing organic pollutants when exposed to visible light [65,80,114,176].

In another study conducted by Su et al. [114], it was observed that simulated solar light exposure led to the removal of RhB and phenol by almost 100% using a g-C_3N_4 QDs/TiO_2 NTA photoanode within 120 and 180 minutes, respectively. In contrast, the TiO_2 NTA electrode only degraded 50% of RhB and 30.1% of phenol under identical conditions. The heterostructured photocatalyst comprising of g-C_3N_4 QDs/TiO_2 NTAs exhibits improved photocatalytic activity. The g-C_3N_4 QDs function as photosensitizers, thereby increasing the yield of charge carriers by harvesting visible phonons. Additionally, the interfacial interaction between g-C_3N_4 QDs and TiO_2 NTAs plays a crucial role in retarding the electron-hole pair recombination, further enhancing the photocatalytic activity of the composite. **Fig. 12e** illustrates the mechanism of photocatalysis for the degradation of pollutants over the electrode of g-C_3N_4 QDs/TiO_2 NTA. The transportation of photogenerated electrons from the conduction band of g-C_3N_4 QDs to the conduction band of TiO_2 NTAs, followed by their transfer to the negative electrode for the purpose of generating $\cdot$OH to mineralize pollutants, is observed. Additionally, the photogenerated holes in the valence band of g-C_3N_4 QDs are observed to react with OH- or H_2O to produce $\cdot$OH, which is utilized for the oxidation of pollutants.

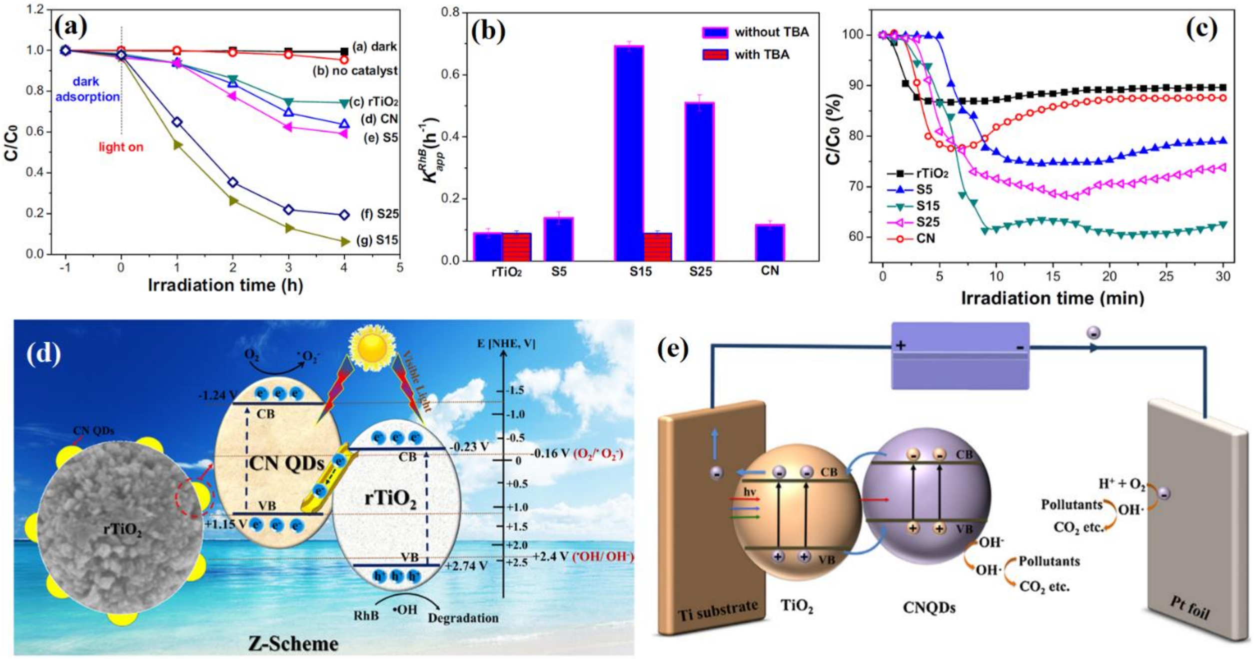

Fig. 12. (a) Photocatalytic degradation profiles of RhB by different g-C_3N_4 QDs-rTiO_2. (b) comparison of the corresponding rate constants. (c) NO removal efficiencies in a single-pass flow of air over different g-C_3N_4 QDs-rTiO_2 under visible-light irradiation. (d) photodegradation mechanism of g-C_3N_4 QDs-rTiO_2 hybrids for RhB degradation and NO removal under visible-light irradiation. Reproduced with permission from [175]. (e) illustrative representation of charge separation and pollutants degradation processes using -C_3N_4 QDs/TiO_2 NTAs photoanodes under solar light. Reproduced with permission from [114].

Another work harnessing the heterojunction between g-C_3N_4 QDs and TiO_2 is that of Guo et al. [54], where the group investigated the degradation process of bisphenol A (BA) dye and the production of H_2 through the utilization of a composite photocatalyst consisting of g-C_3N_4 QDs/TiO_2 with different g-C_3N_4 QDs loadings under visible-UV light. The maximum surface area achieved for g-C_3N_4 QDs-1.5/TiO2 was 38.76 m^2/g, whereas the highest surface area attained for unprocessed TiO_2 was 35.7 m^2/g. The impact of varying volumes (ranging from 0.5 to 2.5 mL) of g-C_3N_4 QDs solution on the photocatalytic performance of BA degradation was examined. The efficiency of the photocatalytic process exhibited by the g-C_3N_4 QDs/TiO_2 catalyst was observed to augment as the proportion of g-C_3N_4 QDs was increased up to a certain optimal level. The degradation efficiency of BA by the g-C_3N_4 QDs/TiO_2 catalysts was found to decrease upon excessive generation of photo-produced electron holes and inhibition of photo-produced charge carriers. The optimal conditions for achieving the highest degradation efficiency of BA were determined to be an operating time of 80 min, an initial BA concentration of 10 mg/L, and a light intensity of 100 mW/cm^2, utilizing 50 mg of the g-C_3N_4 QDs-2/TiO_2 catalyst. This combination resulted in a degradation efficiency of 100%. Additionally, the study evaluated the H_2 production potential under visible-UV light and found that the $g\text{-}C_3N_4$ QDs-2/TiO_2 sample exhibited a maximum H_2 generation of 120 μmol/h.g.

Other inorganic semiconductors have been used as hybridizing agents with $g\text{-}C_3N_4$ QDs to produce either binary or ternary photocatalysts such as MoS_2, Fe_3O_4, $BiPO_4$, $InVO_4$, $BiVO_4$, Bi_2WO_6, $Bi_2Ti_2O_7$, Bi_2MoO_6, and so on [68,72,77,177–179]. For instance, the study conducted by Zarei et al. [177] involved the utilization of MoS_2 nanosheets as a substrate for the deposition of Fe_3O_4 and $g\text{-}C_3N_4$ QDs, resulting in the development of a highly efficient $MoS_2/Fe_3O_4/g\text{-}C_3N_4$ QDs ternary photocatalyst. The primary objective of this research was to investigate the efficacy of the aforementioned hybrid material in the photocatalytic degradation of methyl orange (MO) and methylene blue (MB) dyes present in water. The study examined the impact of varying operating time (ranging from 20 to 60 min), initial pH levels (ranging from 4 to 10), initial dye concentration (ranging from 10 to 40 mg/L), and photocatalyst mass (ranging from 5 to 50 mg) on the photodegradation efficacy under LED irradiation. The experimental results of this work indicated that the optimal conditions for achieving the highest removal efficiency of MO were an initial pH of 4, an operating time of 20 min, an initial MB concentration of 10 mg/L, and a catalyst amount of 10 mg. The observed MO removal efficiency was 99.7%, with a corresponding degradation rate constant of 0.285 min^{-1}. The study yielded a maximum removal efficiency of 99.5% for MO with a rate constant of 0.263 min^{-1}. This was achieved under specific conditions, including an initial pH of 4, an operating time of 40 min, an initial MO concentration of 40 mg/L, and a catalyst amount of 40 mg. The study delved deeper into the recyclability and efficacy of the produced photocatalyst through the treatment of 10 mg/L of MO and MB dyes over six cycles. At the conclusion of the initial and sixth cycles, the removal efficiencies for MB were 99% and 24%, respectively. A comparable pattern was noted with regards to the MO elimination efficacy, whereby the efficacy of elimination, which was 84% following the initial cycle, declined to 22% by the sixth cycle. The observed outcomes during the reusability experiments can be attributed to the reduction of Fe_3O_4 and $g\text{-}C_3N_4$ QDs.

Bismuth phosphate, denoted as $BiPO_4$, is an emerging photocatalyst that belongs to the class of oxy-acid salts. This photocatalyst exhibits a broader band gap of 3.85 eV and superior photocatalytic performance to TiO_2. Li et al. [178] developed a binary structure consisting of $g\text{-}C_3N_4$ QDs and $BiPO_4$ nanocrystals to expand the exploitable spectrum of $BiPO_4$. The visible light-induced photocatalytic performance of this composite was evaluated using MO as the target pollutant. g-C_3N_4 QDs/$BiPO_4$ demonstrated a degradation efficiency of 92% within a time frame of 180 min, with a degradation rate constant of 0.0135 min^{-1} (**Fig. 13a**). This value is significantly greater than the degradation efficiency achieved by $BiPO_4$ nanocrystals, which was less than 10%, and pure g-C_3N_4, which achieved a degradation efficiency of 75% with a degradation rate constant of 0.0079 min^{-1} (**Fig. 13b**). The g-C_3N_4 QDs/$BiPO_4$ composite exhibits a significantly greater specific surface area (39.4 m^2 g^{-1}) compared to pristine $BiPO_4$ nanocrystals (8.3 m^2 g^{-1}). This property is advantageous for facilitating the adsorption of pollutants onto the photocatalyst and increasing the availability of active sites. Conversely, the formation of heterojunctions between g-C_3N_4 QDs and $BiPO_4$ nanocrystals results in a noteworthy improvement in the separation and transportation of charge carriers within the composite catalyst. The composite catalyst of g-C_3N_4 QDs/$BiPO_4$ exhibits notable stability up to four cycles (**Fig. 13c**). The proposed mechanism consists of electron transfer from the CB of g-C_3N_4 QDs to that of $BiPO_4$, which was facilitated by the more negative CB and VB edge potentials of g-C_3N_4 QDs in comparison to those of $BiPO_4$. The photogenerated holes on $BiPO_4$ exhibit direct transfer to g-C_3N_4, thereby increasing charge separation efficiency and reducing the likelihood of photo-generated electron-hole recombination (**Fig. 13d**).

As mentioned above, bismuth complex oxides/g-C_3N_4 QDs have emerged as promising photocatalysts in recent years due to their adequate absorption of visible light and high photocatalytic efficiency thanks to the established heterojunction. Zhang and colleagues [68] created a photocatalyst with a direct Z-scheme by incorporating g-C_3N_4 QDs onto ultra-thin Bi_2WO_6 nanosheets. This photocatalyst was utilized for the removal of RhB and tetracycline (TC) under illumination from a broad-spectrum light source. The study conducted by the authors revealed that the introduction of g-C_3N_4 QDs in varying quantities resulted in an enhancement of the photocatalytic activity of Bi_2WO_6 nanosheets in the degradation of pollutants under visible and NIR light irradiation. The composite catalyst, specifically the one with a loading amount of 5 wt.% g-C_3N_4 QDs (5% g-C_3N_4 QDs/Bi_2WO_6), demonstrated the highest photocatalytic activity among all the samples (**Fig. 13e** and **Fig. 13f**). The study found that the degradation efficiency of TC was notably higher when using 5% g-C_3N_4 QDs/Bi_2WO_6 compared to neat Bi_2WO_6 nanosheets under the NIR light irradiation. This was observed to be approximately twice as effective (**Fig. 13g**) and can be attributed to the up-conversion photoluminescence (UCPL) behavior of g-C_3N_4 QDs. The article presents a proposed Z-scheme mechanism for the photocatalytic degradation of organic pollutants over g-C_3N_4 QDs/Bi_2WO_6, as illustrated in **Fig. 13h**. When exposed to visible light, the photogenerated electrons located in the CB of Bi_2WO_6 have the ability to transfer to the HOMO of g-C_3N_4 QDs. This transfer effectively suppresses the recombination of the photogenerated carriers. Additionally, the remaining electrons and holes located in the LUMO of g-C_3N_4 QDs and the VB of Bi_2WO_6 can facilitate the formation of ROSs ($\cdot OH$ and $\cdot O_2^-$) that are capable of attacking organic pollutants. The capacity of the VB of Bi_2WO_6 to oxidize organics is attributed to the elevated VB edge of the material. The enhanced efficiency of charge separation results in the accumulation of additional electrons and holes within the composite material. This accumulation subsequently generates a greater number of reactive species, which leads to an improved removal of organic pollutants. The utilization of g-C_3N_4 QDs as a spectral converter under the NIR light irradiation results in the generation of visible light emission, owing to their UPCL characteristics. A comparable process of photocatalytic degradation was also observed akin to the one observed under the irradiation by visible light.

In addition to the previously discussed composite catalysts constructed from binary g-C_3N_4 QDs, photocatalysts with superior performance have been additionally synthesized by assembling ternary materials involving g-C_3N_4 QDs. The ternary compound system exhibits a minimum of two contact interfaces, thereby facilitating a more efficient separation of photogenerated electrons and holes, ultimately leading to an enhanced photocatalytic performance. Several investigations have shown the enhanced photocatalytic degradation of organic contaminants utilizing ternary compounds based on g-C_3N_4 QD. In their work, Li and colleagues [77] synthesized a composite photocatalyst consisting of leaf-like $InVO_4$/$BiVO_4$ nanocrystals and g-C_3N_4 QDs assembled on their surface. They evaluated the photocatalytic performance of this composite material with respect to the degradation of RhB. Their findings demonstrated that the g-C_3N_4 QDs/$InVO_4$/$BiVO_4$ composite exhibits superior photoactivity compared to both single- and two-component samples. Specifically, under the visible light irradiation, the ternary composite achieves full elimination of RhB within a 40-minute timeframe with a reaction rate constant of 0.120 min^{-1} (**Fig. 13i** and **Fig. 13j**). Moreover, the stability testing results revealed that the degradation rate of the ternary photocatalyst showed slightly decrease after the continuous five-run repeated irradiation within 280 min (**Fig. 13l**). The plausible mechanisms for the dispersion and movement of photoinduced carriers within the ternary compound were also discussed. In general, there exists multiple potential routes that could be taken into account for the production of charge carriers. Upon simultaneous excitation of $BiVO_4$ and $InVO_4$ under the visible light irradiation, the photogenerated electrons in the CB of $InVO_4$ undergo electron transfer I into the CB of $BiVO_4$. This is due to the more negative CB of $InVO_4$ in comparison to that of $BiVO_4$. Concurrently, the photogenerated holes located in the VB of $BiVO_4$ flow into the VB of $InVO_4$, denoted as hole transfer I: $BiVO_4/InVO_4$, due to the comparatively more negative VB of $InVO_4$ in relation to $BiVO_4$. Subsequently, the electrons that are generated by the photoexcitation process in the CB of g-C_3N_4 QDs can undergo two distinct pathways for electron transfer. The first pathway involves the transfer of electrons from the CB of g-C_3N_4 QDs to the CB of $InVO_4$ (electron transfer II: g-C_3N_4 QDs/$InVO_4$). Alternatively, the electrons can directly migrate to the CB of $BiVO_4$ (electron transfer III: g-C_3N_4 QDs/$BiVO_4$). Concurrently, there exists hole transfers from the VB of $InVO_4$ to that of g-C_3N_4 QDs (referred to as hole transfer II: $InVO_4$/g-C_3N_4 QDs) and from the VB of $BiVO_4$ to that of g-C_3N_4 QDs (referred to as hole transfer III: BiVO4/CNQDs). It is postulated that the mechanisms governing the aforementioned transfers exhibit greater celerity in comparison to the electron-hole recombination process occurring between the VB and CB of bismuth vanadate, indium vanadate, or carbon nitride QDs. The transfer of charges has the potential to decrease the recombination of electron-hole pairs, leading to an extension in the lifespan of charges and ultimately enhancing the photocatalytic efficacy. Moreover, the generation of ·OH radicals for the degradation of organic pollutants using the g-C_3N_4 QDs/$InVO_4$/$BiVO_4$ photocatalyst is challenging due to the slightly higher VB potential of $BiVO_4$ in comparison to OH^-/·OH. This observation aligns with the outcomes of quenching experiments demonstrating that $\cdot O_2^-$ radicals constitute the primary species that are reactive in the photodegradation (**Fig. 13k**).

Subsequent research by Lin et al. [72] on nanoheterostructured Bi_2MoO_6 nanosheets deposited with Ag and g-C_3N_4 QDs demonstrated the superior performance of ternary composite photocatalysts based on g-C_3N_4 QDs compared to the corresponding binary composite systems. Compared to pure Bi_2MoO_6, Ag/Bi_2MoO_6, and g-C_3N_4 QDs/Bi_2MoO_6, the as-prepared g- C_3N_4 QDs/Ag/Bi_2MoO_6 composite removes 100% of RhB in 30 min under visible light irradiation. The g-C_3N_4 QDs and Bi_2MoO_6 in this ternary compound absorb visible light as photosensitizers, and the Ag bandgap accepts electrons from the CB of Bi_2MoO_6 and holes from the VB of g-C_3N_4 QDs, forming an electron-conduction bridge. Both g-C_3N_4 QDs and Bi2MoO_6 exhibit remarkable acceleration of photoinduced electron and hole separation during photocatalysis, which aids in the degradation of RhB. The visible light absorption of the composite was improved by the surface plasmon resonance of Ag, which was helpful for the photocatalytic activity (significantly greater than pure Bi_2MoO_6, Ag/Bi_2MoO_6, and g-C_3N_4 QDs/Bi_2MoO_6 after 30 min of visible light irradiation). The g-C_3N_4 QDs and Bi_2MoO_6 in this ternary compound absorb visible light as photosensitizers, and the Ag bandgap accepts electrons from the CB of Bi_2MoO_6 and holes from the VB of g-C_3N_4 QDs, forming an electron-conduction bridge. Both g-C_3N_4 QDs and Bi_2MoO_6 exhibit remarkable acceleration of photoinduced electron and hole dissociation during photocatalysis, which aids in the degradation of RhB. In addition, the visible light absorption of the composite was improved by the surface plasmon resonance of Ag, which was advantageous for the photocatalytic activity.

In addition, scholarly literature documents the amalgamation of g-C_3N_4 QDs with alternative semiconductor materials for photocatalysis purposes, beyond the aforementioned metal oxide semiconductors. The photocatalytic efficacy of a composite material comprising of ultrathin g-C_3N_4 sheets embedded with g-C_3N_4 QDs (g-C_3N_4 QDs-utg-C_3N_4) and Sb_2S_3 under the NIR irradiation was reported by Wang et al. [92]. The utilization of g-C_3N_4 sheets and QDs presents an efficacious approach to enhance the photocatalytic performance of Sb_2S_3 through integration, thanks to their distinctive photoinduced electron transfer characteristics. The results presented in **Figs. 13m-o** indicate that the photocatalytic performance of g-C_3N_4QD composites toward MO degradation under light illumination ranging from UV to NIR region is improved with varying loadings of g-C_3N_4 QDs-utg-C_3N_4. The sample with 10 ml of g-C_3N_4 QDs-utg-C_3N_4 demonstrates a 70% removal of MO under the NIR irradiation within 120 min, owing to the UCPL characteristics of g-C_3N_4 QDs. This outcome is achieved by optimizing the loading amount of g-C_3N_4 QDs-utg-C_3N_4. **Fig. 13p** depicts a schematic representation of the process of photocatalytic degradation of MO on the g-C_3N_4 QDs-utg-C_3N_4/ Sb_2S_3 composite under the NIR illumination. The primary spectral converter in question is g-C_3N_4 QDs, which has the ability to absorb NIR light and convert it to shorter wavelength light. This process results in the generation of electrons and holes. Electrons are transferred from the CB of g-C_3N_4 to that of Sb_2S_3, while the VB of Sb_2S_3 receives holes that originate from g-C_3N_4. This process effectively impedes the recombination of the carriers. Subsequently, MO undergoes decomposition through the isolated holes, and the resultant production of $\cdot O_2^-$, which arises from the interaction between stimulated electrons and O_2 that is adsorbed on the Sb_2S_3 surface.

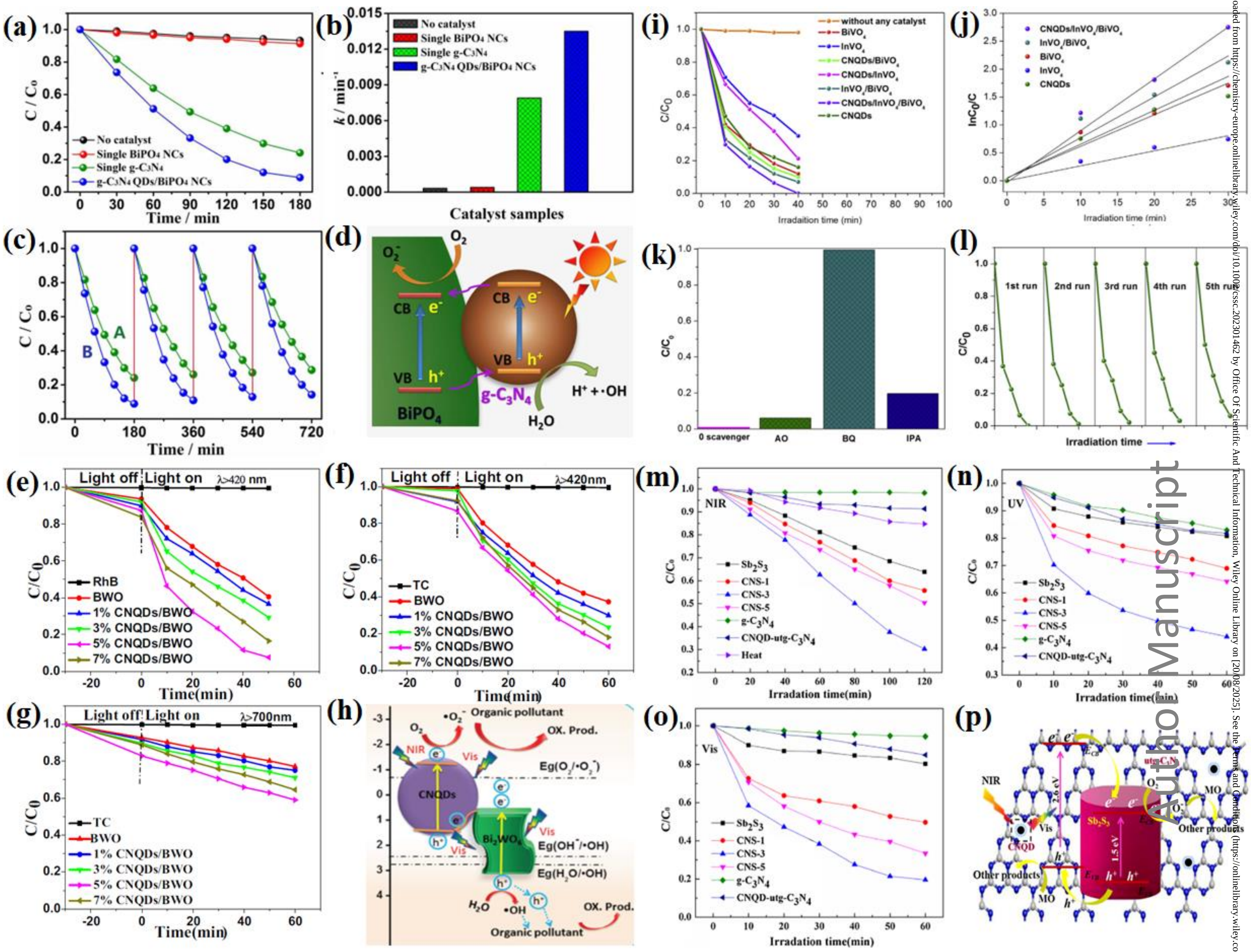

Fig. 13. (a, b) photo-induced catalytic activities and corresponding k of MO degradation using g-C_3N_4, $BiPO_4$, and g-C_3N_4 QDs/$BiPO_4$. (c) neat g-C_3N_4 (curve A) and g-C_3N_4 QDs/$BiPO_4$ reutilization (curve B). (d) mechanism of separation and transport of photogenerated electron–hole pairs at the g-C_3N_4 QDs/$BiPO_4$ interface. Reproduced with permission from [178]. Photo-induced degradation of (e) RhB under visible light irradiation, (f) TC under visible light irradiation; (g) TC under NIR light irradiation with different g-C_3N_4 QDs/BiWO samples. (h) Z-scheme mechanism g-C_3N_4 QDs/BiWO under wide spectrum light irradiation. Reproduced with permission from [68]. (i) Photodegradation efficiencies of RhB as a function of irradiation time for different $BiVO_4$, $InVO_4$, g-C_3N_4 QDs based single , binary, or ternary photocatalyst. (j) ln(C_0/C) versus time curves of RhB degradation over different $BiVO_4$, $InVO_4$, g-C_3N_4 QDs based single , binary, or ternary photocatalyst. (k) Active species determination by trapping experiments. (l) cycling runes of the photocatalytic degradation of Rh B over ternary sample under visible light irradiation. Reproduced with permission from [77]. MO photocatalytic degradation using different g-C_3N_4 QDs-utg-C_3N_4/ Sb_2S_3 hybrids under (m) NIR, (n) UV, (o) Vis. (p) Proposed mechanism for the MO degradation over the g-C_3N_4 QDs/$InVO_4$/$BiVO_4$ composites under NIR irradiation. Reproduced with permission [92].

4.2. Adsorption

It is acknowledged in the state of the art that the existence of primary/secondary amine moieties (C-NH_2 and C_2-NH) on the basal plane and edges within the structure of g-C_3N_4 QDs are attributed to the inadequate thermal polycondensation process, resulting in the formation of a limited quantity of hydrogen impurities. Therefore, it is apparent that the g-C_3N_4 QDs materials with surface defects and an abundance of electrons, exhibit a marked nucleophilic nature due to the presence of basic amine surface functionalities and hydrogen bonding motifs. This property enhances their capacity for the adsorption of heavy metals, such as Fe^{2+}, Fe^{3+}, Hg^{2+}, Pd cluster, and so on [180–183]. Experimental and theoretical efforts were provided in order to investigate the potential of g-C_3N_4 QDs usage in heavy metal adsorption. In this context, Shorie et al. led the experimental work in 2019 in which they conducted a laboratory-scale investigation wherein they synthesized a composite material consisting of agarose-loaded g-C_3N_4 QDs through the use of microwave-assisted thermal methodology [180]. The purpose of this composite was to remove Hg^{2+} from wastewater. Initially, the agarose-loaded g-C_3N_4 QDs composite was loaded into a micro-cartridge and subsequently utilized for the adsorption of Hg^{2+} (ranging from 0.22 to 2715 mg/L) contaminated wastewater. This was achieved by passing 1 mL of the solution through the column. The Hg^{2+} removal efficiency was found to be 96.5%, following a treatment with 2715 mg/L of Hg^{2+}-spiked sewage water, despite the highly complex matrix. Furthermore, an assessment was conducted on the toxicity of the composite material comprising of agarose-loaded g-C_3N_4 QDs towards Escherichia coli and Staphylococcus aureus bacterial strains. The bacterial cultures were inoculated onto an agar medium and subjected to varying concentrations of agarose-loaded g-C_3N_4 QDs (ranging from 0.1 to 10 mg/L) for 12 h at a temperature of 37 °C. The results indicated that the composite did not exhibit any negative impact on the bacterial growth in either of the culture media. This suggests that the absence of heavy metals in the structure of the composite may have contributed to its non-toxicity toward micro-organisms. DFT calculations unveiled a plausible interaction between the mercury atoms and g-C_3N_4 QDs (**Fig. 14a** and **14b**). Furthermore, the incorporation of a mercury atom in the synthesized g-C_3N_4 QDs surface resulted in a moderate degree of structural distortion, i.e., moderate changes in the overall geometry of g-C_3N_4, a reduction in band gap, and a modified dielectric response.

Theoretical studies have focused on the adsorption of metals onto the surface of g-C_3N_4 QDs. For example, Ghashghaee et al. [183] conducted an investigation into the potential of Fe^{2+} and Fe^{3+}

adsorption by four models of pristine heptazine and triazine polymeric g-C_3N_4 QDs in flat and corrugated configurations, labeled as hg-CNQD1 and hg-CNQD2, tg-CNQD1 and tg-CNQD2, respectively, in which 1 and 2 refer to the flat and corrugated configurations (**Fig. 14c**). The optimal adsorption occurred on hollow sites, which exhibited diverse coordination numbers and geometrical configurations. Amidst a plethora of potential locations, it was observed that two vacant sites facilitated the stabilization of the Fe species with negligible energy expenditure. Specifically, the heptazine and triazine type structures yielded three- and six-fold coordination complexes, respectively. The results of the optimization process revealed that the bond lengths between Fe and N atoms in the carbon nitride structures of heptazine type were relatively short. Additionally, both Fe cations were observed to be stabilized in close proximity to the ring plane. g-C_3N_4 QDs exhibited a remarkable ability to recognize iron cations, particularly Fe^{3+}, as evidenced by a substantial decrease in the energy gap. The Fe analytes were found to contribute to the conduction band minimum of the sensor, as opposed to its valence band maximum. The study investigated the impact of surface corrugation on the binding of analytes to the heptazine-type sensor surface, with a focus on the associated electronic states.

In similar fashion, Hosseini and coworkers [182] employed DFT to examine the adsorption of Pd_n clusters of varying sizes (n = 2-8) on g-C_3N_4 QDs. Clusters of Pd_2, Pd_4, and Pd_6 exhibited a proclivity for locating themselves at a corner of the six-fold cavity of g-C_3N_4. Conversely, the Pd_8 cluster was situated atop the cavity of g-C_3N_4 to enable optimal interaction with all pyridine-like nitrogen atoms of the cavity in a simultaneous manner, thereby enhancing efficiency. The Pd_n cluster in Pd_n/g-C_3N_4 complexes (where n ranges from 2 to 6) exhibited a positive charge, indicating a transfer of charge from the metal cluster to g-C_3N_4. Conversely, the net charge of Pd_8 in Pd_8/g-C_3N_4 was negative, indicating a reverse direction of charge transfer in this particular complex. Furthermore, it was observed that the augmentation of Pd_n cluster dimensions results in a reduction of the energy band gap of the Pd_n/g-C_3N_4 composite in comparison to the unmodified g-C_3N_4. Time-dependent DFT (TD-DFT) was implemented to compute the absorption spectra of both the unadorned g-C_3N_4 QDs and Pd_n/g-C_3N_4 complexes. The study revealed that the introduction of Pd_n clusters onto g-C_3N_4 resulted in a notable redshift of the absorption peaks of g-C_3N_4 toward lower wavelengths. Furthermore, the augmentation of the absorption bands within the 400 to 800 nm range was observed to be contingent on the size of the Pd_n cluster. This phenomenon may contribute to the heightened photo-catalytic efficacy of Pd_n/g-C_3N_4 complexes in the visible light region when compared to unmodified g-C_3N_4. The majority of UV-Vis absorption bands observed for the Pd_n/g-C_3N_4 complexes within the 400-800 nm range can be attributed to the excitation of electrons from the Pd_n cluster to g-C_3N_4. This phenomenon results in a reduction of electron-hole recombination within the complexes, as compared to the bare g-C_3N_4. The amalgamation of g-C_3N_4 states with Pd_n clusters results in a reduction in the absorption band intensity of g-C_3N_4 within the 200-300 nm region.

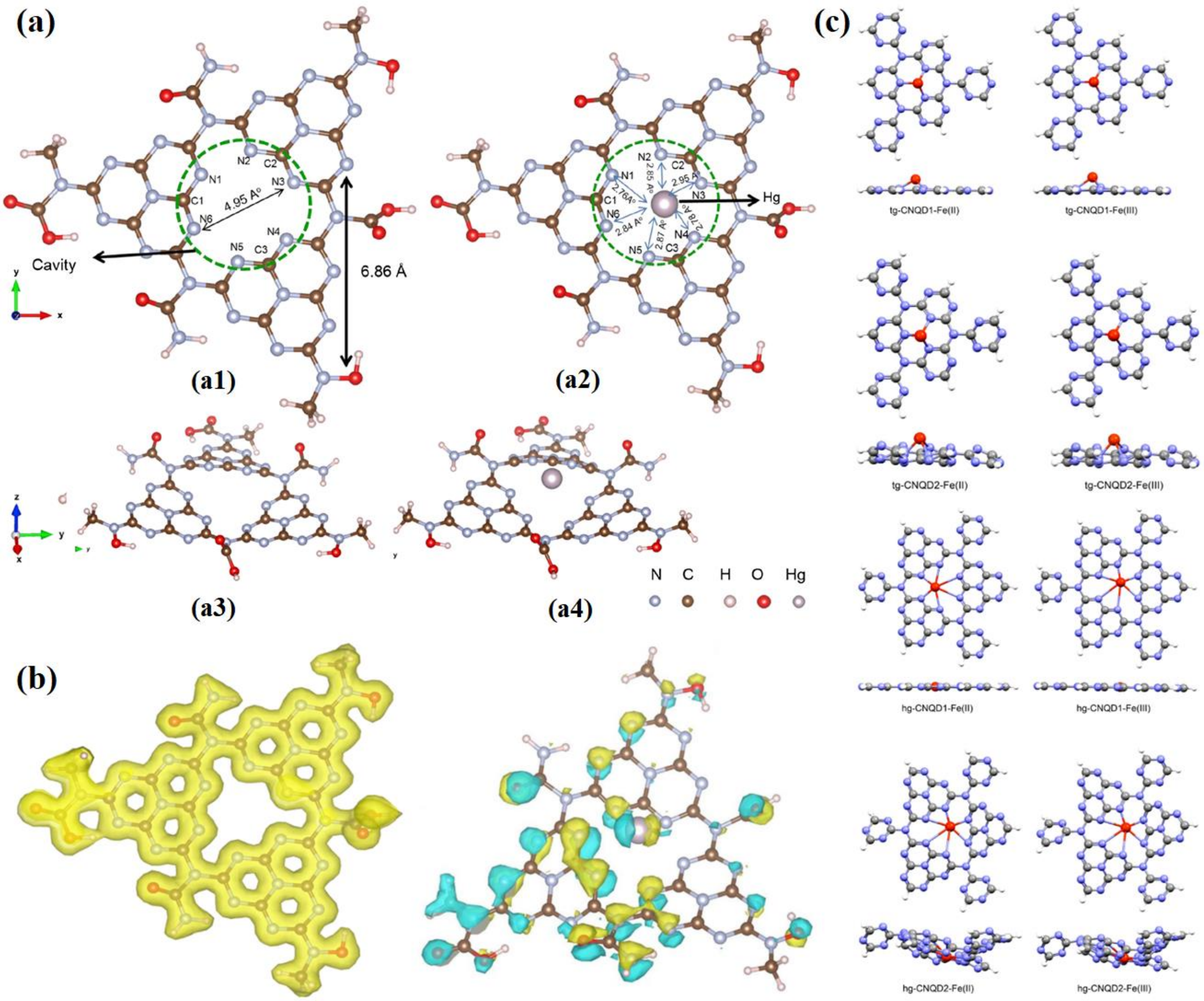

Fig. 14. (a) Enhanced constructions of the electron-rich cavity in which Hg atoms get trapped is seen in the circled region of (a1) the top view of the uncovered sheet of g-C_3N_4, and (a2) the top view of the g-C_3N_4-Hg geometric structure. (a3) g-C_3N_4 sheet, seen from the side, (a4) A section through the geometry of g-C_3N_4-Hg from the side. (b) A graphical representation of the charge density in a g-C_3N_4 sheet (left). The charge density, indicated by the yellow hue, is shown on the surface of the g-C_3N_4-Hg structure at an isovalue of 0.02 e/$Å^3$ (right). The positive (charge buildup) and negative (charge depletion) areas are represented by the yellow and blue hues, respectively. Reproduced

with permission from [180]. (c) Both the top and bottom panels show optimized geometries of the Fe/g-CNQD complexes at the HSE06/6-311 + G* level of theory. Nitrogen atoms are represented by blue balls, and carbon atoms by grey ones. Reproduced with permission from [183].

4.3. Sensing

g-C_3N_4 QDs were used as a promising material for developing sensors to detect various analytes in both aqueous medium for environmental purposes and microbiological environment e.g. body fluids including heavy metal ions (Cu^{2+}, Hg^{2+}, Fe^{3+}) [87,103–105,108,110,125,127,138][184–186], biothiols [52,187], glucose [188–190], ascorbic acid [191,192], enzyme [186,193,194], and other molecules based on their interesting properties such as high electron transfer characteristics, stability, excellent fluorescence quenching abilities, light and electricity conversion capability, biocompatibility, etc. In the past several years, researchers have made significant strides in developing new g-C_3N_4 QDs based sensors for physical, chemical, and bio-analysis. Thus far, these sensors based on g-C_3N_4 QDs may be broken down into two distinct categories: Environmental sensing and Biosensing. The sections that follow provide a concise summary of current developments in these cutting-edge sensing applications.

4.3.1. Environmental sensing

In recent years, significant advancements have been made in the development of innovative sensors utilizing g-C_3N_4 QDs for a range of environmental applications, especially to detect heavy metal ions in aqueous media. Similar to carbon-based QDs and organic polymers [161,162], sensors utilizing g-C_3N_4 QDs have been categorized into three distinct groups, mainly PL, CL, and photoelectrochemical sensors. g-C_3N_4 QDs can exhibit varying PL quantum yields (PLQYs) and emit diverse colors when synthesized using different strategies. The emission of in g-C_3N_4 QDs is believed to originate from both surface defects and intrinsic energy states of these nanomaterials. Furthermore, this emission is notably responsive to interactions with other species (molecules or metal ions), as well as immediate changes in the surrounding environment. Hence, the PL characteristics exhibited by g-C_3N_4 QDs can be effectively utilized in a wide range of sensing applications. To date, only a limited number of methodologies utilizing fluorescence resonance energy transfer, photon-induced electron transfer, and PL quenching of g-C_3N_4 QDs have been proposed for the purpose of constructing PL sensors. For instance, Barman and Sadhukhan [104] first reported the use of g-C_3N_4 QDs as sensors for Hg^{2+} and I^- ions. They described that the g-C_3N_4 QDs exhibiting a strong blue fluorescence were successfully produced through a straightforward microwave-mediated approach utilizing formamide as the precursor. The fluorescence emission characteristics of g-C_3N_4 QDs exhibited a significant reliance on the solvent, pH, and excitation wavelengths. Furthermore, the emission lifetime showed a decreasing trend as the polarity of the solvent increased. The fluorescence of these QDs is significantly quenched, resulting in high sensitivity and selectivity as florescent probes for mercuric ions in aqueous media with a detection limit of approximetly10^{-9} M. The authors stated that the quenching of fluorescence is attributed to the complex formation between Hg^{2+} ions and the CNx sheet, which involves the p delocalized electron moieties of the latter. The introduction of iodide ions resulted in the detachment of Hg^{2+} and the formation of HgI_2, thereby restoring the distinct fluorescence properties of g-C_3N_4 QDs. The g-CNQDs exhibited dual functionality in detecting mercuric and iodide ions in aqueous media with high selectivity and sensitivity through a fluorescence response mechanism characterized by an “ON-OFF-ON” pattern.

In another study, Lu et al. [138] synthesized QDs of g-C_3N_4 co-doped with oxygen and sulfur through thermal treatment of thiourea and citric acid. The reported co-doped g-C_3N_4 QDs exhibited a robust blue photoluminescence and possessed a comparatively elevated quantum yield of 14.5%. The fluorescence reactions of the reported co-doped g-C_3N_4 QDs showed variability in the presence of distinct metal ions, despite being subjected to identical conditions (**Fig 15a**). Remarkably, the photoluminescence intensity of oxygen and sulfur co-doped g-C_3N_4 QDs can be significantly suppressed in the presence of mercury ions. The utilization of co-doped g-C_3N_4 QDs resulted in an effective detection of Hg^{2+} in the presence of other metal ions at a concentration of 200 mM (**Fig. 15b**). The remarkable selectivity and specificity exhibited by co-doped g-C_3N_4 QDs can be attributed to the heightened affinity of Hg^{2+} toward the amino and thiourea groups present on their surface, in comparison to other metal ions. The authors observed that the co-doped g-C_3N_4 QDs demonstrated consistent and distinct PL intensities that were dependent on the concentration of mercury(II) ions within a concentration range of 0.001-20 mM. The detection limit for this phenomenon was determined to be 0.37 nM (3S/N). The authors also investigated the use of the produced co-doped g-C_3N_4 QDs as a viable option for cellular imaging, demonstrating favorable biocompatibility. As such, they have the potential to serve as a fluorescent probe in various biosensing and bioimaging applications.

With the same mind set, Rong and colleagues [186] used the co-doping approach to yield phosphorus and oxygen-doped g-C_3N_4 nanodots from melamine and phytic acid precursors for label-free detection of Cu^{2+} and acetylcholinesterase activity. P,O-g-C_3N_4 nanodots exhibited a robust blue fluorescence, characterized by a noteworthy quantum yield of 90.2%. Additionally, they demonstrated remarkable resilience against photobleaching and possessed high ionic strength. Similar to the aforementioned studies, the proposed approach in this work was based on fluorescence quenching, which involved static fluorescence quenching and photoinduced electron transfer. Under ideal circumstances, the detection of Cu^{2+} can be expeditiously accomplished within 5 min timeframe, with a detection threshold of 2 nanomolar and a linear range spanning from 0 to 1 millimolar. The fluorescence of the P,O-g-C_3N_4 nanodots–Cu^{2+} system can be activated in the presence of acetylcholinesterase (AChE) by utilizing acetylthiocholine (ATCh) as the substrate. This activation is achieved through the reaction between Cu^{2+} and thiocholine, which is the hydrolysis product of ATCh by AChE. The system exhibits high sensitivity. A linear range spanning from 0.01 to 3 mU/mL was achieved, with a corresponding detection limit of 0.01 mU/mL. Based o the reported findings, the P,O-g-C_3N_4 nanodots exhibited a robust fluorescence emission, which was effectively suppressed by Cu^{2+} due to its chelation with N in the P,O-g-C_3N_4 nanodots through static fluorescence quenching and PET from the P,O-g-C_3N_4 nanodots to Cu^{2+}. Subsequently, the luminescence of P,O-g-C_3N_4 nanodots-Cu^{2+} composite was observed to exhibit significant activation upon exposure to AChE and ATCh, owing to the interactions between Cu^{2+} and TCh, which is the byproduct of ATCh hydrolysis catalyzed by AChE (**Fig 15c**).

Similarly, Liu and coworkers [87] targeted Cu^{2+} as an analyte to be detected using a g-C_3N_4 QD based sensor. A facile and rapid method was employed to synthesize highly fluorescent QDs through the process of recrystallization and ultrasonic exfoliation. g-C_3N_4 QDs with controllable sizes were synthesized using recrystallized dicyandiamide as the precursor. The synthesis process only required 90 min, and the sizes of the QDs were modulated from 5 to 200 nm by manipulating the ultrasonic time. In addition, enhanced fluorescent efficiency was achieved in comparison to conventional g-C_3N_4 QDs. The synthesized g-C_3N_4 QDs exhibited a response to Cu(II) within a concentration range of 0.5 to 30 mmol/L and possessed a detection limit of 0.3 nmol/L. The technique was utilized for the quantification of copper (II) in various water samples of environmental origin. In another work, Wang et al. [185] reported the synthesis of QDs of oxygen and sulfur co-doped g-C_3N_4 (OS-g-C_3N_4-dots) with a high fluorescence quantum yield (FLQY) of 33.9%. The synthesis was achieved through a simple electrochemical “tailoring” process. OS-g-C_3N_4-dots exhibited a selective affinity toward copper and silver ions, leading to a significant quenching of the fluorescence emission. OS-g-C_3N_4-dots were further capable of selectively detecting Cu^{2+} and Ag^{+} with the aid of diverse masking agents. In addition, the synthesized OS-g-C_3N_4-dots/Ag^{+} exhibited a fluorescent response that was specific to biothiols (HCy, Cys, and GSH), which can be described as a "turn-on" response. Consequently, diverse sensing platforms with multiple functionalities were developed utilizing the fluorescence response of OS-g-C_3N_4-dots based on the "ON-OFF-ON" mechanism to detect Cu^{2+}, Ag^{+}, and biothiols (**Fig. 15d**). Under ideal circumstances, the minimum detectable concentrations of Cu^{2+}, Ag^{+}, HCy, Cys, and GSH were found to be 7.0×10^{-10} M, 2.0×10^{-9} M, 1.0×10^{-8} M, 1.0×10^{-8} M, and 8.4×10^{-9} M, respectively. In addition, the platforms that were prepared demonstrated successful application in detecting Cu^{2+}, Ag^{+}, and biothiols in real-world samples. Moreover, they displayed exceptional sensitivity and selectivity.

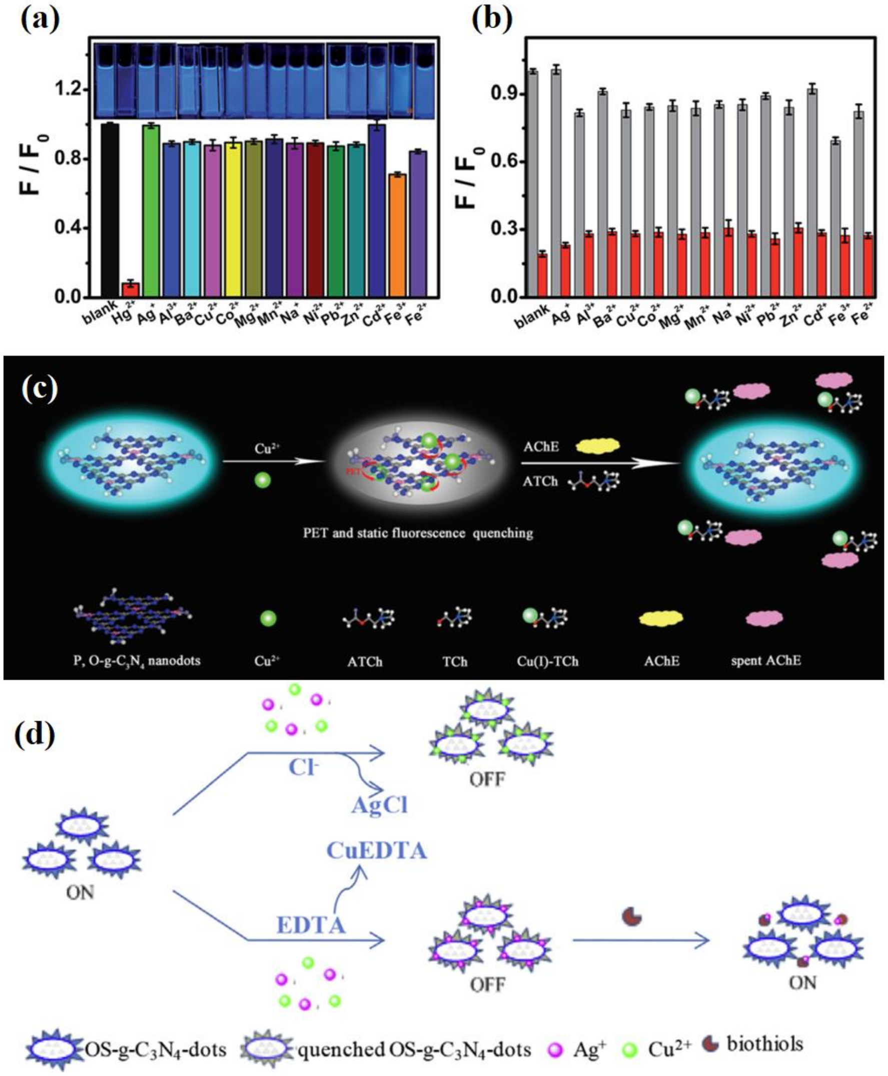

Fig. 15. (a) The fluorescence reactions of O and S co-doped g-C_3N_4 QDs were observed in the presence of various metal ions, with an excitation wavelength of 369 nm and a concentration of 50.0 mM for the metal ions. The

photographs are arranged in accordance with the spectra, as depicted in the inset. (b) The fluorescence intensities (F/F_0) of O and S co-doped g-C_3N_4 QDs were measured in the presence of metal ions (200.0 mM). The mixture solution was subsequently treated with 50.0 mM Hg^{2+} and the resulting fluorescence intensities were recorded and presented in the red column. Reproduced with permission from [138]. (c) illustrative representation of the sensitive and selective fluorescence detection of Cu^{2+} and AChE activity using P,O-g-C_3N_4 nanodots based sensor. Reproduced with permission from [186]. (d) Schematic depiction of the detection of Cu^{2+} and Ag^{+} using the fluorescence "ON-OFF" assay of OS-g-C_3N_4-dots and the detection of biothiols using the fluorescence "OFF-ON" assay of OS-g-C_3N_4-dots/Ag^{+}. EDTA and Cl^{-} serve as Cu^{2+} and Ag^{+} concealing agents, respectively. Reproduced with permission from [185].

Besides Cu(II) ions, researchers have also explored the use of g-C_3N_4 QDs to detect Hg(II) and Fe(III) cations for environmental purposes. For example, Cao et al. [105] published a study where a microwave-assisted solvothermal technique was employed to synthesize g-C_3N_4 QDs that exhibit fluorescence. Oleic acid was utilized as the reaction medium, and the reaction was conducted at a moderate temperature for a brief duration of 5 min. The precursors employed in the study were citric acid monohydrate and urea. g-C_3N_4 QDs demonstrated an atypical fluorescence that was dependent on the excitation wavelength, characterized by two emission peaks at 450 and 540 nm. The utilization of g-C_3N_4 QDs exhibiting a quantum yield of 27.1% has the potential to function as a proficient fluorescent sensing mechanism for the detection of Hg^{2+} ions in tap water samples without the need for labeling, thereby enabling sensitive detection with a limit of 0.14 μM. In similar fashion, Achadu et al. [127] utilized a microwave-assisted hydrothermal technique to synthesize g-C_3N_4 QDs that were modified with thymine (T-gCNQDs). The T-gCNQDs were found to exhibit unique fluorescent properties and were identified as a promising nanoprobe for the detection of Hg(II). The specimens demonstrated exceptional optical characteristics, specifically a blue emission that boasted a fluorescence quantum yield of 46%, coupled with the ability to dissolve in water. This research indicates that fluorescence, which is most accurately assessed at excitation/emission wavelengths of 350/445 nm, experiences a significantly greater level of quenching by Hg(II) in comparison to the thymine-free nanoprobe. The selective nature of quenching is observed to be significant even when other metal ions are present. The aforementioned phenomenon can be attributed to the creation of complexes based on T-Hg(II)-T. The concentration range of Hg(II) within 1.0 to 500 nM exhibits a linear decrease in fluorescence with a detection limit of 0.15 nM. This technique was employed for the quantification of Hg(II) in artificially contaminated specimens of tap and pond water. The practical applicability of the assay was demonstrated by the recovery rate exceeding 95%.

In another study, Patir and Gogoi [125] used the bottom-up doping strategy to yield S and O containing g-C_3N_4 QDs derived from thiourea and ethylenediaminetetraacetic acid disodium salt, labeled as SCNQDs. The sensing capability of SCNQDs toward Hg^{2+} has been exhibited both in solution and solid phase, specifically when SCNQDs are loaded onto filter paper. The SCNQDs exhibit equivalent Hg^{2+} sensing proficiency in both double-distilled and tap water solutions, thereby rendering the technique pragmatically feasible for real-world scenarios. A linear correlation exists between the sensitivity of SCNQDs and Hg^{2+} within the range of 10 to 1 μM (**Figs. 16a-d**). The study also reveals a minimum detection limit of 0.01 nM, indicating a significant improvement compared to prior findings. Likewise, the SCNQDs that were applied onto filter paper exhibited comparable sensing ability toward Hg^{2+} spiked tap and double-distilled water solutions (**Figs. 16e-g**). A system for the detection of Hg^{2+} was developed using filter paper loaded with SCNQDs. In addition, a composite of SCNQDs and poly(vinyl alcohol) (PVA) was synthesized to investigate the phenomenon of room-temperature phosphorescence in SCNQDs.

With respect to Fe ion sensing, Li and colleagues [184] reported the use of chemical oxidation and liquid exfoliation to convert bulk g-C_3N_4 into g-C_3N_4 QDs. The resulting g-C_3N_4 QDs exhibited a size distribution, spanning from 1 to 5 nm with a mean diameter of 3 nm. This study revealed that the adsorption of Fe(III) ions onto the g-C_3N_4 QD surface occurs through electrostatic interactions. Additionally, the Fe(III) ions cause a reduction in the blue fluorescence of the g-C_3N_4 QDs through an inner filter effect. The utilization of g-CNQDs as a fluorescent probe enables the determination of Fe(III) in spiked natural water samples with high selectivity over other ions. This process can be completed within a minute at excitation/emission wavelengths of 241/368 nm. The response exhibited linearity within the Fe(III) concentration range of 0.2-60 μmol L^{-1} with a detection limit of 23 nmol L^{-1}.

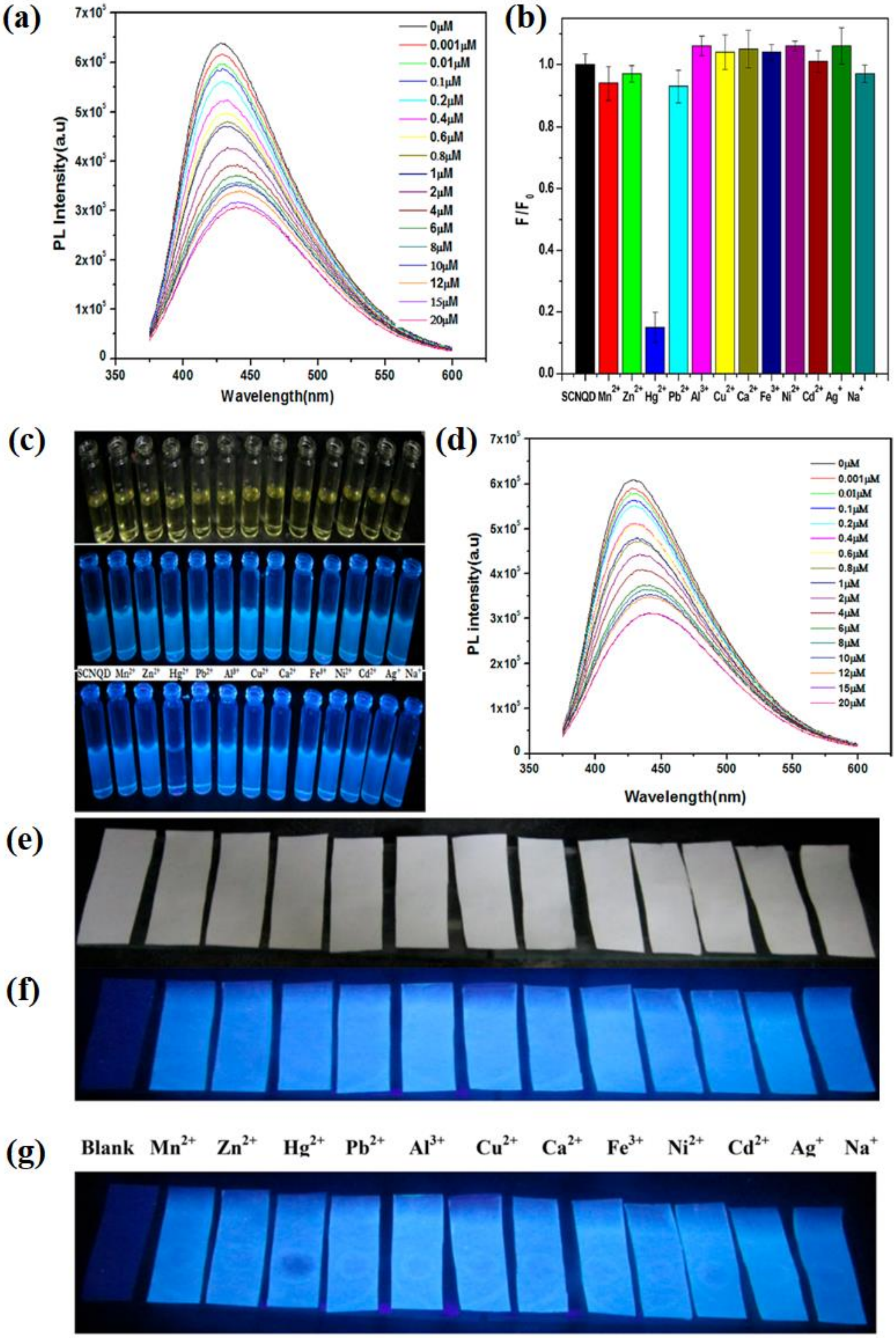

Fig. 16. (a) Reactions of photoluminescence (PL) from SCNQDs in double-distilled water to varying concentrations of Hg^{2+} at excitation wavelength of 360 nm. (b) Bar diagram that illustrates the impact of SCNQDs on PL upon the addition of various metal ions, with a fixed concentration of 10 μM and an excitation wavelength of 360 nm. (c) Digital images of SCNQDs in aqueous solutions exposed to white light (upper panel), 365 nm light (middle panel), and in the presence of different metal ions (10 μM M) exposed to 365 nm light (bottom panel). (d) responses of PL from SCNQDs

aqueous medium on addition of different amounts of Hg^{2+} in tap water with an excitation wavelength of 360 nm. Digital photos of SCNQDs incorporated into filter paper (a) under white light, (b) under 365 nm UV light, and (c) on drop casting of 2 μL of 10μM metal ion solutions ($Mn^{2+,}$ $Zn^{2+,}$ $Hg^{2+,}$ $Pb^{2+,}$ $Al^{3+,}$ $Cu^{2+,}$ $Ca^{2+,}$ $Fe^{3+,}$ Ni^{2+}, Cd^{2+}, Ag^{+}, and Na^{+}). Reproduced with permission from [125].

Jumping to the chemiluminescence (CL) based sensors, it is acknowledged in the literature that CL refers to the emission of light resulting from the relaxation of an electronically excited intermediate or product state to the ground state. This excited state is generated by a chemical reaction between the reagents. The CL technique finds utility in the field of analytical chemistry, owing to its remarkable sensitivity and uncomplicated instrumentation. Luminol, potassium permanganate, lucigenin, and peroxalate are commonly employed and investigated CL reagents in the field of analytical chemistry owing to their satisfactory CL luminosity. Nevertheless, the reagents utilized are costly and toxic, and exhibit exceptional selectivity. Hence, it is imperative to create additional CL systems that possess robust emission intensity and eco-friendly methodologies. g-C_3N_4 QDs have the potential to augment the CL effect through multiple pathways, mainly they have the ability to function as catalysts in chemical reactions, as well as to concentrate the excited CL emitter and amplify its emission. g-C_3N_4 QDs have the ability to participate in the CL reaction, resulting in the emission of CL due to the recombination of the hole-injected and electron-injected g-C_3N_4 QDs. With this background, Tang et al. [103] applied, for the first-time, g-C_3N_4 QDs as CL systems for the selective detection of free chlorine in water. They reported a one-step, microwave-assisted method for synthesizing strong fluorescent g-C_3N_4 QDs by utilizing guanidine hydrochloride and EDTA as precursors. The injection of NaClO into the prepared g-C_3N_4 QDs resulted in a robust CL emission and led to the establishment of a novel CL system for the direct detection of free chlorine. The detection of free residual chlorine in water was carried out with high sensitivity, yielding a detection limit of 0.01 μM. Additionally, the detection range was found to be quite broad, spanning from 0.02 to 10 μM. A proposed mechanism for CL was derived from the analysis of CL spectral, UV-visible absorption spectral, and electron spin resonance (ESR) spectral studies. The emission of CL was attributed to the radiative recombination of holes and electrons injected by the oxidant in the g-C_3N_4 QDs. The surface of g-C_3N_4 QDs was found to exhibit $^1O_2$ generation through ROS in the g-C_3N_4 QDs-NaClO system. This energy transfer from $^1O_2$ to g-C_3N_4 QDs resulted in a significant increase in the CL emission (**Figs. 17a** and **17b**).

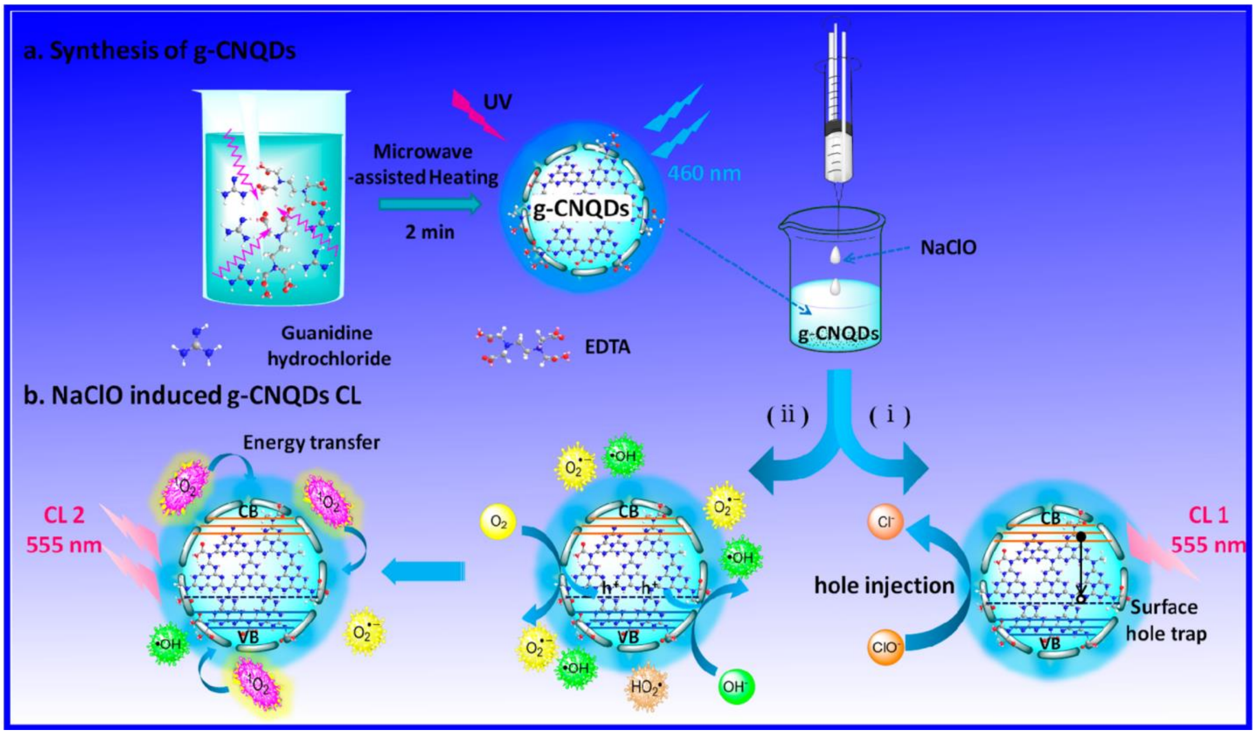

Fig. 17. (a) illustrative representation for g-C_3N_4 QDs synthesis using MW assisted route. (b) Proposed CL mechanism of g-C_3N_4 QDs-NaClO system. Reproduced with permission from [103]

Following that state of mind, Abdolmohammad-Zadeh and Rahimpour [108] reported a similar study that involved the synthesis of g-C_3N_4 QDs through the microwave-assisted method. They investigated the CL emission of the synthesized g-C_3N_4 QDs under the influence of $K_3Fe(CN)_6$ as an oxidant, along with an in-depth analysis of the underlying CL mechanism. A chemosensor with high sensitivity was developed for the detection of Hg(II) ions in aqueous solutions, utilizing the g-C_3N_4 QDs- $K_3Fe(CN)_6$ CL system and taking into account the diminishing effect of Hg(II) ions. The study employed a response surface methodology to optimize the experimental parameters that impact the analytical signal. The calibration graph exhibited linearity within the range of 0.25-10 ng mL^{-1} under the optimized experimental conditions, and the detection limit was determined to be 0.08 ng mL^{-1}. This study reported the inter-day and intra-day relative standard deviations for six replicate measurements of 4 ng mL^{-1} Hg(II) ion as 3.4% and 2.8%, respectively. The reported method was effectively utilized to discern Hg(II) in both water and food samples with a high degree of selectivity and sensitivity. The samples that were Hg(II)-spiked exhibited recoveries within the range of 95.7 to 102.8%. The precision of the method was assessed through the examination of a certified reference material (SRM 1566b).

Concerning the photoelectrochemical (PEC) based g-C_3N_4 QDs sensors, it is basically using the principals of PEC sensing, which mainly involves the amplification of photocurrent resulting from the consumption of photogenerated holes at the anode or photogenerated electrons at the cathode as a consequence of the interactions between the analyte and photoresponsive material. Following this principle, Chen et al. [110] examined the production of nanohybrids through an *in situ* coupling of g-C_3N_4 QDs and Bi_2MoO_6 nanoparticles. The photocurrent intensity of the prepared nanohybrids was observed to be nearly three and six times higher than those of neat g-C_3N_4 QDs and Bi_2MoO_6 NPs, respectively. The observed enhancement was ascribed to the expedited charge transfer from the CB of g-C_3N_4 QDs to that of Bi_2MoO_6. The nanohybrids were effectively utilized in the development of a Cu^{2+} PEC sensor, owing to their exceptional PEC capabilities. The developed sensor exhibited favorable performance characteristics within the ideal conditions, demonstrating a broad linear range spanning from 3 nM to 40 μM. The observed high selectivity of g-C_3N_4 QDs/Bi_2MoO_6 nanohybrids suggests their potential to be used as a photoactive material for PEC sensing.

4.3.2. Biosensing

The occurrence of pathological processes in tissues and organs are frequently triggered by alterations in the biological microenvironment, including but not limited to variations in temperature, pH, redox state, ion concentration, and biomolecules. Hence, the utilization of g-C_3N_4 QDs as signal monitoring detectors facilitates the explication of intricate biological mechanisms and advancement of sophisticated diagnostic techniques [195,196]. g-C_3N_4 QDs exhibit semiconductor-like characteristics, rendering them highly effective as optical probes for detecting alterations in the adjacent biological microenvironment. This is attributed to the presence of nitride-N-atom in the graphitic structure, which introduces a distinct type of "surface state". In recent times, a diverse range of sensors have been fabricated utilizing the adjustable PL and electrochemiluminescence (ECL) properties of g-C_3N_4 QDs. This section will be mainly divided into three major parts including enzyme sensing, intracellular redox state sensing, molecules sensing (e.g. glucose, ascorbic acid, amikacin, heparin, dopamine, and others).

4.3.2.1. Enzyme sensing

Maintaining physiological homeostasis requires the attainment of optimal levels of enzyme activity. Numerous pharmacological agents exhibit the ability to activate or inhibit enzymes. Hence, the determination of enzyme concentration holds immense importance in the realm of health surveillance and pathological identification [197]. Acetylcholinesterase (AChE) is a serine esterase that is present in both the central and peripheral nervous systems and was the main analyte in Chen et al. work [186] . They reported a specific type of AChE sensor that utilizes phosphorus and oxygen-doped g-C_3N_4 QDs (P/O-g-C_3N_4 QDs). The introduction of Cu^{2+} into the solution of P/O-g-C_3N_4 QDs resulted in fluorescence quenching, which can be attributed to static fluorescence quenching and photoinduced electron transfer. Upon the introduction of acetylthiocholine (ATCh), the P/O-g-C_3N_4 QDs-Cu^{2+} system exhibited a notable increase in fluorescence, indicating a high level of sensitivity. A linear range spanning from 0.01 to 3 mU mL^{-1} with a detection limit of 0.01 mU mL^{-1} was achieved.

Riboflavin (RF) serves as a complementary enzyme and is essential for preserving the typical structure and operation of the human organism [198,199]. Lu et al. [193] developed an electrochemical sensor utilizing g-C_3N_4 QDs for the purpose of detecting RF levels in the presence of co-reactant $K_2S_2O_8$. Based on their findings, g-C_3N_4 QDs have the potential to be used for electrochemical sensing applications. The study further revealed that the ECL signal of g-C_3N_4 QDs, characterized by a size distribution of 3.5 nm, was effectively suppressed through the process of resonance energy transfer (RET) between the donor g-C_3N_4 QDs and the receptor RF. These ECL findings indicated that the RF amount present in vitamin B_2 (VB_2) tablets was in agreement with the fluorescence analysis. Furthermore, the ECL method exhibited a broader linear range of 0.02-11 mM and a lower minimum detection limit of 0.63 nM (S/N=3) compared to fluorescence analysis.

In another work, Zou et al. [194] developed a highly sensitive method for detecting trypsin inhibitor (TI) using a ratiometric fluorescence nanosensor. This nanosensor was composed of gold nanoclusters and g-C_3N_4 QD nanocomposites that were protected by bovine serum albumin (BSAAuNC@g-CNQDs). The hydrolysis of BSA can be catalyzed by trypsin, which can subsequently lead to the decomposition of BSA-AuNC@g-CNQDs (**Fig. 18**). This process ultimately results in the quenching of fluorescence in the nanocomposites. The addition of TI resulted in the inhibition of trypsin-mediated decomposition of the BSA-AuNC-g-CNQDs system, thereby providing protection against fluorescence quenching of the nanocomposites. The nanocomposites-trypsin sensor system exhibited a high degree of sensitivity in detecting TI, as evidenced by its limit of detection of 0.089 ng/mL.

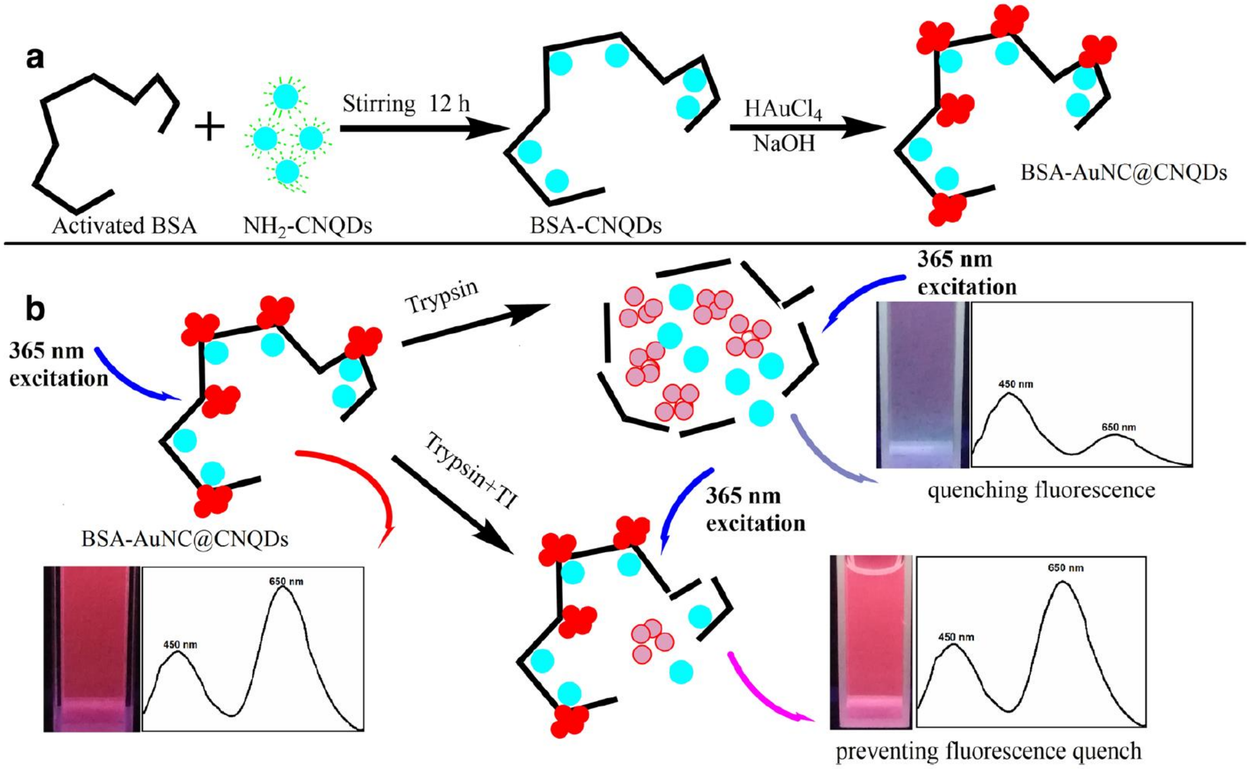

Fig. 18. (a) illustrative representation of BSA-AuNC@g-CNQDs synthesis. (b) Trypsin mechanism of detection. Reproduced with permission from [194].

4.3.2.2. Intracellular redox state sensing

The regulation of cellular, microenvironmental, and chemical processes has been extensively investigated with regards to the intracellular redox state environment of the cell as viewed through the redox state of the glutathione disulfide/glutathione couple [200]. The alteration of the intracellular redox state has significant implications not only on the transfer of signals, protein production, DNA and RNA formation, and enzyme triggering, but also on the stability of the cell cycles [201]. The intracellular redox state is predominantly influenced by the concentration of glutathione (GSH), which is regarded as a crucial molecular determinant [202]. The investigation of the intracellular redox state has been widely facilitated through the utilization of GSH level detection. Several examples of utilizing g-C_3N_4 QD-based sensors for the detection of GSH levels are available in literature. For example, Lu et al. [187] utilized g-C_3N_4 QDs to measure the concentration of biothiols by monitoring the shift in plasmon resonance absorption peak of Ag nanoparticles (NPs), which was caused by the reduction of Ag^+ in the g-CNQD solution. The biothiols have the ability to form a complex with the Ag^+ ions, resulting in the consumption of Ag^+ ions and acting as a capping agent to inhibit the growth of Ag NPs. This phenomenon leads to a reduction in the absorption peak of the Ag NPs in the presence of the g-C_3N_4 QD solution. The dispersion of Ag^+ in the g-C_3N_4 QD solution has been found to demonstrate a notable degree of selectivity and sensitivity toward biothiols such as cysteine (Cys), homocysteine (Hcy), and GSH. The detection limit for these biothiols was observed to be low with values of 11.5, 16.1, and 15.5 nM, respectively.

Wang et al. [185] conducted a study on the O/S doped g-C_3N_4 QDs, which revealed a state of fluorescence “turn-off” in the presence of Ag^+. The doped QDs exhibited a distinctive fluorescent response to biothiols (HCy, Cys, and GSH) upon activation, thanks to the higher affinity of biothiols-Ag^+ compared to pyridinic N-Ag^+. This led to the fluorescence recovery of the O/S doped g-C_3N_4 QDs. The prepared sample exhibited detection limits of 10, 10, and 8.4 nM for HCy, Cys, and GSH, respectively, under the optimal conditions. Interestingly, the sensor based on the O/S doped g-C_3N_4 QDs demonstrated remarkable sensitivity and selectivity in detecting GSH in real-world samples. Xu et al. [52] developed a “switch-on” fluorescent sensor, enabling the swift and precise identification of GSH in food specimens. This sensor was based on the g-C_3N_4 QDs-Hg^{2+} system. The electron transfer occurring in the g-C_3N_4 QDs-Hg^{2+} complex was found to be responsible for the quenching of fluorescence and subsequent switching to the “off” state. The introduction of GSH resulted in the activation of fluorescence in g-C_3N_4 QDs, thanks to the superior binding affinity of GSH toward the Hg^{2+} ions, which facilitated their capture.

4.3.2.3. Molecules sensing

Ascorbic acid (AA) is a vital biomolecule in biological systems and is administered to individuals who exhibit inadequate dietary intake of vitamins for the prevention or treatment of AA deficiency. Insufficient amounts of AA may lead to the development of scurvy, a condition characterized by symptoms such as skin lesions, muscle fatigue, arthralgia, fatigue, and dental complications. Thus, AA exerts a significant impact on various physiological processes and pathologies in the human body [203]. Currently, there is significant interest among researchers in accurately detecting the AA levels. For example, Achadu et al. [191] synthesized a special type of g-C_3N_4 QDs through a hydrothermal process at 200 °C for 6 h, utilizing nitrogen-rich diaminomaleonitril (DAMN) as precursor. The covalent linkage between the g-C_3N_4 QDs and 4-amino-2,2,6,6-tetramethyl(piperidin-1-yl)oxyl (4-AT) was established through an amide bond, resulting in the formation of the g-C_3N_4 QDs-4-AT complex. The introduction of g-C_3N_4 QDs-4-AT resulted in the attenuation of the luminescence exhibited by g-C_3N_4 QDs. The fluorescence intensity of g-C_3N_4 QDs exhibited a gradual recovery in direct correlation with the concentration of AA in its presence. The findings of the authors indicated that g-C_3N_4 QDs-4-AT exhibits a linear response to AA within a concentration range of 1-10 nM with a detection limit of 1.25 nM. The same group also presented a study on the synthesis of a sensor utilizing a modified form of tannic acid (TA) and g-C_3N_4 QDs, referred to as TA-g-C_3N_4 QDs. The study revealed that the fluorescence emanating from TA- g-C_3N_4 QDs could be suppressed by the presence of $Cu2^+$ ions, even at low concentrations [192]. This phenomenon was attributed to a charger/electron transfer mechanism that occurs between Cu^{2+} ions and hydroxyl groups present in TA. Upon the introduction of AA into the aforementioned solution, the fluorescence of TA-g-C_3N_4 QDs was observed to be reinstated (**Fig. 19a**). The utilization of TA-g-C_3N_4 QDs-based probe has enabled the detection of AA with a limit of detection of 50 pM and a linear analytical range, spanning from 0.1 to 200 nM of AA. Furthermore, Xie et al. [204] developed a sensor utilizing g-C_3N_4 QDs for the purpose of detecting AA without the need for labeling and with notable sensitivity and specificity. They reported the successful synthesis of g-C_3N_4 QDs with desirable characteristics, including a high quantum yield of 21%, as well as excellent water solubility. The synthesis involved employing g-C_3N_4 sheets and ethylenediamine as precursors, followed by a hydrothermal treatment at 180 °C for 6 h. The synthesized g-C_3N_4 QDs possessed a significant number of amino groups, and the AA was present in its anionic state under physiological pH conditions. The interaction of electrostatic nature between g-C_3N_4 QDs and AA has the potential to impede the excitation and emission of the lone pair states in the g-C_3N_4 QDs (**Fig. 19b**). This property renders g-C_3N_4 QDs capable of detecting AA in a highly sensitive and selective manner across a broad range spanning from 0.5 to 200 μM, with a detection threshold of 150 nM.

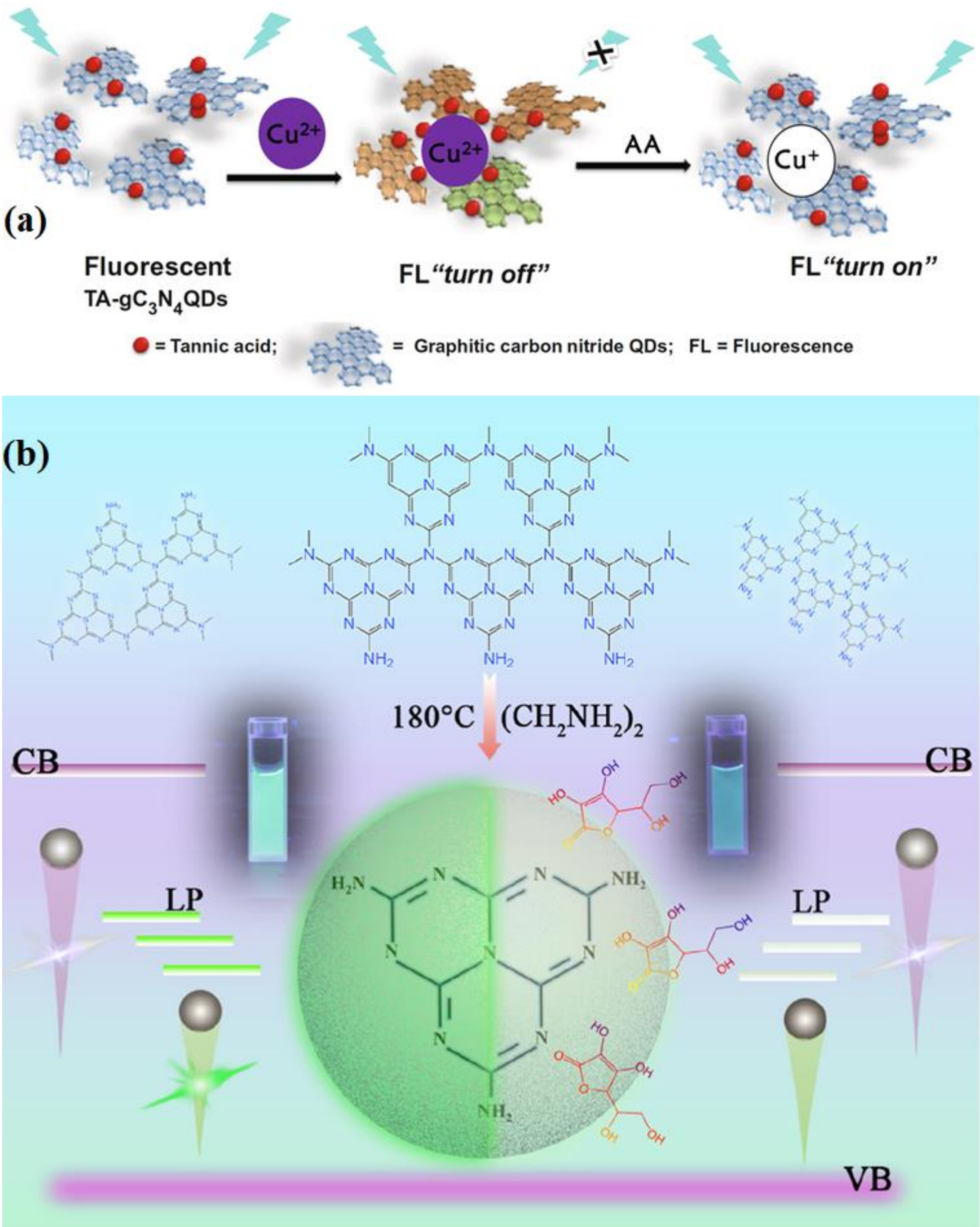

Fig. 19. (a) Fluorescence 'on-off-on' schematization AA sensing via TA modified g-C_3N_4 QDs in the presence of Cu^{2+}. Reproduced with permission from [192]. (b) g-C_3N_4 QDs synthesis with the presence of ethylenediamine and working mechanism of AA sensing. Reproduced with permission from [204].

The measurement of glucose levels in the bloodstream has proven to be a significant issue for several decades, as it is a crucial aspect of managing diabetes mellitus and other metabolic disorders that have seen a surge in patient numbers [205]. Significant advancements have been made in the development of a glucose level detection sensor utilizing g-C_3N_4 QDs. Ngo and colleagues [188,189] presented two fluorescent materials for glucose sensing under physiological pH conditions. These materials were based on phenylboronic acid (PBA) functionalized g-C_3N_4 QDs (PBA-g-CNQDs) and 3-aminophenylboronic acid (3APBA) functionalized g-CNQDs (3APBA-g-CNQDs). The PBA-g-CNQDs were synthesized through a top-down approach utilizing melamine as the sole precursor. Subsequently, surface modification of the g-C_3N_4 QDs was carried out using PBA molecules that exhibit glucose-responsive behavior. The fluorescent properties of g-C_3N_4 QDs in PBA-g-CNQDs sample can be utilized as a means of encoding, while the PBA molecule present in PBA-g-CNQDs can function as both a quencher and receptor in the process of glucose sensing. Upon the addition of glucose to the solution containing PBA-g-CNQDs, the boronic acid molecules present in PBA underwent a conversion process, resulting in the formation of anionic glucoboronate esters with a tetrahedral structure. The boronate complexes that were produced as a result of the experiment exhibited a negative charge (**Fig. 20a**). The glucose sensor utilizing PBA-g-CNQDs exhibited a notable sensitivity, featuring a detection limit of 16 nM, and demonstrated exceptional selectivity in the presence of diverse interfering reagents. The case of 3APBA-g-CNQDs reveals that g-C_3N_4 QDs exhibit comparable performance to PBA-g-CNQDs in terms of exceptional selectivity, favorable biocompatibility, and minimal cytotoxicity. Additionally, g-CNQDs exhibit the highest recorded maximum quantum yields to date, reaching up to 78%. Basically, the introduction of 3-APBA into an aqueous solution of 1-ethyl-3-(3-dimethylaminopropyl)carbodiimide (EDC) and phosphate-buffered saline (PBS) containing g-C_3N_4 QDs results in a significant increase in the fluorescence intensity. The observed phenomenon can be explained by the inhibition of photo-induced electron transfer (PET), which can be attributed to the effective development of the fluorescent structure between the protonated tertiary amino group and the negatively charged hydroxylated boronic acid ester through hydrolysis in the PBS buffer solution (**Fig. 20b**).

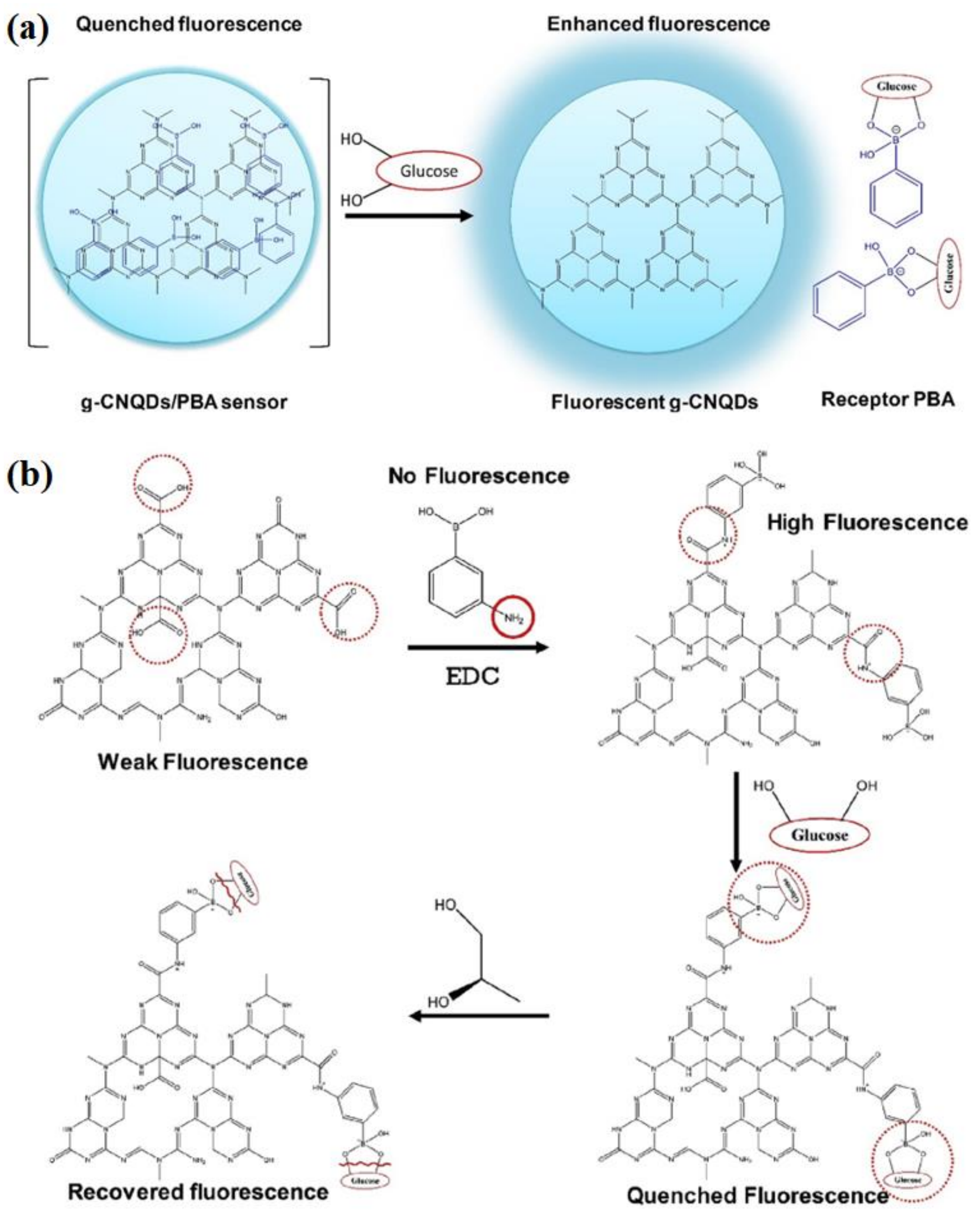

Fig. 20. (a) Sensing mechanism of glucose using g-CNQDs/PBA material. Reproduced with permission from [188]. (b) g-CNQDs/3APBA sensing mechanism-based fluorescence sensor "on-off" for glucose and "on-off-on" for propylene glycol. Reproduced with permission from [189]

Recently, Weng et al. [190] created a glucose sensor utilizing Fe-doped g-C_3N_4 QDs (Fe-g-CNQDs) that were synthesized through a one-pot solvothermal treatment using citric acid, urea, and ferric chloride as precursors. The as-synthesized Fe-g-CNQDs demonstrated peroxidase-like characteristics, capable of facilitating the catalytic oxidation of tetramethylbenzidine (TMB) through hydrogen peroxide (H_2O_2). The oxidation process of glucose catalyzed by glucose oxidase

(GOD) resulted in the generation of H_2O_2. Based on these findings, the utilization of Fe-g-CNQDs as a dual-platform for the detection of H_2O_2 and glucose is a novel approach that combines the catalytic properties of GOD with Fe-g-CNQDs. The detection limits for the H_2O_2 and glucose sensors based on Fe-g-CNQDs were 0.21 and 0.29 μM, respectively.

Heparin serves as an anticoagulation that stops blood clots from forming as a result of certain illnesses or surgical operations. Prior to surgery, heparin is often administered to the patient to lower the risk of blood clots. Lately, Cheng et al. [83] designed a g-C_3N_4 QD based sensor for heparin detection. The sensor, labeled as Ag-g-CNQDs/PEI, was created by coating the Ag/g-C_3N_4 QDs (Ag-g-CNQDs) composite with polyethylenimine (PEI) (**Fig. 21a**). The fluorescence of Ag-g-CNQDs at an emission wavelength of 600 nm was significantly reduced due to the surface coating. But since PEI has a greater affinity for heparin than Ag-g-CNQDs, the Ag-g-CNQDs showed a noticeable increase in the fluorescence intensity following the addition of heparin. With a detection limit of 8.2 nM, this g-C_3N_4 QDs based sensor has shown to be a good candidate for a fluorometric test of heparin.

Dopamine is a neurotransmitter, or chemical messenger, that is produced by brain nerve cells and communicates with other nerve cells. One of the various dopamine channels found in the brain is crucial to the motivational aspect of conduct prompted by rewards. Fan et al. [112] produced a g-C_3N_4 QD-based CL sensor for the detection of dopamine. The radiative recombination of the thermally excited electrons and the oxidant-injected holes in the g-C_3N_4 QDs resulted in a substantial CL emission in the presence of $K_3[Fe(CN)_6]$ (**Fig. 21b**). When dopamine was added, the CL intensity of the g-C_3N_4 QDs and $K_3[Fe(CN)_6]$ mixture was drastically suppressed due to the competition between dopamine and g-C_3N_4 QDs for $K_3[Fe(CN)_6]$. With a detection limit of 4.7 nM, such a sensor may be utilized to measure dopamine in the range of 1×10^{-8} to 2×10^{-6} M. Real serum samples were examined to establish the validity of the methodology, which showed great sensitivity and good recoveries.

The buildup and aggregation of β-amyloid (Aβ) peptide in brain is known to be a starter for the onset of Alzheimer's disease (AD). A transmembrane protein (amyloid precursor protein) is typically proteolyzed to produce β- and γ-secretases. A g-C_3N_4 QD based sensor for the detection of Aβ monomer was developed by Zhang et al. [206]. The g-C_3N_4 QDs were first coordinated with Cu^{2+}, which caused their fluorescence to be quenched as a result of the formation of the chelate (Cu^{2+}-g-C_3N_4 QDs). Due to the aggregation of Aβ monomer on the surface of g-C_3N_4 QDs, the addition of Aβ monomer further quenched the fluorescence of Cu^{2+}-g-C_3N_4 QDs chelate (**Fig. 21c**). With a low detection limit of 0.18 ng mL^{-1} for $A\beta_{1-42}$, the sensor based on the Cu^{2+}-g-C_3N_4 QD chelate displayed a broad linear range from 1 to 700 ng mL^{-1}.

The detection of phenolic substances, a category of contaminants that are hazardous to both human beings and ecosystem, is very important to the daily lives of people. Coupling the distinct optical characteristics of g-C_3N_4 QDs with the selectivity of enzymatic reactions, Lu et al. [207] created a g-C_3N_3 QD based sensor for phenolics. According to their findings, both hydroquinone (HQ) and benzoquinone (BQ) directly or indirectly extinguished the fluorescence of g-C_3N_4 QDs. Horseradish peroxidase's (HRP) catalytic oxidation of HQ in the presence of H_2O_2 results in a generation of quinone, which was thought to be the process responsible for quenching (**Fig. 21d**). The triggered transfer of electrons from the CB of g-C_3N_4 QDs to their VB allowed the quinone to successfully extinguish the fluorescence of the g-C_3N_4 QDs. With a linear range of 0.5-11.6 M and a detection limit of 0.04 nM (S/N=3), the g-C_3N_4 QD based sensor is capable of measuring HQ.

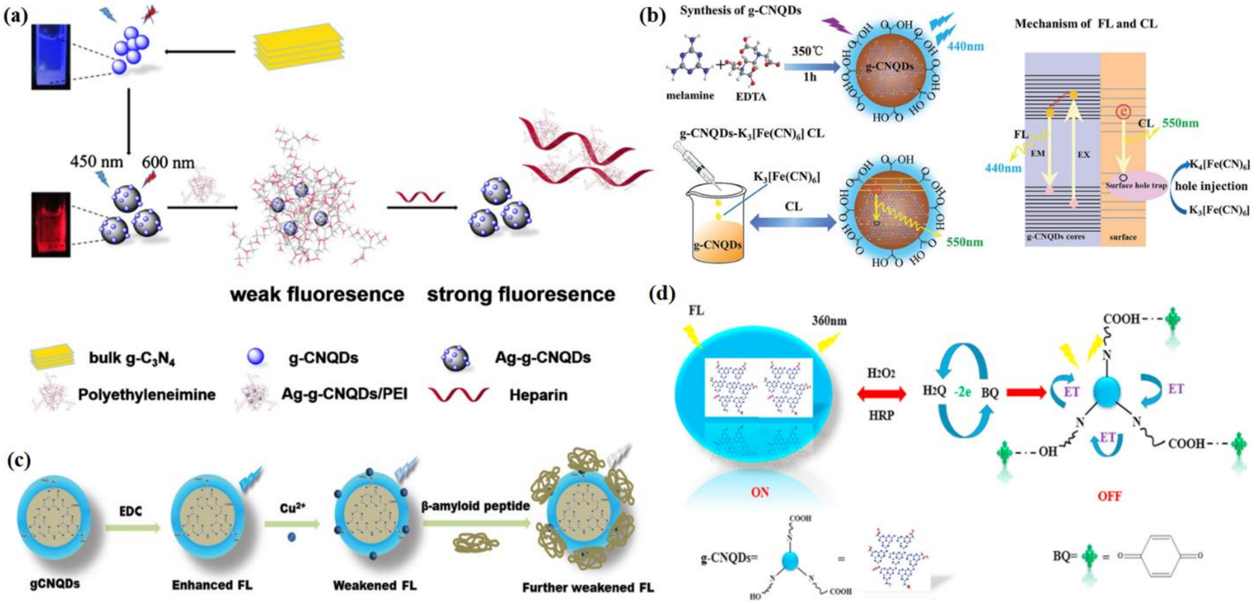

Fig. 21. (a) Illustrative representation Ag-g-CNQDs preparation for heparin detection. Reproduced with permission from [83]. (b) Illustrative representation for g-C_3N_4 QDs–$K_3[Fe(CN)_6]$ preparation and CL mechanism for dopamine. Reproduced with permission from [112]. (c) Illustrative representation of g-C_3N_4 QDs based fluorescent probe mechanism for sensing of the Aβ peptide. Reproduce with permission from [206]. (d) Schematic illustration of the detection mechanism of HQ via g-C3N4 QDs-HRP enzymatic reaction. Reproduced with permission from [207].

4.4. Optoelectronics: Solar cell and Light-emitting diode

The unique size effect is largely responsible for the optical and PL characteristics of g-C_3N_4 QDs. Due to their high light absorption efficiency, g-C_3N_4 QDs can be used as photosensitizers in photo(electro)catalytic reactions. Since g-C_3N_4 QDs have unique PL and UCPL properties, they can be used as spectral converters in photocatalysis. In particular, the UCPL behavior can make it possible to use the NIR light with longer wavelengths. PL in g-C_3N_4 QDs is caused by the optical selectivity of different-sized nanodots (quantum effect), emissive traps on the surface such as defects, surface groups, and surface states. However, more research is needed to fully understand how PL works. The UCPL behavior, on the other hand, is often thought to have come from the multiphoton active process. With these optical properties, g-C_3N_4 QDs have a wide range of uses, in optoelectronics, biomedical and photocatalysis applications. For example, Xiang et al. [131] successfully utilized g-C_3N_4, for the first time, in bulk heterojunction (BHJ) polymer solar cells (PSCs) by doping solution-processable g-C_3N_4 QDs in the active layer for efficiency improvement. This approach introduced a new usage of g-C_3N_4 in energy conversion applications beyond the commonly used photocatalysts. **Fig. 22** shows the schematic illustration of the BHJ-PSC device fabrication and its performance results. When g-C_3N_4 QDs were added to the PSCs, the power conversion efficiencies of inverted BHJ-PSC devices with different polymer active layers, such as P3HT:PC_{61}BM, PBDTTT-C:PC_{71}BM, and PTB7-Th:PC_{71}BM reached 4.23%, 6.36%, and 9.18%, respectively, which are higher than the standard (undoped) devices by 17.5%, 11.6%, and 11.8%, respectively. External quantum efficiency (EQE) tests showed that the increase in short-circuit current was the main reason why the g-C_3N_4 QDs-doped BHJ-PSC device had a higher power conversion efficiency. The effects of g-C_3N_4 QDs on the surface morphology, optical absorption, and PL properties of the active layer films, as well as the charge transport property of the devices, were further studied. It was found that the efficiency improvement of the BHJ-PSC devices upon g-C_3N_4 QDs doping was due to a combination of effects, such as better interfacial contact between the active and hole transport layers and photoinduced electron transfer between the donor (conducting polymer) and acceptor (fullerene). This study opens a new path for integrating semiconducting photocatalysts into BHJ-PSCs to improve performance [208], in addition to providing conceptually new insights into g-C_3N_4 and its QDs beyond the commonly used photocatalysts.

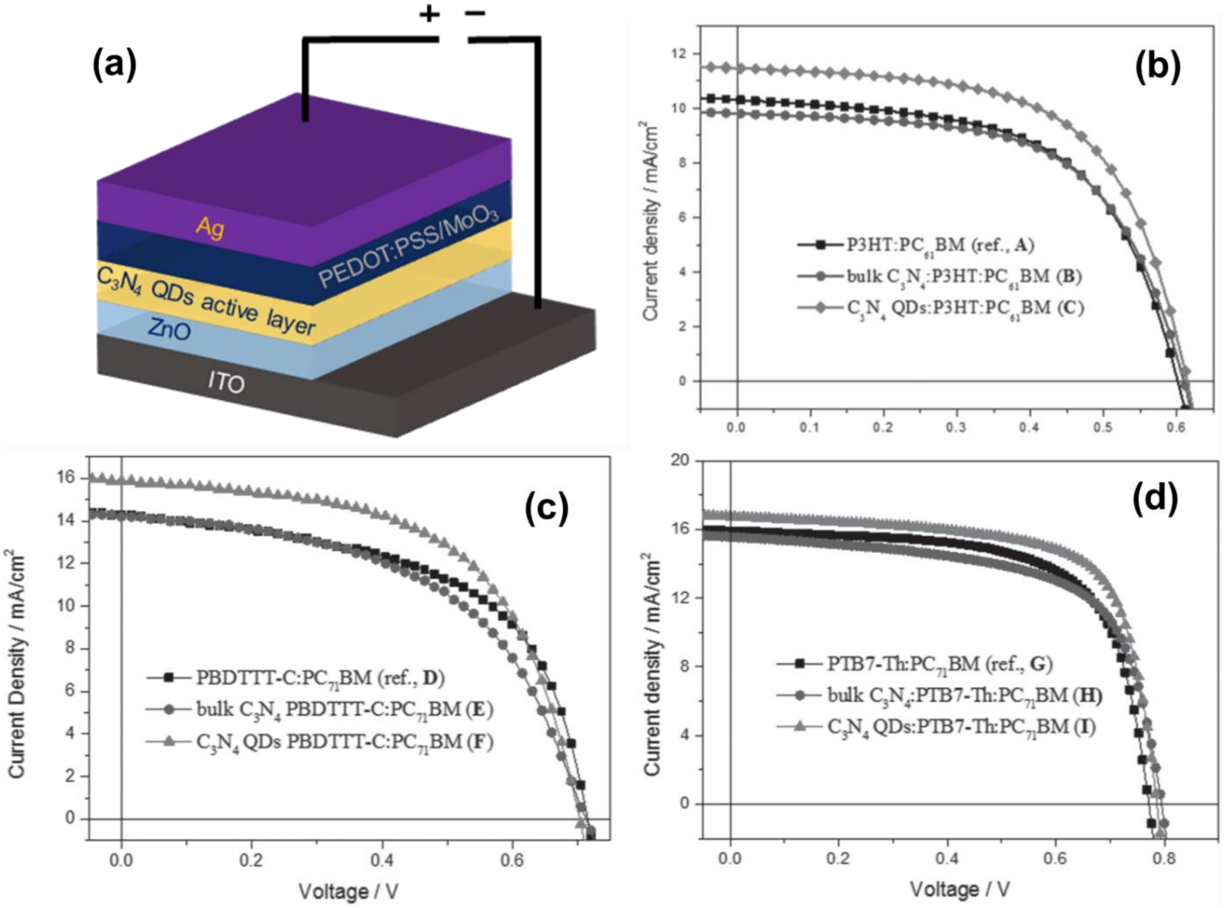

Fig. 22. (a) Schematic illustration of BHJ-PSC device fabrication, (b) *J*-*V* curves of ITO/ZnO/C_3N_4:P3HT:$PC_{61}BM$/PEDOT:PSS/Ag, (c) ITO/ZnO/C_3N_4:PBDTTT-C:$PC_{71}BM$/MoO_3/Ag and (d) ITO/ZnO/C_3N_4:PBT7-Th:$PC_{71}BM$/MoO_3/Ag with undoped and g-C_3N_4 or g-C_3N_4 QDs doped devices tested under illumination of an AM 1.5 solar simulator (100 mW cm^{-2}) in air. Reproduced (adopted) with permission from [131].

g-C_3N_4 QDs are naturally suited for light-emitting devices due to their quantum size, high PL quantum yield, and remarkable physicochemical properties. Because of their excellent dispersibility in most organic solvents, they have a great potential to be used in light-emitting devices and flexible transparent displays, such as smart windows for advertising [129,209]. For example, Liangrui et al. [210] fabricated the quantum dot light-emitting diode (QLED) by employing g-C_3N_4 QDs as an emitting layer via the spin-coating technique (**Fig. 23a**). Thermal evaporation was used to create the LiF/Al electrode. **Fig. 23b** illustrates the corresponding energy levels of the various thin-film layers, and the off-and-on states of the device at an applied voltage of 21 V are shown in **Fig. 23c**. The electroluminescence spectra displayed in **Fig. 23d** features two bands, one at 427 nm and another at 513 nm, rather than the single peak at around 435 nm reported by Chen [209]. **Fig. 23e** shows that the luminescence increases almost linearly with the applied voltage. From the data, it can be inferred that the peaks at 427 and 513 nm are caused by the interference of electrons and holes injected at unoccupied δ* and π* orbitals in the CB and loan pair states in the VB, respectively. The mechanism described in **Fig. 23f** can therefore explain the electroluminescence. In another study, Xingchen et al. [71] used a similar device configuration on ITO/PEDOT:PSS/PVK/OMIM-g-C_3N_4 QDs/TPBi/LiF/Al (**Fig. 24**) to fabricate QLED. In this work, the bright blue-emitting g-C_3N_4 QDs were obtained from bulk g-C_3N_4 via the one-pot methylamine intercalation–stripping method. The obtained g-C_3N_4 QDs were more suitable for the solution-processed thin film fabrication than previously reported QDs because of their low polydispersity and increased solution stability thanks to their high absolute zeta potential (41.23 mV). These QDs can be spin-coated to uniform films with low surface roughness, making them suitable for use in the fabrication of QLEDs. When incorporated into a functional QLED with OMIM g-C_3N_4 QDs as the emitting layer, the LED demonstrated 60 times higher luminance (605 vs. 11 Cd m^{-2}) at a lower operating voltage (9 vs. 21 V), as compared to the previously reported first-generation g-C_3N_4 QLEDs [210]. Bright blue light was emitted from the QLEDs with an electroluminescence peak at 438 nm (similar to the PL of OMIM g-C_3N_4 QDs shown in **Figs. 24c and 24d**).

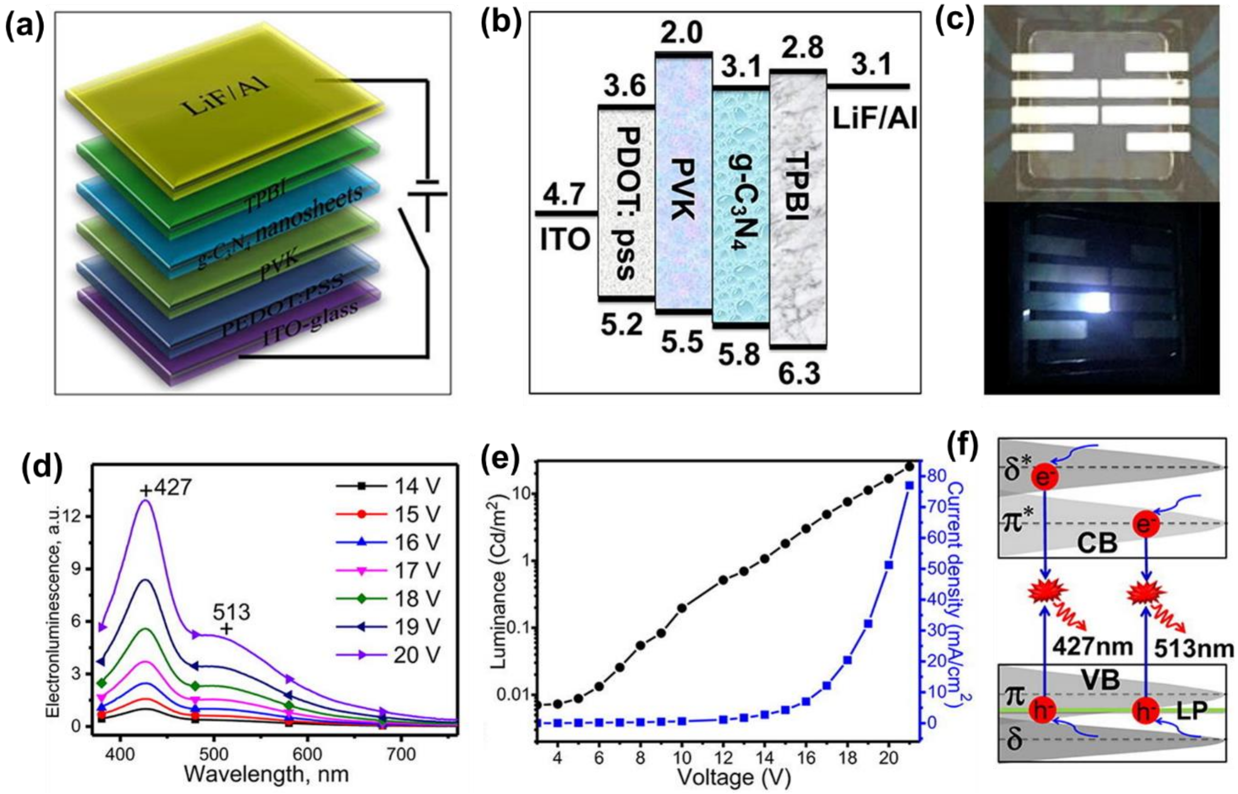

Fig. 23. QLED devices fabricated using g-C_3N_4 QDs. (a) A schematic illustration of the QLED device structure; (b) the energy level diagram of various thin-film layers, (c) the as-prepared QLED device in visible light and a photograph of the light-emitting device with an applied voltage of 21 V, (d) electroluminescence spectra of the as-prepared QLED device; (e) the brightness and current density as a function of the applied voltage; and (f) plausible mechanism of electroluminescence of g-C_3N_4 QDs. Reproduced with permission from [210].

Fig. 24e shows that the QLED has a relatively high current efficiency of 0.09 cd A^{-1}, and **Fig. 24f** illustrates that the applied voltage increases with the electroluminescence intensity. However, at a luminance of 100 cd m^{-2} in air, the QLEDs exhibited low operational stability. The brightness decreased to less than 50% of the initial value after 200s, indicating a need for further optimization of the device construction. Due to the poor solubility of white light-emitting g-C_3N_4 QDs in solvents, the first UV-pumped WLED was fabricated by directly coating W-CNQD phosphorus with Super Glue® (cyanoacrylate) on the surface of a standard 380 nm UV-LED (**Fig. 24g**) [129]. Under a 20 mA forward bias current, the LED emits efficient white light. Also, when the electrical excitation was turned off, the LED showed yellow phosphorescence. **Fig. 24h** shows that the electroluminescence spectrum of an efficient single-component WLED based on white g-C_3N_4 QDs phosphorus covers a wide range from 380 to 780 nm. Two clear peaks are discernible: one at 450 nm, which is caused by blue fluorescence, and another at 570 nm, which is caused by yellow phosphorescence. Electroluminescence spectra exhibit a distinct red shift that results from reabsorption compared to the steady-state PL spectra. The commission Internationale de l´Eclairage (CIE) chromaticity coordinates of the WLED lamps were (0.35, 0.39) (**Fig. 24i**), which gave it a orrelated color temperature (CCT)of 4935 K. The WLED made from white g-C_3N_4 QDs has a CRI value of 85, the same as some of the most advanced single-component WLEDs made from semiconductor QDs and lead halide perovskites. The single-component WLED lamp exhibited high device stability after 72 h of operation, and good chromatic stability with an applied current increasing from 20 to 90 mA. g-C_3N_4 QDs embedded in PVA transparent films have also been utilized for LED application. By adding 10 wt.% g-C_3N_4 QDs to PVA, 40% transparency was retained without changing the optical properties of the polymer. Emission was shown to be wavelength-independent and confined to the 510–530 nm range when CN-QDs were encapsulated in a PVA matrix. A white light emission was observed, as shown in **Figs. 24j** and **24k**, while combining 10% g-C_3N_4 QDs with the PVA film on a blue LED (InGaN) chip [159]. Compared to conventional light emitters used in LEDs, such as conjugated polymers [211–215], organic and inorganic small molecules [216–220], donor–acceptor molecules [221–223], and halide perovskite nanocrystals [220,224–226], g-C_3N_4 QDs are more cost-effective and have the potential to be made on a larger scale without any toxic effect on the environment. It is still necessary, however, to optimize the performance of g-C_3N_4 QDs in QLED devices to meet the high-quality requirement of displays for high-definition, high-luminance, and high-accuracy pictures. This includes emission color chromaticity and color saturation (determined by emission peak wavelength and bandwidth), luminance, and energy conversion efficiency of electroluminescence.

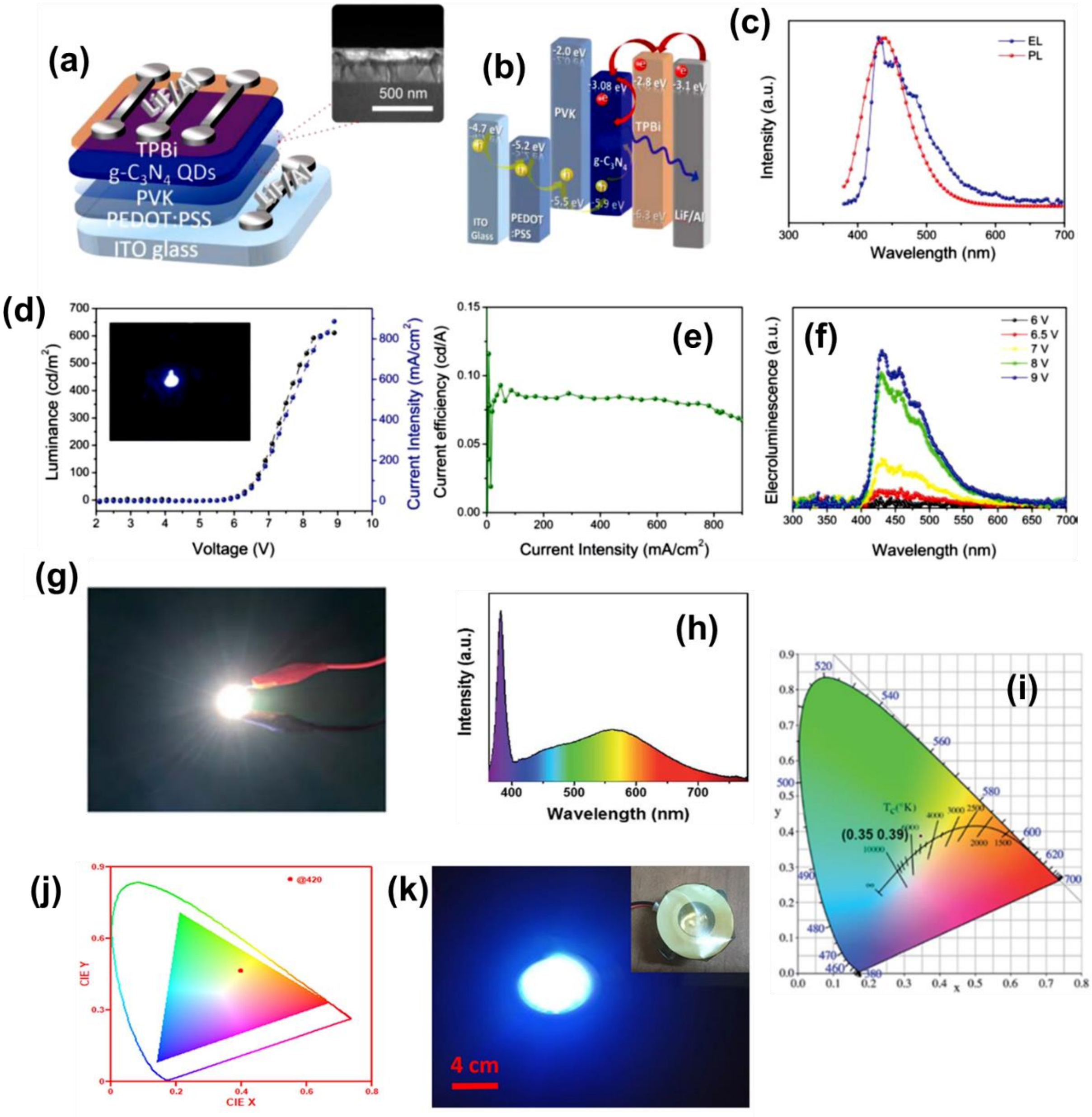

Fig. 24. (a) Schematic illustration of device structure, (b) energy level diagram, (c) PL (excited at 360 nm) and electroluminescence spectra of g-C_3N_4 QDs. (d) *J-V-L* curves (e) CE-I curve of g-C_3N_4 QDs QLED device and (f) electroluminescence spectra g-C_3N_4 QDs fabricated QLED with different applied voltage. Reproduced with permission from [71]. (g) UV pumped WLED device fabricated with g-C_3N_4 QDs as phosphors. (h) electroluminescence

spectrum and (h) CIE coordinates of white g-C_3N_4 QDs LED. Reproduced with permission from [129]. (j) CIE coordinates and (k) g-C_3N_4 QDs embedded PVA transparent film on blue LED chip. Reproduced with permission from [159].

4.5. Biomedical Applications

The use of g-C_3N_4 QDs in biomedical applications has been gaining much attention due to their superior properties to traditional semiconductor QDs. The former are free from metals, making them safer for use in living organisms. In addition, their surface can be easily modified to provide low cytotoxicity and selectivity to the specific cell organelles. One of the most remarkable features of g-C_3N_4 QDs is their unique optical properties, which surpasses those of both organic dyes and conventional QDs. They have the ability to modify excitation wavelengths and exhibit a higher PL quantum yield. This makes them highly suitable for bioimaging applications, as they can provide high-quality images with minimal damage to living tissues. Moreover, g-C_3N_4 QDs have a small size distribution of less than 20 nm, which enhances their stability and biocompatibility with living organisms. They can be used as efficient nanocarriers for targeted molecules and anti-cancer drugs, thanks to their conjugated electronic structures and active surface groups. Due to their inherent properties, g-C_3N_4 QDs are a highly promising biomaterials for clinical use. Extensive research has been conducted on their potential biomedical applications, including drug carrier and therapeutics. With their remarkable properties, g-C_3N_4 QDs are poised to revolutionize the field of biomedical research and clinical practice.

4.5.1. Cytotoxicity

Despite the outstanding uses of g-C_3N_4 QDs in drug delivery and bioimaging, the issue of toxicity needs to be addressed before they become widely used in biomedicine. *In vivo* (the entire living organism considered to be the test subject) and *in vitro* (living cells taken from the organism considered to be the test subject) tests are typically used to determine the level of the toxicity of a substance. The term “cytotoxicity” can also be used to refer to “*In vitro* toxicity.” To study the toxicity of g-C_3N_4 QDs, both *in vitro* and *in vivo* tests have been conducted. For example, *In vitro* tests have been carried out on various human or animal cells, including Hela cells, MDC-803, H196, MCF-7 cells, HepG2, brain tumor cells, L929 fibroblast cells, Ocular Choroidal Melanoma-1 (OCM1), red blood cells, etc. (**Fig. 25**) [53,70,78,85,123,138,227] . In contrast to GQDs, *in vivo* tests of g-C_3N_4 QDs are only conducted with mice as the test subjects. The toxicity tests included not just pristine g-C_3N_4 QDs but also doped g-C_3N_4 QDs and nanocomposites (e.g., p-doped g-C_3N_4 QDs and CuS-g-C_3N_4 QDs). It is important to note that there are more *in vitro* tests available in literature than *in vivo* tests. Although studies have focused on improving the optical features of g-C_3N_4 QDs, it is important to note that their biocompatibility is still essential for *in vivo* applications. When a material interacts with an organism, it is considered biocompatible if it fulfills its intended function without causing any harmful biological reactions. g-C_3N_4 QDs are a safe alternative to metal-based nanoparticles because they have excellent solubility in water and are composed solely of carbon. However, toxicity may occur due to aggregation in some carbon-based nanoparticles.

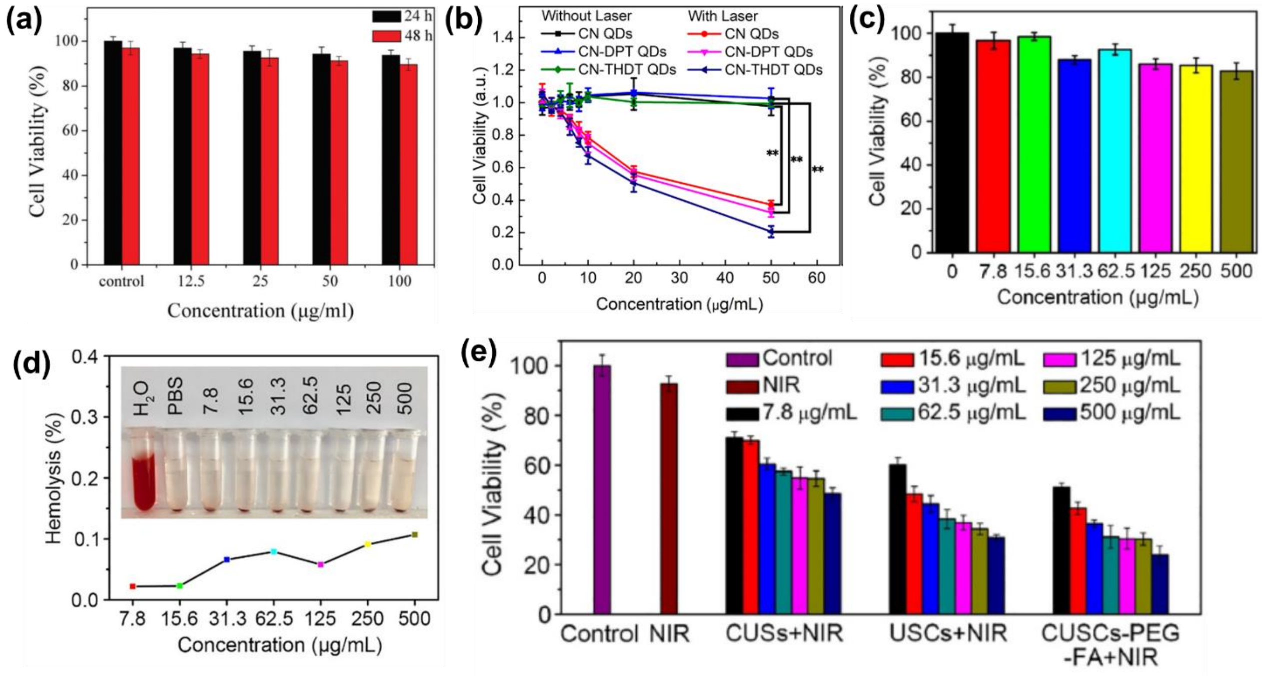

Fig. 25. (a) Cell viability of HeLa cells incubated with g-C_3N_4 QDs. Reproduced with permission from [75]. (b) MCF-7 cells were treated with CN, CN-DPT, and CN-THDT QDs for a period of 24 hours with or without the application of laser irradiation (800 nm, 1.0 W/cm^2, for 20 minutes). Reproduced with permission from [123] (c) Hemolytic assay and (d) cell viability of g-C_3N_4 QDs/PEG with nanocomposite incubated with human red blood cells and L929 fibroblast cells respectively. (e) The effect of near-infrared light (NIR) on the viability of HeLa cells cultured *in vitro* for 24 hours with various concentrations of CUSs, USCs, and CUSCs-PEG-FA. Reproduced with permission from [228].

4.5.2. Bioimaging

The use of bioimaging enables the precise and thorough examination of biological processes, such as drug delivery, cellular uptake, and biodistribution, by utilizing various wavelengths of electromagnetic radiation to isolate and observe them in detail. Accurate imaging is crucial in detecting cancer, allowing for early detection of tumors, and monitoring the spread or recurrence of the disease. Fluorescent imaging is the preferred method for biomedical applications due to its high resolution, rapid response, non-invasiveness, and ability to provide *in situ* and real-time information at the cellular or molecular level. Other bioimaging methods, such as magnetic resonance imaging (MRI), positron-emission tomography (PET), computed tomography (CT), ultrasound imaging are also used. However, the biggest challenge is ensuring that stable PL probes are designed and synthesized for fluorescent imaging. Because of their controllable fluorescence emission, high quantum yield, low toxicity, excellent biocompatibility, and resistance to photobleaching, g-C_3N_4 QDs have emerged in recent years as attractive alternatives to traditional QDs and organic dyes [227]. Recent studies have demonstrated that biocompatible g-C_3N_4 QDs are effective for both NIR fluorescence and MRI imaging, making them suitable for a variety of bioimaging tasks.

4.5.2.1. Fluorescence imaging

Fluorescence imaging is a critical technique in biomedical applications, providing in-depth analysis of the distribution of molecules of interest in cells and tissues. Visible light, two-photon, and NIR are utilized for this purpose, and the results have proven to be highly effective. With applications ranging from disease diagnostics to monitoring therapies and subcellular imaging, fluorescence imaging plays a vital role in the field. Probes, specific molecules that produce PL, are utilized to achieve these outcomes. The extensive use of fluorescence imaging in both laboratory and clinical settings is evidence of its success. Fluorescent probes, i.e., organic dyes and fluorophores, are widely used in a variety of *in vitro*, *in vivo*, and *ex vivo* settings. However, it is imperative to consider solubility when determining the compatibility of substances for use in human or animal bodies. As many fluorophores lack water solubility, an additional bioconjugation process is often a prerequisite [227,229–232]. For example, bright blue-emitting g-C_3N_4 QDs were developed by Zhan et al.[75] via the ethanol-thermal treatment of bulk g-C_3N_4. After 5 h of treatment with g-C_3N_4 QDs, the blue fluorescence of Hela cells at an excitation wavelength of 405 nm was clearly visible, as shown in **Figs. 26a-c**. Furthermore, no substantial fluorescence quenching of Hela cells treated by g-C_3N_4 QDs was observed following continuous irradiation for 5 h, suggesting that g-C_3N_4 QDs possess good photostability and are suitable for long-term cellular imaging. In another example, UV light exposure did not significantly affect the photostability of phosphorous-doped QDs [78]. After 2 days of irradiation, the P-g-C_3N_4 QDs retained 94% of their initial photoluminescence intensity, while the stabilities of g-C_3N_4 QDs and GQDs were lower. This was attributed to the stable lattice doping structure of P-g-C_3N_4 QDs. Additionally, even at high concentrations (up to 400 g mL^{-1}), P-g-C_3N_4 QDs did not noticeably harm cells *in vitro*. **Figs. 26d-**

f show that cell viability during the incubation process remained at or above 95% (healthy cells are green and dead cells are red). Finally, tests on OCM-1 cells suggested that P-g-C_3N_4 QDs could be a viable bioimaging materials for clinical use. Since cancer cells are typically more resistant to chemical compounds, human umbilical vein endothelial cells (HUVEC) were used instead. The oxygen and sulfur co-doped g-C_3N_4 QDs (OS-g-C_3N_4 QDs) possess high biocompatibility and low cytotoxicity with HUVEC, indicating their potential use in cell imaging [138]. Confocal images of HeLa cells treated with 75.0 ng mL^{-1} of OS-g-C_3N_4 QDs are shown in **Figs. 26g-j**. The fluorescence increases as the concentration of OS-g-C_3N_4 QDs increases and vice versa. It is important to note that the concentration of OS-g-C_3N_4 QDs used in the *in vitro* evaluation was significantly higher (75.0 g mL^{-1}) and the incubation time was longer (24 h). These findings suggest that OS-g-C_3N_4 QDs have a higher level of biocompatibility, making them suitable for use in *in vivo* applications such as bioimaging. When HeLa cells were not incubated with OS-g-C_3N_4 QDs solution, there was no fluorescence reaction at the wavelength of 488 nm (**Figs. 26g** and **26h**). Following incubation, the cytoplasm of the cells exhibited a bright lime green color when excited by a wavelength of 488 nm. This indicates that OS-g-C_3N_4 QDs can easily penetrate the cytoplasm and label it, exemplifying the significantly increased fluorescence performance of OS-g-C_3N_4 QDs as fluorescent probes in bioimaging. As a result, OS-g-C_3N_4 QDs could potentially be used to investigate labeled cytoplasm. Ying Yin et al. [85] used urethral epithelial cells (SH1 cells) to investigate how g-C_3N_4 QDs are absorbed by cells and their effectiveness within the body. In **Figs. 26k-n**, a blue area is visible within the SH1 cells under UV light, indicating that the g-C_3N_4 QDs penetrated the cell membrane without the need for bioconjugation. The PL of g-C_3N_4 QDs remained stable under light when continuously excited for 20 min, as evidenced by the PL brightness not changing significantly. To assess their compatibility with living things, the MTT test was conducted on SH1 cells after being incubated with g-C_3N_4 QDs for 48 h. The cell survival rate remained unchanged at concentrations of 150, 300, and 600 g/mL, with the latter being several times higher than the concentration used in bioimaging studies. This indicates that the g-C_3N_4 QDs did not harm the cells and were biocompatible even at high concentrations. Additionally, the cell viability remained stable even after three days, demonstrating that g-C_3N_4 QDs are a suitable fluorescent probe for cell labeling. The g-C_3N_4 QDs exhibited not only monochromatic fluorescence emission described above, but also a wide range of fluorescence colors in response to a variety of excitation wavelengths.

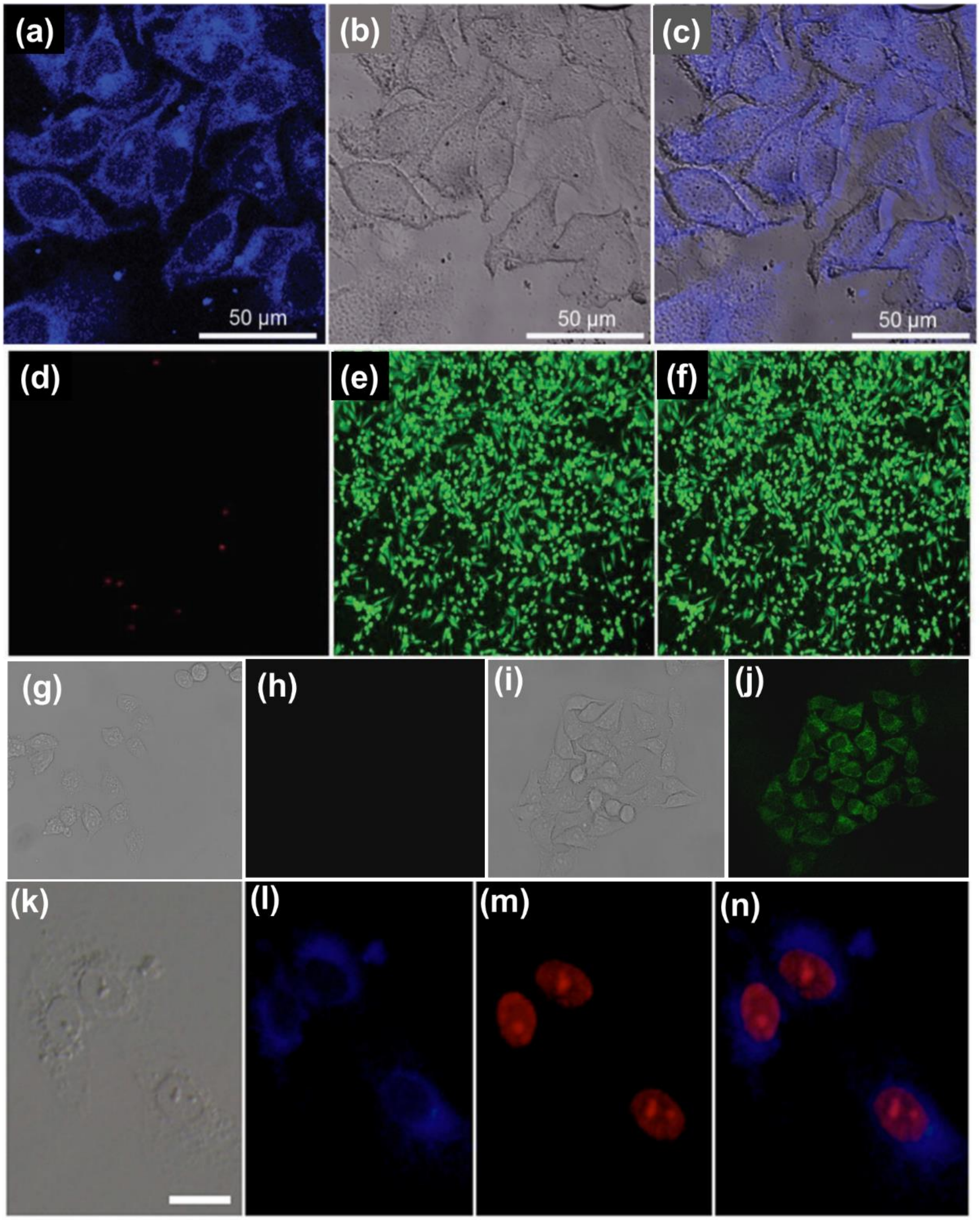

Fig. 26. HeLa cells incubated with g-C_3N_4 QDs for 5 hours (a) as seen by confocal fluorescence microscopy (ex = 405 nm). (b) Cells photographed in bright field microscope. (c) A merged image consisting of (a) and (b). Reproduced with permission from [75]. (d-f) The green and red lights showed which OCM-1 cells were alive and which ones were dead. The live/dead cell viability kit (Thermo Fisher Scientific) used to determine the percentage of viable OCM-1 cells following a 24-hour incubation period. Reproduced with permission from [78]. Confocal images of Hela cells without (g&h) and with (i&j) OS-g-C_3N_4 QDs were captured under bright field (g&h) at an excitation wavelength of 488 nm (i&j). Reproduced with permission from [138]. (k-n) SH1 cells were exposed to g-C_3N_4 QDs for a period of 24 hours before being imaged using fluorescence (excitation at 380 nm). Reproduced with permission from [85].

Zhou et al. [58] described that g-C_3N_4 QDs exhibit a visible-range-spanning, excitation-wavelength-tunable fluorescence emission. Specifically, HEK 293T cells treated with g-C_3N_4 QDs exhibited strong multicolor fluorescence emission with excitation at 405, 488, and 543 nm after 24 h of incubation. With these characteristics, metal-free g-C_3N_4 QDs may be promising candidates for use as bioimaging biomarkers. Zhuang et al. [233] discovered that bright green-emitting g-C_3N_4 QDs can be synthesized through hydrothermal synthesis at 200 °C for 2 h using human urine as the precursor. When HepG2 cells were exposed to g-C_3N_4 QDs at a concentration of 0.2 mg mL^{-1} for 4 h, they emitted blue light at 405 nm and green light at 488 nm in response to 405 nm and 488 nm stimulation, respectively. In another example, Liyanage et al. [234] reported on the *in vitro* cellular selectivity and distribution of g-C_3N_4 QDs with SJGBM2 and HEK293 cells under different excitation wavelengths. Cells can be imaged in multiple wavelengths thanks to the excitation-dependent emission property. It is worth mentioning that blue autofluorescence is emitted by living cells and organisms due to NADPH, proteins, and other amino-functional fluorophores [235]. Therefore, blue-emitting bioimaging markers are not particularly useful due to the potential of autofluorescence for interference. However, multicolor emissive g-C_3N_4 QDs are facilitating high-quality, red-region cellular imaging even at longer wavelengths. In a work by Liyanage eat al. [234] g-C_3N_4 QDs were derived from the combination of citric acid with urea and selenourea and utilized for bioimaging because of their high PLQY, strong stability, and low cytotoxicity. The g-C_3N_4 QDs were able to selectively penetrate the cytoplasm of SJGBM2 tumor cells and emit strong PL in wavelengths associated with the red region of the light spectrum (**Fig. 27a**). In general, if the nanomaterial effectively passes the blood-brain barrier and enters the central nervous system, this labeling technique may prove to be beneficial in the identification of tumors, as well as in fluorescence-guided brain surgery. It was discovered that the g-C_3N_4 QDs entered the lysosome approximately 6 h after being taken in by the cells (**Figs. 27b** and **27c**). This demonstrates that g-C_3N_4 QDs are capable of biodegradation. In addition, the g-C_3N_4 QDs nanomaterial has the potential to function as an effective delivery vehicle for medications that are to be delivered within the cell via a pH change inside the lysosome.

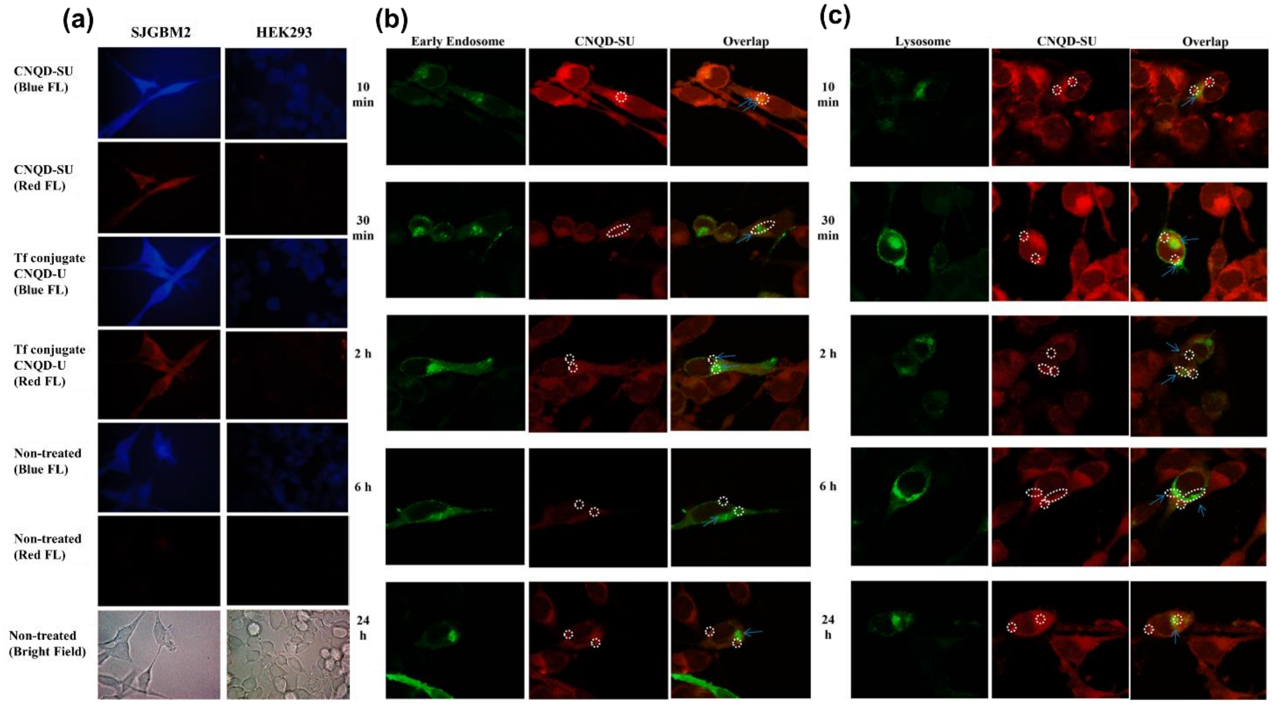

Fig. 27. (a) Images obtained using fluorescence microscopy of SJGBM2 and HEK293 cells after treatment with Tf-conjugated g-C_3N_4 QDs and g-C_3N_4 QDs -SU. The excitation wavelengths are 358 nm for blue and 558 nm for red. (b&c) Confocal microscopy time-lapse analysis of g-C_3N_4 QDs intracellular localization (into early endosomes and lysosomes). The g-C_3N_4 QDs were visualized using a red luminescence, while early endosome trackers are green fluorescent, and lysosome trackers are blue fluorescent. The regions of g-C_3N_4 QDs -SU with the highest intensity are denoted with white circles, while the lysosomes and endosomes are indicated with blue arrows. In each example, the overlap between the first two photos is indicated by the third column. Green light has a wavelength of 488 nm, while red light has a wavelength of 594 nm. Reproduced with permission from [234].

4.5.2.2. Two-photon fluorescence imaging

The use of two-photon fluorescence (TPF) imaging in studying living tissues has become increasingly popular since it enables monitoring of the tissues for extended periods of time without causing significant damage to them. TPF imaging offers advantages over traditional fluorescence optical and confocal imaging, including less phototoxicity, less photobleaching, and deeper tissue penetration. Researchers are particularly interested in metal-free semiconductor nanoprobes with high two-photon absorption cross-section in the NIR region, good biocompatibility, and high photostability. These properties make TPF imaging a promising tool for medical applications. There are few research reports available on the TPF imaging of g-C_3N_4 QDs. For example, Zhang et al. [53] developed a fluorescent probe, g-C_3N_4 single-layered QDs, showing promise as a safe and cost-effective option for the TPF imaging of cellular nuclei (**Fig. 28a**). The g-C_3N_4 single-layered QDs were successfully synthesized using a modified liquid exfoliation technique. These QDs had a size distribution ranging from 2 to 6 nm, with most particles located at approximately 4 nm. They exhibited stable and intense two-photon fluorescence, with a high two-photon absorption cross-section of 28000 GM at 750 nm. Due to their appropriate size distribution and specific interactions with chromatin, the g-C_3N_4 single-layered QDs may be considered as a viable and economical alternative to the commercial reagent DAPI for the TPF imaging of cellular nuclei. The as-synthesized g-C_3N_4 QDs possessed stable and strong two-photon absorption, good biocompatibility, non-toxicity, negligible photothermal effects, and excellent fluorescence imaging capabilities. Therefore, they have the potential to be utilized in various biological applications, including biomedicine and deep-tissue imaging. In another example, Wu et al. [123] tested the TPF imaging efficacy of three probes (CN, CN-DPT, and CN-THDT QDs) incubated with MCF-7 cells. The results of the fluorescence signal acquisition excited by an 800 nm NIR laser are shown in **Figs. 28b** and **28c**. Compared to the control without probes, all g-C_3N_4 QDs demonstrated TPI abilities for MCF-7 cells. Among the three g-C_3N_4 QDs, CN-DPT QDs exhibited the highest two-photon fluorescence intensity, while CN-THDT QDs produced the weakest signal. The decrease in two-photon fluorescence of CN-THDT QDs under the same excitation energy is consistent with their increased catalytic activity. Instead of TPI, one-photon fluorescence images of the three g-C_3N_4 QDs were obtained using TIRFM. All g-C_3N_4 QDs emit blue light when excited at 405 nm.

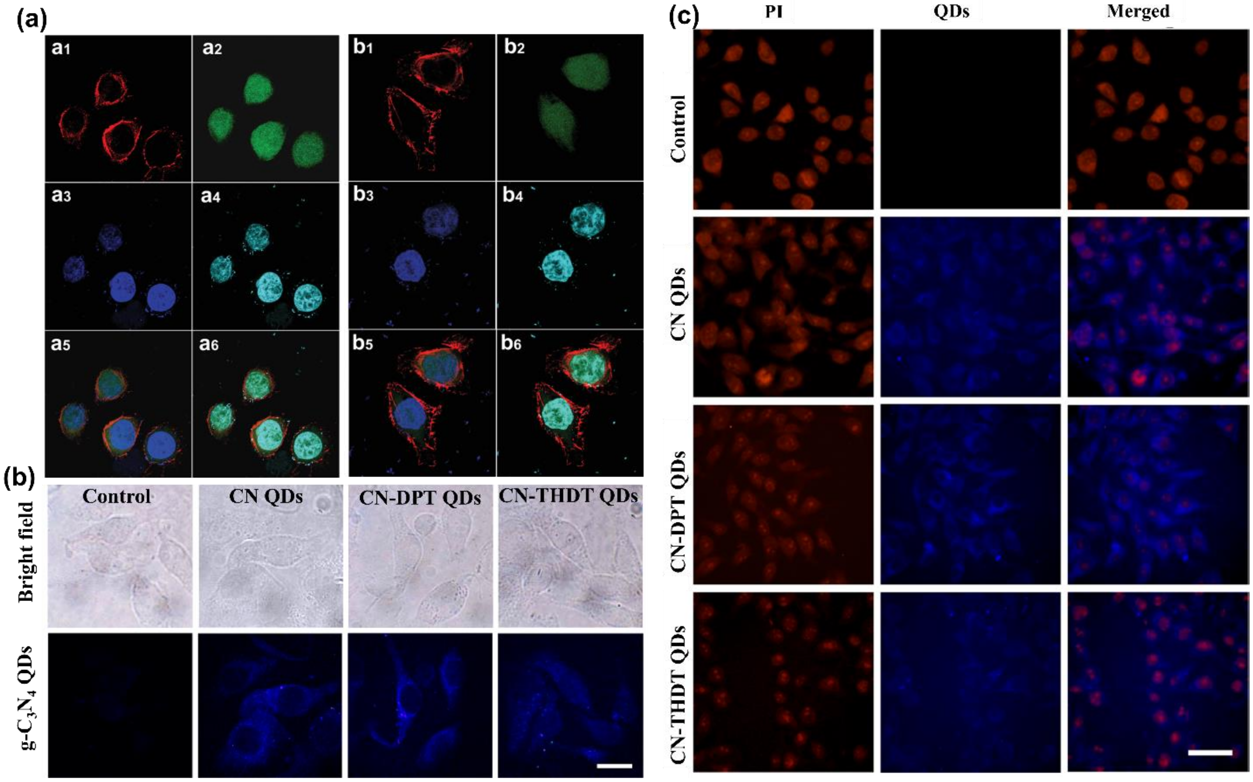

Fig. 28. (a) Fluorescence images of HepG2 cells co-stained with various dyes and g-C_3N_4 QDs. The following images were obtained using one-photon excitation: One-photon fluorescence images of HepG2 cells co-stained with 1,1-dioctadecyl-3,3,3,3-tetramethylindocarbocyanine perchlorate (Dil) are represented by (a1 and b1). Fluorescein diacetate (FDA) staining results in one-photon fluorescence images denoted by (a2 and b2). The g-C_3N_4 QDs produced one-photon fluorescence, represented by (a3). DAPI staining resulted in one-photon fluorescence images denoted by (b3). Additionally, two-photon fluorescence imaging was performed, resulting in the following images: Two-photon fluorescence images of HepG2 cells with g-C_3N_4 QDs are represented by (a4). DAPI staining produced two-photon fluorescence images denoted by (b4). Merged images were also created: Merged images of a1–a3 are represented by (a5). Merged images of a1, a2, and a4 are represented by (a6). Merged images of b1–b3 are represented by (b5). Merged images of b1, b2, and b4 are represented by (b6). Reproduced with permission from [53]. (b) MCF-7 cells were incubated with CN, CN-DPT, and CN-THDT QDs (1 µg/mL) for 4 hours, and two-photon fluorescence images were captured. A control group of MCF-7 cells without the three g-C_3N_4 QDs was also included. The g-C_3N_4 QDs were excited using an 800 nm wavelength, and the two-photon fluorescence images were recorded with emission wavelengths ranging from 400 to 500 nm. The scale bar in the images represents 20 µm. (c) MCF-7 cells were incubated with CN, CN-DPT, and CN-THDT QDs (1 µg/mL) for 4 hours, and their imaging was performed using total internal reflection fluorescence microscopy (TIRFM). A control group of MCF-7 cells without g-C_3N_4 QDs was included. To stain the nuclei, the MCF-7 cells were treated with PI (1 µg/mL) at room temperature. The emission spectrum of PI ranged from 550 to 660 nm, with an excitation wavelength of 543 nm. The three g-C_3N_4 QDs were excited using a wavelength of 405 nm, and the fluorescence images were recorded with emission wavelengths ranging from 430 to 490 nm. The scale bar in the images represents 50 µm. Reproduced with permission from [123].

4.5.2.3. *In Vivo* optical imaging

Over the past decade, GQDs and other semiconducting QDs have made great strides in *in vivo* bioimaging of model animals, resulting in a significant progress in biomedical applications [236–241]. A noteworthy aspect is that g-C_3N_4 QDs also exhibit both short- and long-wavelength PL. For *in vivo* bioimaging, the focus is mainly on the long-wavelength emission of GQDs, since the short-wavelength emission can overlap with the autofluorescence generated by living cells. In 2014, Wu et al. [78] studied the ability of phosphorous-doped g-C_3N_4 QDs to image tumors by *in vivo* Vision Systems®. Mice were injected with 5×10^6 OCM-1 cells subcutaneously one week prior to the experiment. A dose of 0.1 mg/mL P-g-C_3N_4 QDs was then intratumorally injected to the mice, and the results are shown in **Figs. 29a–c**. Fig. 29a illustrates a bright-field microphotograph of the tumor-bearing mice, while **Fig. 29b** displays the photoacoustic image of the tumor-bearing mice, incubated with P-g-C_3N_4 QDs. **Fig. 29c** represents the merged bright-field and photoacoustic image of the tumor-bearing mice, incubated with P-g-C_3N_4 QDs. Photoacoustic images of the mice were taken at 4, 12, and 24 h after intratumoral injection of P-g-C_3N_4 QDs (100 µL, 0.1 mg/mL). The material gradually diffused and discharged after 24 h of injection. This study demonstrated that P-g-C_3N_4 QDs, as fluorescence-responsive nanoconstructs, can enable real-time continuous imaging of their uptake into cells. P-g-C_3N_4 QDs exhibit high quantum yield, low biological toxicity, high stability, and a suitable emission wavelength, making them an efficient bio-imaging material. Furthermore, expanding the concepts for real-time *in vivo* tumor imaging will lead to the development of targeted cellular imaging and diagnostic applications.

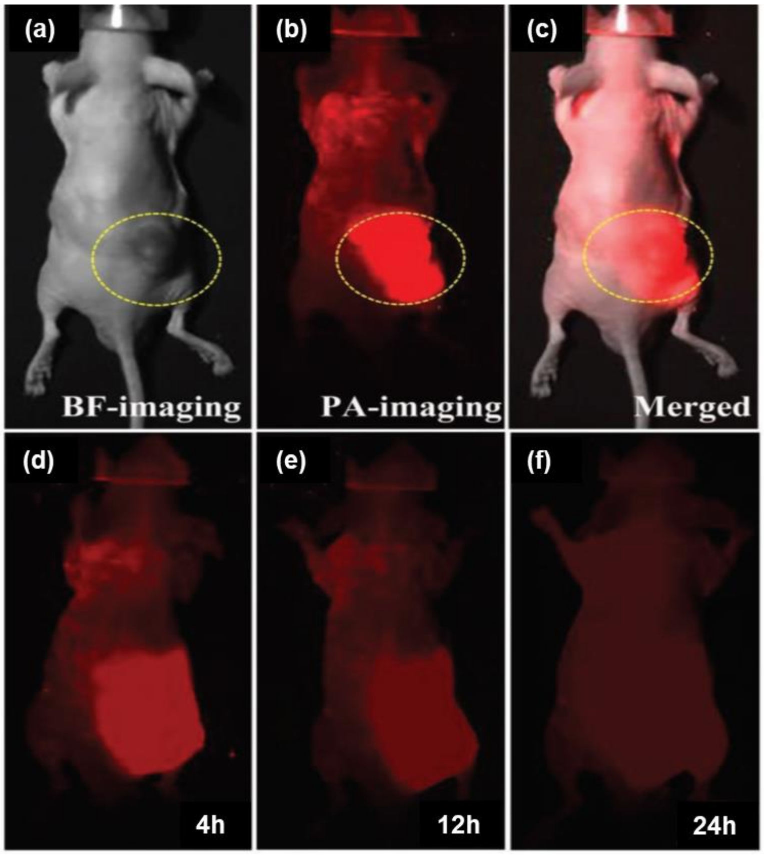

Fig. 29. (a) A bright-field microphotograph of the tumor that was found in the naked mouse. b) A photoacoustic image of a tumor-bearing mouse that has been incubated with P-g-C_3N_4 QDs. c) A bright-field image of a tumor-bearing mouse that has been incubated with P-g-C_3N_4 QDs along with a photoacoustic image. The exact spot of the tumor is denoted by the yellow circles. Photoacoustic pictures of animals at (d), 4, (e), 12, and (f) 24 hours following the intratumoral injection of P-g-C_3N_4 QDs (100 L, 0.1 mg mL1) in mice. Reproduced with permission from [78].

4.5.3. Therapeutics

g-C_3N_4 QDs possess unique properties that make them ideal for therapeutic applications. These properties include the presence of functional groups on the edges of g-C_3N_4 QDs, which allows them to be conjugated with targeting ligands and therapeutic agents. The sp^2-hybridized carbon in the g-C_3N_4 QDs structure enables therapeutic molecules, often containing triazine rings, to be efficiently bound to the basal planes of g-C_3N_4 QDs, increasing drug loading capacity and facilitating efficient drug release. Furthermore, g-C_3N_4 QDs can enhance the generation of ROS when exposed to irradiation, making them valuable in photothermal and photodynamic therapy (PDT). In this section, a few examples of cancer treatments, involving the use of g-C_3N_4 QDs are provided. Specifically, chemotherapy with responsive drug release and phototherapy with external light irradiation are discussed. **Fig. 30** provides an illustration of how g-C_3N_4 QDs are used in various therapeutic applications.

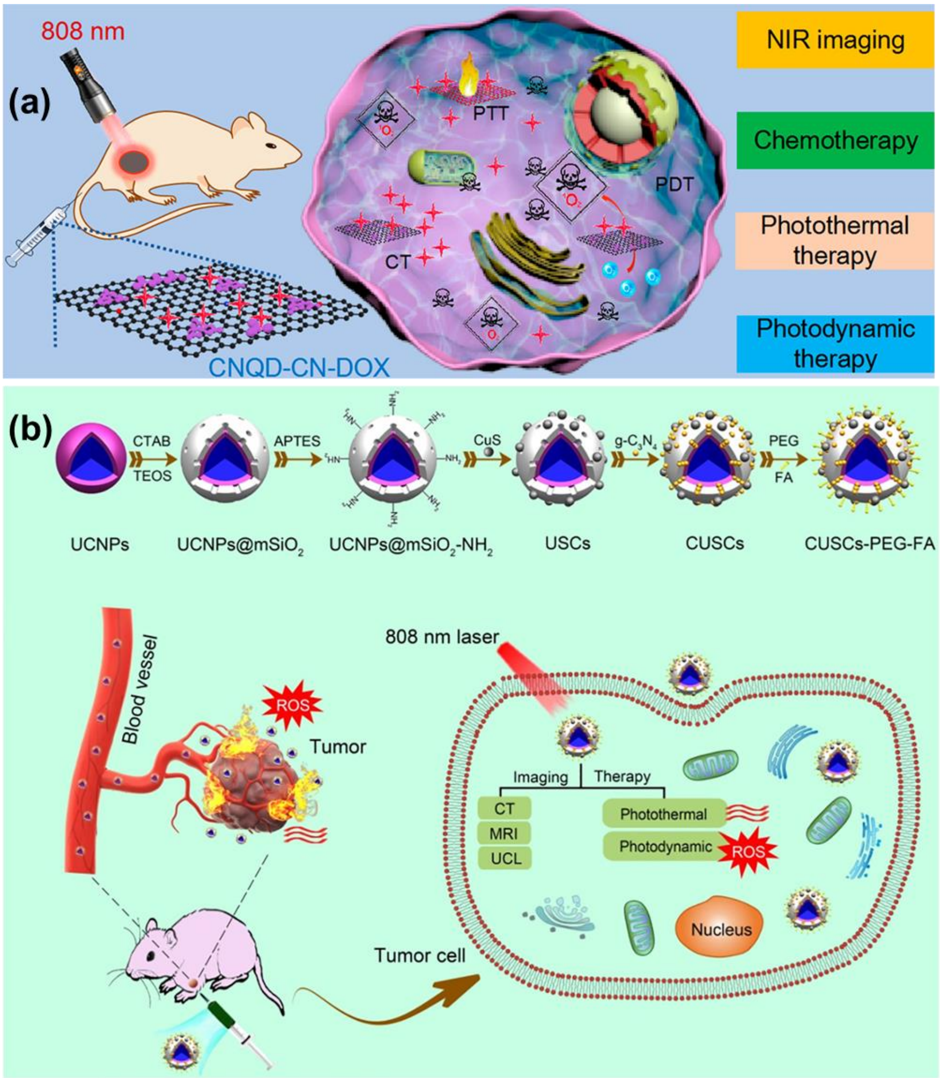

Fig. 30. (a) Schematic illustration of CNQD-CN for bioimaging, drug delivery and therapy of cancer. Reproduced with permission from [70]. (b) A diagram of the synthesis of CUSCs-PEG-FA (g-C_3N_4 QDs/polymer nanocomposite) and its application for multimodal imaging and therapy of cancer. Reproduced with permission from [228].

4.5.3.1. Responsive drug delivery

The distinctive structure of g-C_3N_4 QDs, characterized by a high surface area, abundant conjugate structures, and excellent biocompatibility, makes them a promising candidate for potential drug delivery systems. Although there are only a few examples of g-C_3N_4 QD based nanocarriers for controlled drug release and therapeutic applications, they show great potential. For example, Liu et al. [70] developed a metal-free, multifunctional platform called CNQD-CN, consisting of g-C_3N_4 QDs embedded in carbon nanosheets. This platform was used for NIR imaging-guided combined photo-chemotherapy, as shown in **Fig. 30a**. CNQD-CN was synthesized *in situ* using formamide as a single source, without any additional catalysts or other molecule precursors. CNQD-CN acts as a NIR/pH dual-responsive drug carrier to increase the effectiveness of chemotherapy. The effectiveness of CNQD-CN as a drug delivery system for the anticancer drug doxorubicin (DOX) was examined. As shown in **Fig. 31**, DOX was efficiently loaded onto CNQD-CN, with a loading capacity of up to 53%. The release of DOX was found to be responsive to changes in pH, with greater release observed at lower pH values (**Figs. 31a-c**). Acid-induced dissociation of hydrophilic groups and photothermal conversion of the CNQD-CN decrease the electrostatic/hydrogen bond interactions between the DOX and CNQD-CN, thereby increasing the DOX release rate. *In vitro* studies showed that the combination of DOX-loaded CNQD-CN with NIR irradiation at 808 nm resulted in a high level of cell death. This demonstrates the potential of CNQD-CN as a therapeutic platform (**Fig. 31d-f**). In another example, Dong et al. [147] fabricated g-C_3N_4 QDs with polyethylene glycol, a promising carrier for delivering DOX due to its non-toxic and biocompatible properties. Moreover, its pH-sensitive release profile makes it a suitable choice for drug delivery. The inclusion of g-C_3N_4 QDs in a poly(ethylene glycol (PEG) matrix prevents any noticeable π-π stacking in the g-C_3N_4 QDs-PEG-DOX system, allowing for a higher quantity of DOX to be released compared to a previously developed drug delivery system based on GQDs, operating at the same pH. Additionally, the intrinsic fluorescence properties of g-C_3N_4 QDs-PEG and DOX help in the effective monitoring and confirmation of the controlled release of the drug, eliminating the need for external dyes. The same research group claim that g-C_3N_4 QDs synthesized by the hydrothermal methods are suitable carriers for DOX delivery, since they are both biocompatible with the body and has no toxic effects[242]. These g-C_3N_4 QDs have a preferred pH-sensitive release profile and highly efficient DOX loading (69.8%). DOX is released quickly under acidic conditions, such as those found in tumor cells, which reduces the adverse effects of anticancer agents on normal tissues and enhances their therapeutic efficiency. These g-C_3N_4 QDs are inherently fluorescent, making it easy to monitor their real-time movement in cells without external dyes.

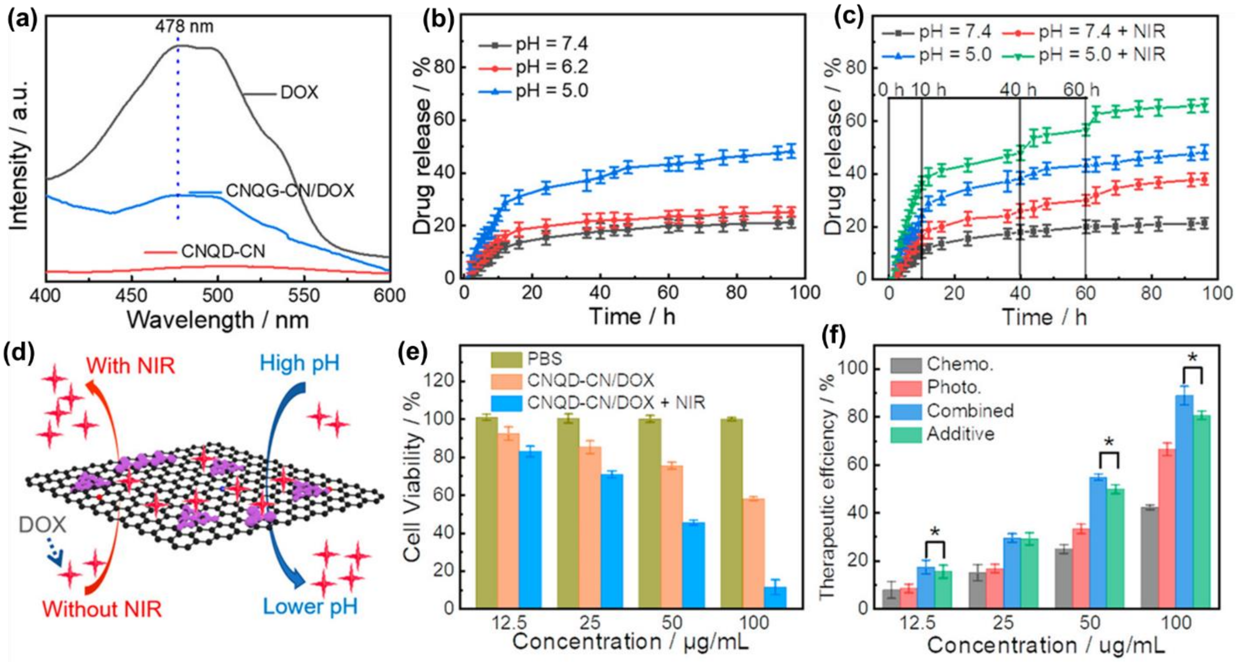

Fig. 31. (a) Typical absorption bands for DOX, CNQD-CN, and CNQD-CN/DOX in the UV-VIS range. (b) The amount of DOX released by CNQD-CN/DOX at different pH levels. (c) Release of DOX from CNQD-CN/DOX with or without 808 nm light. (d) Schematic illustration shows how DOX is released from CNQD-CN when the pH and NIR light are changed. (e) The number of HeLa cells that are still alive after being treated with CNQD-CN/DOX with or without 808 nm light. (f) Therapeutic effectiveness of CNQD-CN based nanocarrier for chemotherapy, phototherapy, and combined therapy. Two-tailed, homoscedastic Student's t-test was performed to determine statistical significance (n = 4, $^*p < 0.05$). Irradiation at 808 nm has a power density of 1.0 W/cm^2 and a duration of 5 minutes. Reproduced with permission from [70].

4.5.3.2. Photothermal and photodynamic therapy

g-C_3N_4 QDs are a new type of photothermal and photodynamic therapy (PTT and PDT) agents with several advantages that include excellent biocompatibility and dispersibility, ability to absorb light, high photostability, quick removal from the body, and easy breakdown by enzymes. Liu et al. [70] determined the photothermal characteristics of g-C_3N_4 QDs embedded in carbon nanosheets (CNQD-CN) (**Fig. 32a**). Upon exposure to 808 nm irradiation, a slight temperature increase of 3.1 °C was observed in pure water. However, in CNQD-CN dispersions with concentrations of 25, 50, and 100 µg/mL, the temperature rose by 8.9, 16.5, or 22.2 °C, respectively (**Figs. 32b** and **32c**). The photothermal conversion efficiency of CNQD-CN was determined to be approximately 21.32%, based on calculated results and previous measurements. This efficiency was comparatively lower than that of carbon dots (38.5%) [243], GQDs (33.45%) [244], antimonene QDs (45.5%)/nanosheets (41.8%) [245,246], and boron nanosheets (42.5%) [247]. This was attributed to the relatively lower proportion of CN in CNQD-CN and the limitations of the triazine structure for efficient photothermal conversion. Furthermore, the photothermal stability of CNQD-CN was excellent, as evidenced by no significant change in temperature over five cycles. The presence of the tris-triazine ring in CNQD-CN suggests its potential for effective photodynamic therapy, as it demonstrates excellent singlet oxygen conversion capability. NIR-induced phototherapy of CNQD-CN was conducted using HeLa cells (**Fig. 32d**). In **Fig. 32f**, it can be observed that when subjected to different concentrations of CNQD-CN without 808 nm irradiation, over 95% of the HeLa cells remained viable. With prolonged NIR irradiation, the absorbance intensity at 417 nm of the 1,3-Diphenylisobenzonfuran (DPBF) suspension containing CNQD-CN exhibited a linear reduction (**Fig. 32e**). This decrease indicates the degradation of DPBF and generation of singlet oxygen ($^1O_2$) by CNQD-CN. When testing with the NIR laser irradiation alone, no dead cells were observed in the control sample. However, when CNQD-CN was used, there was a higher number of dead cells after the NIR laser irradiation (**Figs. 32g-j**). This suggests that CNQD-CN has potential for photoinduced cancer treatment. The observed cell death is due to a combination of PTT and PDT, with approximately 82.5% attributed to PDT and 17.5% to PTT [70].

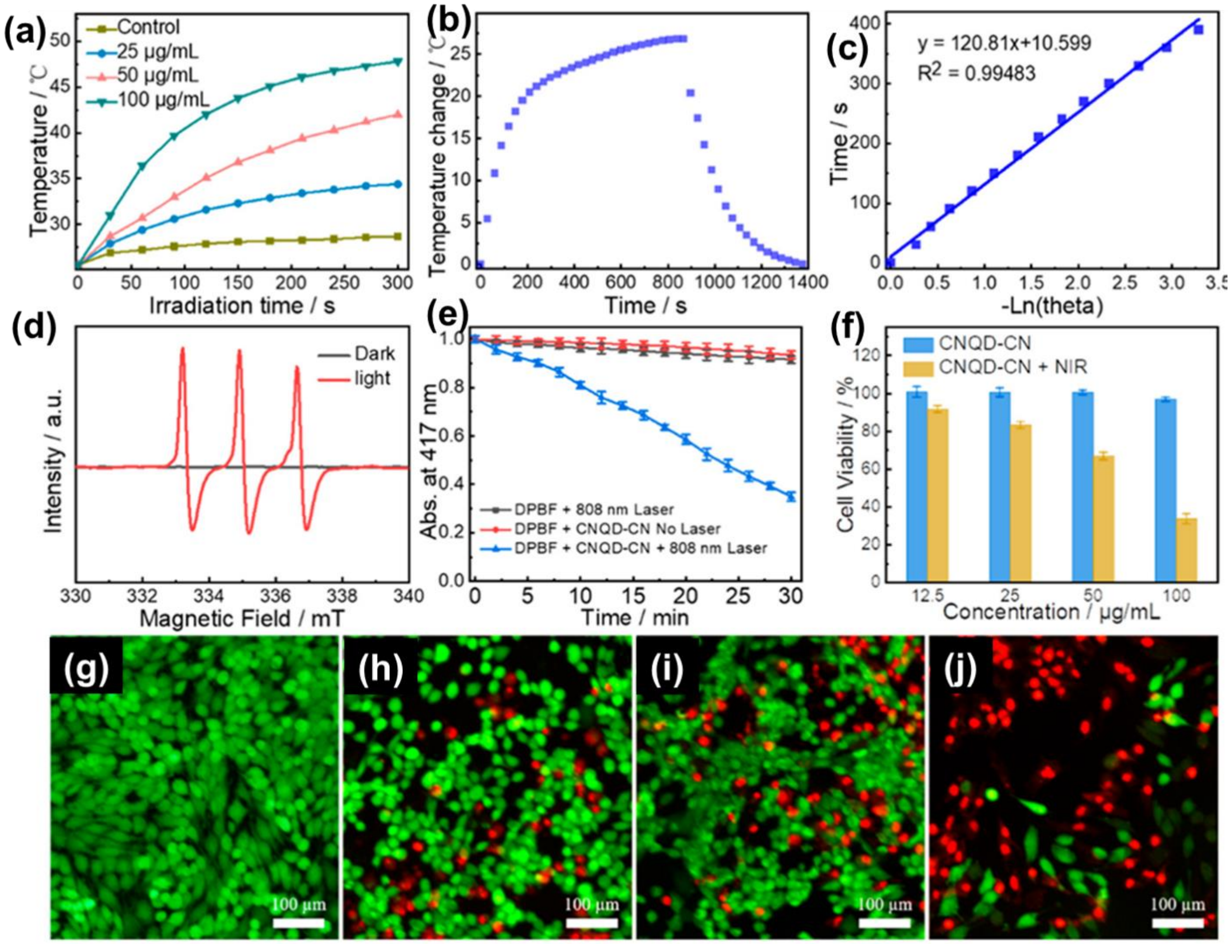

Fig. 32. PTT/ PDT properties. (a) Temperature curves of water with different amounts of CNQD-CN (zero is the control) when exposed to 808 nm light. (b) Curves showing how the temperature of a 100 g/mL CNQD-CN solution goes up and down when it is exposed to 808 nm light. The decreasing temperature graph (b), (c) shows the linear time constant *versus*-Ln θ. (d) ESR signs of $^1O_2$ of CNQD-CN for 8 minutes, with or without NIR irradiation. (e) Plots of the relative strength of CNQD-CN in a DPBF solution at different times of irradiation. (f) Cell viability tests of HeLa cells exposed to 808 nm light while treated with CNQD-CN for 300 seconds. Confocal imaging of HeLa cells incubated with CNQDCN at different doses (0, 25, 50, and 100 g mL^{-1}) for 300 s under 808 nm light. The power of light at 808 nm is 1.0 W/cm^2. Reproduced with permission from [70].

Recently, the CNQD-CN-based nanoplatform was evaluated for its potential use in bioimaging and cancer treatment. Mice with subcutaneous HeLa cervical carcinoma were injected with either phosphate buffer saline, CNQD-CN, or CNQD-CN/DOX. After one day, the tumors were treated with or without 808 nm irradiation twice every other day (**Figs. 33a** and **33b**). Mice injected with CNQD-CN and CNQD-CN/DOX exhibited bright NIR fluorescence in the tumor tissue, indicating potential for NIR imaging-guided cancer treatment. Negligible fluorescence signals were observed in other organs. Treatment with DOX loading alone or 808 nm irradiation alone resulted in efficient reduction in tumor volume. As demonstrated in **Fig. 33c**, when mice treated with CNQD-CN/DOX were subjected to 808 nm irradiation, tumor growth was significantly inhibited, indicating a synergistic effect of phototherapy and chemotherapy. The body weight of the mice remained within a reasonable range throughout the treatment period, with no significant observed weight loss. Tumor cells in the CNQD-CN/DOX plus NIR group exhibited severe damage, indicating the combined effect of cancer therapy (**Figs. 33e** and **33f**). Next, the effectiveness of CNQD-CN nanoplatform for bioimaging and cancer treatment on mice with cervical carcinoma was evaluated. Upon injection, the nanoplatform was found to collect at tumor sites, which proves its potential for NIR imaging-guided cancer treatment (**Figs. 33g-i**). Treatment with DOX loading or 808 nm irradiation alone resulted in significant reduction in the tumor volume; however, a combination of both showed a synergistic effect. The combination treatment caused severe damage to tumor cells, while not affecting the weight of the mice. Xu et al. [228] conducted *in vivo* experiments using U14 tumor-bearing mice to evaluate the tumor-suppressive effect of g-C_3N_4 QDs encapsulated CUSCs-PEG-FA nanocomposite. As shown in **Fig. 33m**, direct exposure to the laser alone resulted in a slight inhibition of tumor growth. Mice injected with CUSs or USCs and exposed to 808 nm NIR laser exhibited partial tumor inhibition with USCs displaying higher efficiency. However, the group treated with CUSCs-PEG-FA under 808 nm NIR laser exhibited the slowest tumor growth rate. These findings align with the results obtained from cytotoxicity assays and dye experiments performed on HeLa cells. After a 14-day treatment period, the typical organs and tumor tissues from each group of U14 tumor-bearing mice were dissected. The masses of the excised tumors are presented in **Fig. 33n**, while digital photographs of the mice and their corresponding tumor tissues are shown in **Fig. 33o**. The tumor tissues were further stained with hematoxylin and eosin (H&E), and the stained images are presented in **Fig. 33p**. These images clearly illustrate that tumor cells in the group with the most optimal inhibition were largely destroyed, whereas cells in the control group remained largely intact. Moreover, H&E-stained images of the major organs in the various treatment groups demonstrate that CUSCs-PEG-FA exhibited minimal acute toxicity to mice. These observations supporting the potential of g-C_3N_4 QDs for clinical use in disease treatment [228].

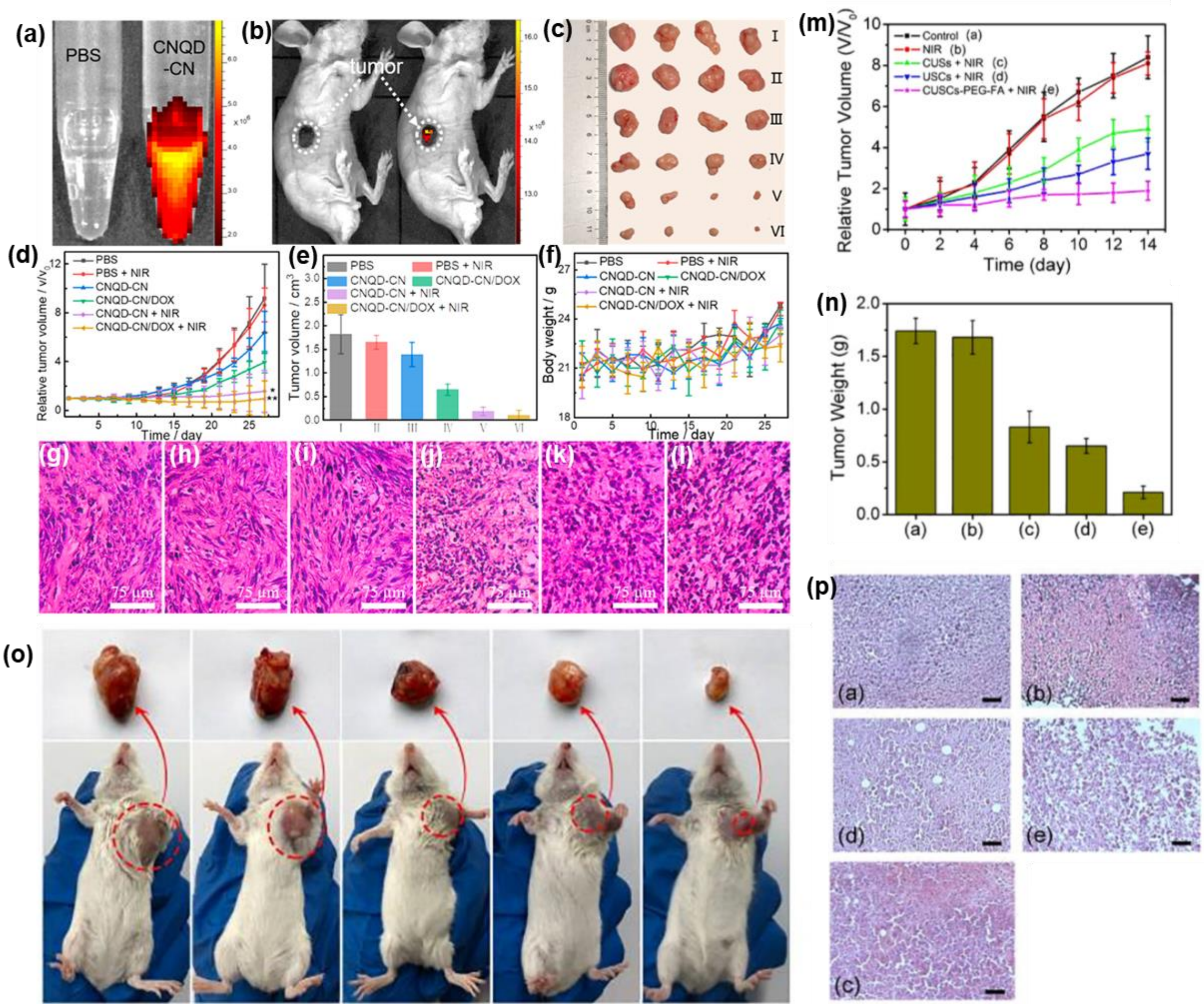

Fig. 33. *In-Vivo* synergistic therapy. (a) Optical and near-infrared (NIR) scans of CNQD-CN solution. (b) Optical and near-infrared (NIR) photographs of a CNQD-CN-treated mouse. Tumor images captured optically from mice undergoing various treatments. (d and e) Tumor volumes and relative growth curves from mice of varying treatment conditions. (f) Mice weight-growth curves under various experimental circumstances. (g-i) A sample of H&E-stained tumor slices from mice with various treatments. Two-tailed homoscedastic Student's t-test was employed for statistical analysis (n = 4, *p < 0.05, **p < 0.01). Power of irradiation = 1.0 W/cm^2; duration of irradiation = 5.0 minutes. Reproduced with permission from [70]. (m) The relative size of tumors in mice with tumors in different groups that were given different treatments. (n) The total weight of tumor tissue removed from tumor-bearing mice in each of the four treatment groups fourteen days following the end of the experiment. (o) Images of tumors on mice that have been treated for their tumors, as well as digital photographs of a variety of mice that have been diagnosed with tumors. (p) H&E-stained pictures were obtained from the various groups after a treatment period of fourteen days. All of the photographs include scale bars that are 50 micrometers wide. Reproduced with permission from [228].

5. Current and future research status for the g-C_3N_4 QDs synthesis and applications

Recent advances in g-C_3N_4 QDs have completely reimagined the promise of these materials as platforms for optoelectronics, sensing, photocatalysis, and biological applications. Researchers have investigated unique synthetic approaches to doping and altering the precursors of g-C_3N_4 QDs, which has led to considerable advances in the properties of these QDs, particularly in the areas of optoelectronics, photocatalysis, and biological dimensions. Because of these improvements, the application of g-C_3N_4 QDs in a variety of medical sectors is now more feasible. In order to maximize the physicochemical features of g-C_3N_4 QDs and customize them to the requirements of certain applications, a number of different experimental approaches have been established. In addition, a significant amount of effort has been put toward the development of risk-free and uncomplicated "one-pot" synthesis techniques. These procedures make use of precursor molecules that are easily obtainable as well as easy apparatus, such as a microwave. Because of these accomplishments, g-C_3N_4 QDs are now more accessible and suitable for use in a wider variety of applications, from optoelectronics to nanomedicine. Because a low-cost, industrial-scale synthesis of g-C_3N_4 QDs has not yet been truly realized, many applications of g-C_3N_4 QDs are now not practically feasible. This is the case for a number of reasons. However, our research has led us to the conclusion that it will be able to produce g-C_3N_4 QDs on a ton-scale either through top-down or bottom-up methods. This is similar to the existing capacity for the mass manufacturing of graphene materials. Scalability is required not just for the synthesis but also for the purification step. For purification on a benchtop, ultrafiltration can be utilized since it is a faster procedure than other frequently employed purification methods such as centrifugation, dialysis, and electrophoresis.

In the preceding sections, a comprehensive examination and analysis of various facets of each synthesis route and field of application were conducted and highlighted. Furthermore, the characteristics of each examined g-C_3N_4 QDs based materials, among others, are analyzed in a suitable manner based on the preparation strategy and application. Numerous authors have exerted significant efforts towards yielding g-C_3N_4 QDs using top-down and bottom-up pathways and have deliberated on the QDs formation mechanism and its significance in relation to the selected application. The inquiry regarding the viability and the enhancement of g-C_3N_4 QDs properties going from 2D to 0D morphology remains a persistent and imperative topic of discussion. A comprehensive critical approach was employed to conduct a secondary screening of the aforementioned works, with a focus on categorizing them based on the synthesis strategy and field of application.

In the realm g-C_3N_4 QDs synthesis, it is evident that both top-down and bottom-up approaches possess a certain allure, each adorned with their own unique set of virtues and drawbacks. In regard to cost, the microwave-assisted solvothermal method and solid phase method reign supreme from an economic standpoint. These methods, with their minimal equipment requirements and effortlessly swift synthesis, are truly a testament to simplicity and refinement. Nevertheless, the stoichiometry and bond configurations of the obtained QDs derived from the two bottom-up techniques may diverge from the bulk g-C_3N_4. Regarding the one-step sonication method and one-step hydrothermal method, while they do possess the advantage of being effortless procedures and requiring affordable equipment, the prolonged synthesis cycle inevitably amplifies the electricity consumption, thereby augmenting the overall expenditure, especially when combined with oxidation pretreatments to achieve an elevated yield, thus, the grandeur of g-C_3N_4 QDs production cost is magnificently amplified. The Quasi-CVD method, with its unparalleled demand for top-of-the-line equipment, substantial energy consumption, and regrettably low yield, undoubtedly reigns as the epitome of opulence among the aforementioned methods. Nevertheless, this exquisite technique has the ability to generate fascinating composite materials, adorned with impeccable contact between the g-C_3N_4 QDs and the used substrate, all achieved effortlessly in a single step. Furthermore, it is worth noting that g-C_3N_4 QDs, meticulously crafted through various exquisite methods, are likely to exhibit distinct structural characteristics and surface chemistry. These include the attributes of average diameters, surface functionalities, element compositions, and even the presence of defective structures. Such intricacies, in turn, bestow upon the as-prepared g-C_3N_4 QDs their own unique electronic structures and optical properties, rendering them as distinct entities that perform in different manners in practical applications. An example of this may be seen in the g-C_3N_4 QDs synthesized by the hydrothermal technique, which have a notable emission of blue light and distinctive up conversion photoluminescence characteristics. The aforementioned features have the potential to serve as spectrum converters in photocatalytic systems. Furthermore, the simultaneous synthesis of g-C_3N_4 QDs and doped g-C_3N_4 QDs may be achieved via a microwave-assisted solvothermal technique, by carefully choosing appropriate precursors. The obtained g-C_3N_4 QDs exhibit favorable dispersibility and robust fluorescence properties when immersed in water, hence indicating promising prospects for its use in bioimaging as well as the detection of ions in aqueous mediums. Moreover, in contrast to the bottom-up approach, the top-down technique often has poor, hence, the g-C_3N_4 QDs synthesized by the top-down approach are often integrated with other substances to form composites that serve as photoelectrocatalysts, fuel cell electrodes, and similar applications. Conversely, the g-C_3N_4 QDs produced through the bottom-up technique are mostly used in biosensing, biological imaging, and related fields. Herein, a comparative table describing the merits and demerits of each top-down and bottom-up synthesis approaches (**Table 1**).

Table 1: Comparison of the merits and demerits of different g-C_3N_4 QDs synthesis approaches

Synthesis pathway	Technique	Advantages	Disadvantages	Ref.
Top-Down	Ultrasonication	Facile steps and straightforward procedure	Poor yield and time-consuming synthesis sequences	[86,87,90,96,122,139,144,176]
	Ultrasonication combined with chemical oxidation	Acceptable yield with good product purity	Elevated cost and strenuous synthesis steps with the utilization of strong acids (Poor scalability)	[53,93,95]
	Hydrothermal	One step and low cost	Poor yield and time-consuming synthesis cycles	[72–75,77,78,80,81,83,84]
	Hydrothermal associated with chemical oxidation	Good yield and high purity	High cost and strong acids' usage (poor scalability)	[47,76,79,82]
Bottom-Up	Solid-phase	Single step, High production yield, high quantum yield, and adjustable PL properties depending on the precursors (highly scalable)	Tedious and time-consuming post-synthesis purification process	[69,110–117,248]
	MW-assisted hydro-/solvothermal	simple synthesis stages, short synthesis cycle and low cost	Poor quantum yield	[97–99,103–108]
	CVD	Totally intertwined in the process of making g-C3N4 QDs composites	High energy consumption and further separation and purification processes are needed	[60,65]

As stated before, several straightforward, inexpensive, and size-accommodating techniques have been created for producing g-C_3N_4 QDs with various physicochemical characteristics. These techniques are divided into top-down and bottom-up synthetic methodologies, which are both of the main production approaches. On one hand, the bottom-up approach uses solid-phase, CVD and MW-assisted techniques. On the other hand, the top-down approach largely uses the hydrothermal, ultrasonication and evaporation-condensation/hydrolysis strategies. These techniques produce g-C_3N_4 QDs that effectively absorb light and have unique Up conversion PL and adjustable PL. Because of their superior optical qualities, g-C_3N_4 QDs are capable of using photons across a broad wavelength range (from UV to IR). Consequently, in the photocatalytic processes, g-C_3N_4 QDs serve as a material with multiple purposes. For instance, they may be used as a photosensitizer in conjunction with a wide-bandgap semiconductor to significantly increase photon usage during photocatalysis operations. Additionally, it may be used as a converter to expand the photocatalyst's spectrum usage to the NIR region. Interestingly, g-C_3N_4 QDs have the capacity to avoid photocorrosion in photoelectrocatalytic processes because of their high stability. Despite the field's impressive advancements, there are still a number of problems that need attention. There are yet no reports for synthesizing g-C_3N_4 QDs on a big scale. The solid phase strategy seems to be the most likely of the many ways that could be scaled up, however the productivity of the approach has yet to be enhanced to shorten the post-treatment time e.g. dialysis, and to optimize the controlled size synthesis procedure. Therefore, it is vital to make efforts toward the mass manufacture of excellent quality, uniformly sized g-C_3N_4 QDs. Moreover, while g-C_3N_4 QDs defects have a significant impact on their optical and electrical characteristics, there are currently no methods for correctly engineering the quantity of defects in these 0D materials. So, it is important to focus more on the well-planned structural synthesis of g-C_3N_4 QDs. In addition, surface modifications/doping/chemical functionalization on g-C_3N_4 QDs surface have the potential to impact both their electronic and photocatalytic characteristics, although there haven't been many investigations on this topic. For instance, several studies showed that doping g-C_3N_4 QDs with heteroatoms like S, P, F, B, and others might enhance their optical traits, but it is uncertain if doping would affect their photocatalytic activities. Additionally, it is possible for the features of g-C_3N_4 QDs to undergo modifications as a result of variations in the nature and quantity of surface functional groups and defects. Therefore, there is an urgent requirement for facile and manageable functionalization and doping strategies for g-C_3N_4 QDs to achieve enhanced photoluminescence modulation and increased efficacy, thereby rendering them highly attractive for a wide range of potential applications. For this reason, Additional theoretical and experimental investigations are required to comprehend the mechanisms underlying the features associated with g-C_3N_4 QDs, in order to fully exploit their distinct characteristics. Theoretical computations pertaining to the defects' effects, surface moieties, and doping on the band structure and photocatalytic characteristics of g-C_3N_4 QDs are advantageous in achieving their deliberate production with superior performance. The modeling of g-C_3N_4 QDs based composites is imperative for gaining a deeper comprehension of their role in both the photocatalytic and reaction processes. This includes an examination of the distribution of electrons in g-C_3N_4 QDs composites prior to and subsequent to photo-activation. The integration of computational analysis with empirical findings can facilitate a deeper understanding of the mechanisms underlying photocatalytic activation. Considering the favorable photocatalytic properties exhibited by composite photocatalysts based on g-C_3N_4 QDs in the degradation of organic pollutants in aqueous solutions, it is plausible to extend their application to the remediation of air pollutants such as volatile organic compound e.g. H_2S, NO_x, and so on, which represent a significant environmental challenge globally. Regrettably, there is a scarcity of literature on the subject of the use of g-C_3N_4 QDs for highly desirable photocatalytic reactions including H_2 evolution, O_2 evolution and CO2 reduction. Therefore, it is imperative to allocate additional resources towards the utilization of composite photocatalysts based on g-C_3N_4QD for these aforementioned purposes.

Jumping to the sensing application, till now, g-C_3N_4 QDs have demonstrated significant promise for sensing fields, including environmental sensing and biosensing, which is mainly to their distinctive physiochemical, morphological, electrical, and optical properties. This makes them a highly promising candidate among the various carbon nitride morphologies currently available. g-C_3N_4 QDs also presents prospects for the development of novel and practical nanocomposites, which can offer additional benefits through attachment or binding to active probes or targets of interest in a synergistic way. Nevertheless, there exist certain limitations that could be further improved in subsequent endeavors. Hence, there is a necessity to enhance the detection limit of g-C_3N_4 QDs based sensors to match the performance of high-performance liquid chromatography and fluorometry. This can be achieved by integrating g-C_3N_4 QDs with high-catalytically active nanomaterials and enzymes to fabricate devices with superior specific catalytic activity. Furthermore, the employment of noble metal/g-C_3N_4 based devices is restricted due to their elevated expenses, which hinders their extensive adoption. It is imperative to devise cost-effective measures, including the promotion of disposable electrodes such as biobased or paper-based electrodes, as a substitute for traditional glass-like carbon electrodes, and metal electrodes. Therefore, it is essential to establish low-cost and scalable methodologies for the large-scale production of g-C_3N_4 QDs based sensors.

With respect to the biomedical and optoelectronic fields, g-C_3N_4 QDs have a disadvantage when it comes to bioimaging, display, and fluorescence-based sensing due to their low photoluminescence quantum yield (PLQY) compared to carbon dots or GQDs, semiconductor QDs, and organic dyes. However, it is possible to improve the PLQY by removing or passivating chemical groups that act as nonradiative recombination centers and introducing heteroatom doping and chromophore groups. Some g-C_3N_4 QDs have already achieved PLQY values exceeding 40%, which is sufficient for most bioimaging purposes. Although g-C_3N_4 QDs may not match the brightness of certain competing materials due to their small size, they offer many other advantages that make them suitable for numerous unique applications. Also, a better understanding of the unique properties of g-C_3N_4 QDs with PL characteristics is necessary.

The potential applications of g-C_3N_4 QDs continue to expand, and they are increasingly being used in catalytic processes for chemical synthesis and conversion. Their excellent dispersibility, PLQY, and properties such as photoluminescence and semiconductivity make them suitable for the fabrication of flexible electronics and semiconductors. Although there are only limited reports on the use of g-C_3N_4 QDs as an active layer in LED fabrication and solar cell applications, they show promise in these areas. As a result of their one-of-a-kind features, g-C_3N_4 QDs can also be beneficial for fabricating flexible electronics. They are capable of enhancing and modifying the properties of other functional nanomaterials, which paves the way for the development of advanced material engineering. The great dispersibility and inherent amphiphilic characteristics of g-C_3N_4 QDs make them an attractive candidate for a new class of surfactants, which could have a wide range of applications in the future.

A wide variety of parameters, including size, chemical groups, dopants, edge configurations, and shape, all play a role in determining the properties of g-C_3N_4 QDs. However, without precise control over the composition and morphology of the g-C_3N_4 QDs, it is difficult to identify the individual influence of each of these elements through experimentation. Theoretical investigations have the potential to provide insightful information regarding these aspects, such as the coexistence of electron-donating and electron-withdrawing chemical groups as well as various heteroatom dopants. It is essential to investigate these interactions because they may lead to the identification of previously unknown qualities and possibilities for the use of g-C_3N_4 QDs in practical settings. In addition, the creation of heterojunctions between g-C_3N_4 QDs and other nanomaterials has not been adequately researched despite the fact that it offers a significant amount of potential. Since chirality can be introduced through the edge-functionalization of chiral molecules, there is no work that investigates how the properties of g-C_3N_4 QDs are affected by how they are distorted.

Despite the promising potential of g-C_3N_4 QDs, there are several challenges that need to be addressed before their clinical applications can be realized. One major challenge is that most of the currently reported g-C_3N_4 QDs exhibit low-wavelength fluorescent emission, typically in the blue to green spectrum range (400 to 550 nm). However, longer excitation and emission wavelengths are still needed more research to minimize interference from natural fluorescence in cells and tissues, particularly in the near-infrared (NIR) region. In order to improve bioimaging and phototherapy in deep tissues penetration in living organisms, especially in the near-infrared (>850 nm), it is important to change the emission wavelength and optical absorbance of g-C_3N_4 QDs. This means moving the emission from the UV to the visible region, and ultimately to the NIR region. With this change, g-C_3N_4 QDs can work better in medical applications and be more compatible with biological systems. The inherent optical and electronic features of g-C_3N_4 QDs allow for concurrent monitoring of therapeutic delivery, as well as regulated release through the interaction between g-C_3N_4 QDs and incident light. In addition, the drug loading capacity of g-C_3N_4 QDs is superior to that of other drug delivery systems. The potential applications of g-C_3N_4 QDs as platforms for biological imaging, sensing, and therapy are extremely diverse and extensive. Even if short-term toxicity testing *in vitro* is not nearly sufficient to support g-C_3N_4 QDs as safe in biological systems, first findings of minimal *in vivo* toxicity and low residual accumulation in mice models are encouraging. This is because these reports show that g-C_3N_4 QDs are not harmful to living organisms. In the realm of biological research, toxicity studies that are both more comprehensive and longer in duration will provide more insight on the distinctive characteristics of g-C_3N_4 QDs. Overall, the utilization of g-C_3N_4 QDs in biomedical uses, particularly in the areas of bioimaging and cancer treatment, is currently in its nascent stages. Presently underway advancements in g-C_3N_4 QDs are anticipated to broaden the biomedical potential of g-C_3N_4 QDs in non-invasive diagnosis and imaging-guided combined therapy. Based on these critical statements, herein, we propose the possible scenarios for future development of g-C_3N_4 QDs synthesis strategies with future insights on the use of these materials in high end fields (**Fig. 34**).

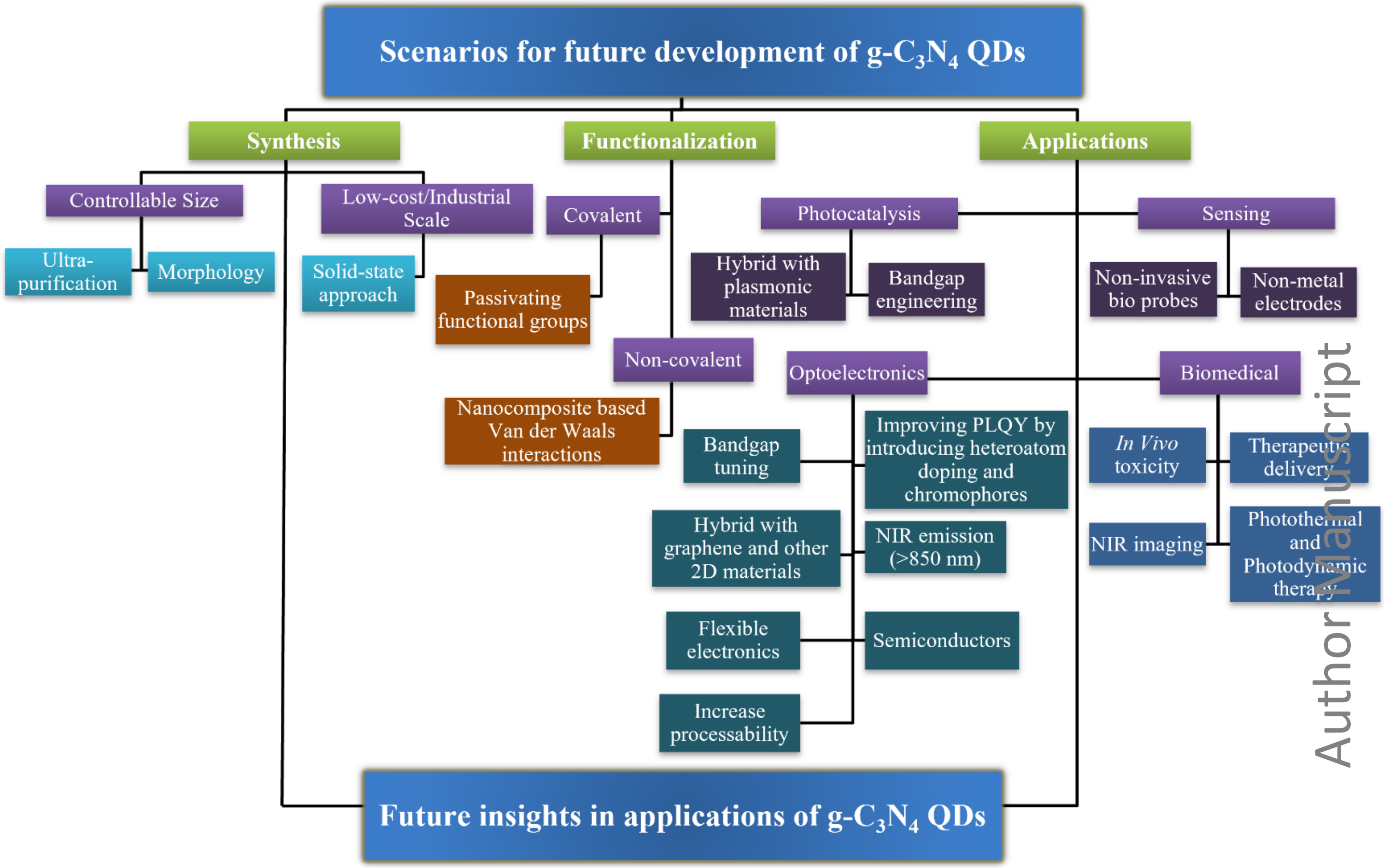

Fig. 34. Scenarios for future development of g-C_3N_4 QDs and future insights of their applications.

6. Summary

In summary, we have explored the synthesis, characterization, and properties of graphitic carbon nitride quantum dots (g-C_3N_4 QDs) in detail, and provided a survey on their applications from photocatalysis, sensing, optoelectronics, biomedical, etc. Overall, research on g-C_3N_4 QDs is in its early stages but has significant potential if the existing obstacles can be overcome and desirable properties can be achieved for g-C_3N_4 QDs for their effective use. Different production approaches have been explored for g-C_3N_4 QDs, each yielding nanomaterials with distinct characteristics such as water solubility, optical absorbance, photoluminescence, and conductivity, among others. Since the discovery of g-C_3N_4, little advancement has been made in adopting it for potential applications. Our survey has revealed some of the practical issues associated with g-C_3N_4, such as poor zero-band gap and absorptivity, among others. As a result, the development of g-C_3N_4 QDs has emerged as a significant driving force behind the increasing number of g-C_3N_4 applications, prompting extensive research efforts in their development. Previous research has shown that g-C_3N_4 QDs are becoming increasingly important as functional materials with potential applications in medicine, optics, energy, sensing, and catalysis. However, an adequate level of understanding of the property-performance relationship for g-C_3N_4 QDs is still lacking, which signifies the need for additional research on this topic. Nevertheless, due to the number of benefits that g-C_3N_4 QDs can bring in a variety of applications, this area of research has attracted a lot of interest from academics and industries in recent years.

Taking a look into the future, it is evident that the rapid advancement of g-C_3N_4 QDs synthesis and application will occupy a prominent position in the research of 0D materials. This will involve the development and production of high-performance g-C_3N_4 QD based materials. By leveraging collaborative efforts and synergistic cooperation across various research disciplines, it is possible to create highly advanced materials based on g-C_3N_4 QDs that exhibit promising characteristics. Last but not least, it is our belief that the field of g-C_3N_4 QDs research will continue to yield fascinating topics for exploration in the future, given the demonstrated utility of these nanomaterials across a wide range of domains. Anticipating the prospective utilization of g-C_3N_4 QDs, it appears that the enhancement of the g-C_3N_4 QDs preparation methodologies constitutes a pivotal factor in unveiling several intriguing prospects for this 0D material. Finally, it is our aspiration that this review will effectively accomplish its intended objective and function as a navigational tool for researchers in their pursuit of advancing the g-C_3N_4 QD chemistry toward the realization of compelling applications for this 0D nanomaterial.

Author information

Corresponding Authors

*Mohammed Majdoub - Email: **mmajdoub@olemiss.edu, simajdoub@gmail.com**
* Dineshkumar Sengottuvelu - Email: **dsengott@olemiss.edu, dineshchemsrkv@gmail.com**

ORCID

Mohammed Majdoub: 0000-0002-5674-0089

Dineshkumar Sengottuvelu: 0000-0002-5110-450X

Sasan Nouranian: 0000-0002-8319-2786

Ahmed Al-Ostaz: 0000-0003-3101-5996

Authors Contributions

Mohammed Majdoub - Conceptualization, Formal analysis, Methodology, Validation, Investigation, Writing- Original Draft, Review & Editing; **Dineshkumar Sengottuvelu -** Conceptualization, Formal analysis, Methodology, Validation, Investigation, Writing- Original Draft; Review & Editing; **Sasan Nouranian -** Funding acquisition, Validation; Visualization, Review & Editing; **Ahmed Al-Ostaz -** Project administration**,** Funding acquisition**,** Validation; Visualization, Review & Editing.

Conflicts of interest

There are no conflicts to declare.

Acknowledgment

The authors acknowledge partial support provided for this work by the U.S. Army Engineer Research and Development Center (ERDC) and the Military Engineering Research and Development Area under contract W912HZ21C0040. Permission to publish was granted by the ERDC Geotechnical and Structures Laboratory. The authors also acknowledge partial support for this work by the U.S. Department of Energy under grant DE-SC0024072.

Funding

The work herein was funded partially under CA BO340 497014 Project, “Graphene Applications for Military Engineering,” under Contract W912HZ21C0040, and managed by the U.S. Army Engineer Research and Development Center (ERDC), and partially under grant DE-SC0024072 through the U.S. Department of Energy.

References

[1] D. Esposito, M. Antonietti, *Chem. Soc. Rev.* **2015**, *44*, 5821.

[2] F. H. Isikgor, C. R. Becer, *Polym. Chem.* **2015**, *6*, 4497.

[3] Y. Zheng, L. Lin, B. Wang, X. Wang, *Angew. Chemie Int. Ed.* **2015**, *54*, 12868.

[4] Y. Zhu, C. Romain, C. K. Williams, *Nature* **2016**, *540*, 354.

[5] D. Larcher, J. M. Tarascon, *Nat. Chem.* **2015**, *7*, 19.

[6] H. Xiang, R. Wang, J. Chen, F. Li, H. Zeng, *Light Sci. Appl.* **2021**, *10*, 1.

[7] T. M. Brenner, D. A. Egger, L. Kronik, G. Hodes, D. Cahen, *Nat. Rev. Mater.* **2016**, *1*, 1.

[8] M. Chhowalla, D. Jena, H. Zhang, *Nat. Rev. Mater.* **2016**, *1*, 1.

[9] X. Li, J. Yu, J. Low, Y. Fang, J. Xiao, X. Chen, *J. Mater. Chem. A* **2015**, *3*, 2485.

[10] V. Singh, Priyanka, P. V. More, E. Hemmer, Y. K. Mishra, P. K. Khanna, *Mater. Adv.* **2021**, *2*, 1204.

[11] S. Rahman, S. R. Al Ahmed, *Sol. Energy* **2021**, *230*, 605.

[12] X. Li, W. Xu, Y. Wang, X. Zhang, Z. Hui, H. Zhang, S. Wageh, O. A. Al-Hartomy, A. G. Al-Sehemi, *Appl. Mater. Today* **2022**, *28*, 101546.

[13] H. Zhou, Y. Sun, H. Yang, Y. Tang, Y. Lu, Z. Zhou, S. Cao, S. Zhang, S. Chen, Y. Zhang, H. Pang, H. Zhou, Y. Sun, H. Yang, Y. Tang, Y. Lu, Z. Zhou, S. Cao, S. Zhang, S. Chen, H. Pang, Y. Zhang, *Adv. Sci.* **2023**, *10*, 2303636.

[14] S. Liu, Z. Teng, H. Liu, T. Wang, G. Wang, Q. Xu, X. Zhang, M. Jiang, C. Wang, W. Huang, H. Pang, *Angew. Chemie - Int. Ed.* **2022**, *61*, e202207026.

[15] D. Sengottuvelu, A. K. Shaik, S. Mishra, H. Ahmad, M. Abbaszadeh, N. I. Hammer, S. Kundu, *ACS Omega* **2022**, *7*, 27742.

[16] M. Majdoub, Z. Anfar, A. Amedlous, *ACS Nano* **2020**, *14*, 12390.

[17] M. L. Cohen, *Phys. Rev. B* **1985**, *32*, 7988.

[18] J. Zhu, P. Xiao, H. Li, S. A. C. Carabineiro, *ACS Appl. Mater. Interfaces* **2014**, *6*, 16449.

[19] D. M. Teter, R. J. Hemley, *Science (80-.).* **1996**, *271*, 53.

[20] K. Maeda, X. Wang, Y. Nishihara, D. Lu, M. Antonietti, K. Domen, *J. Phys. Chem. C* **2009**, *113*, 4940.

[21] Y. Xu, S. P. Gao, *Int. J. Hydrogen Energy* **2012**, *37*, 11072.

[22] F. Dong, L. Wu, Y. Sun, M. Fu, Z. Wu, S. C. Lee, *J. Mater. Chem.* **2011**, *21*, 15171.

[23] S. Zhang, H. Gao, Y. Huang, X. Wang, T. Hayat, J. Li, X. Xu, X. Wang, *Environ. Sci. Nano*

2018, *5*, 1179.

[24] Y. Hong, E. Liu, J. Shi, X. Lin, L. Sheng, M. Zhang, L. Wang, J. Chen, *Int. J. Hydrogen Energy* **2019**, *44*, 7194.

[25] Y. Zhang, J. Liu, G. Wu, W. Chen, *Nanoscale* **2012**, *4*, 5300.

[26] K. Takanabe, K. Kamata, X. Wang, M. Antonietti, J. Kubota, K. Domen, *Phys. Chem. Chem. Phys.* **2010**, *12*, 13020.

[27] L. Yang, X. Liu, Z. Liu, C. Wang, G. Liu, Q. Li, X. Feng, *Ceram. Int.* **2018**, *44*, 20613.

[28] Q. Liu, X. Wang, Q. Yang, Z. Zhang, X. Fang, *Appl. Surf. Sci.* **2018**, *450*, 46.

[29] S. C. Yan, Z. S. Li, Z. G. Zou, *Langmuir* **2009**, *25*, 10397.

[30] X. Jiang, J. Li, J. Fang, L. Gao, W. Cai, X. Li, A. Xu, X. Ruan, *J. Photochem. Photobiol. A Chem.* **2017**, *336*, 54.

[31] W. J. Ong, L. L. Tan, Y. H. Ng, S. T. Yong, S. P. Chai, *Chem. Rev.* **2016**, *116*, 7159.

[32] A. Majdoub, M. Majdoub, S. Rafqah, H. Zaitan, *Environ. Sci. Pollut. Res.* **2023**, *30*, 85940.

[33] A. Amedlous, M. Majdoub, Z. Anfar, E. Amaterz, *Catal. 2021, Vol. 11, Page 1533* **2021**, *11*, 1533.

[34] M. Majdoub, A. Amedlous, Z. Anfar, A. Jada, *Adv. Mater. Interfaces* **2022**, *9*, 2200170.

[35] K. S. Lakhi, W. S. Cha, S. Joseph, B. J. Wood, S. S. Aldeyab, G. Lawrence, J. H. Choy, A. Vinu, *Catal. Today* **2015**, *243*, 209.

[36] Y. Wang, X. Wang, M. Antonietti, Y. Zhang, *ChemSusChem* **2010**, *3*, 435.

[37] M. Groenewolt, M. Antonietti, *Adv. Mater.* **2005**, *17*, 1789.

[38] P. Niu, L. Zhang, G. Liu, H. M. Cheng, *Adv. Funct. Mater.* **2012**, *22*, 4763.

[39] S. Patnaik, S. Martha, K. M. Parida, *RSC Adv.* **2016**, *6*, 46929.

[40] Y. Chen, F. Ding, A. Khaing, D. Yang, Z. Jiang, *Appl. Surf. Sci.* **2019**, *479*, 757.

[41] J. Barrio, L. Lin, P. Amo-Ochoa, J. Tzadikov, G. Peng, J. Sun, F. Zamora, X. Wang, M. Shalom, *Small* **2018**, *14*, 1800633.

[42] J. Barrio, M. Shalom, *ACS Appl. Mater. Interfaces* **2018**, *10*, 39688.

[43] T. Jordan, N. Fechler, J. Xu, T. J. K. Brenner, M. Antonietti, M. Shalom, *ChemCatChem* **2015**, *7*, 2826.

[44] Y. Yang, J. Chen, Z. Mao, N. An, D. Wang, B. D. Fahlman, *RSC Adv.* **2017**, *7*, 2333.

[45] L. Wang, G. Zhou, Y. Tian, L. Yan, M. Deng, B. Yang, Z. Kang, H. Sun, *Appl. Catal. B Environ.* **2019**, *244*, 262.

[46] M. Sumathi, A. Prakasam, P. M. Anbarasan, *J. Clust. Sci.* **2019**, *30*, 757.

[47] W. Wang, J. C. Yu, Z. Shen, D. K. L. Chan, T. Gu, *Chem. Commun.* **2014**, *50*, 10148.

[48] Z. Zhou, Y. Shen, Y. Li, A. Liu, S. Liu, Y. Zhang, *ACS Nano* **2015**, *9*, 12480.

[49] T. Wang, C. Nie, Z. Ao, S. Wang, T. An, *J. Mater. Chem. A* **2020**, *8*, 485.

[50] Y. Chen, X. Bai, *Catalysts* **2020**, *10*, 142.

[51] B. Kumru, D. Cruz, T. Heil, B. V. K. J. Schmidt, M. Antonietti, *J. Am. Chem. Soc.* **2018**, *140*, 17532.

[52] Y. Xu, X. Niu, H. Zhang, L. Xu, S. Zhao, H. Chen, X. Chen, *J. Agric. Food Chem.* **2015**, *63*, 1747.

[53] X. Zhang, H. Wang, H. Wang, Q. Zhang, J. Xie, Y. Tian, J. Wang, Y. Xie, *Adv. Mater.* **2014**, *26*, 4438.

[54] R. Guo, D. Zeng, Y. Xie, Y. Ling, D. Zhou, L. Jiang, W. Jiao, J. Zhao, S. Li, *Int. J. Hydrogen Energy* **2020**, *45*, 22534.

[55] H. R. Chen, W. M. Meng, R. Y. Wang, F. L. Chen, T. Li, D. D. Wang, F. Wang, S. E. Zhu, C. X. Wei, H. D. Lu, W. Yang, *Carbon N. Y.* **2022**, *190*, 319.

[56] S. R. Nxele, T. Nyokong, *Diam. Relat. Mater.* **2022**, *121*, 108751.

[57] J. Wang, S. Wang, *Coord. Chem. Rev.* **2022**, *453*, 214338.

[58] J. Zhou, Y. Yang, C. Y. Zhang, *Chem. Commun.* **2013**, *49*, 8605.

[59] F. Yuan, Y. K. Wang, G. Sharma, Y. Dong, X. Zheng, P. Li, A. Johnston, G. Bappi, J. Z. Fan, H. Kung, B. Chen, M. I. Saidaminov, K. Singh, O. Voznyy, O. M. Bakr, Z. H. Lu, E. H. Sargent, *Nat. Photonics* **2020**, *14*, 171.

[60] T. An, J. Tang, Y. Zhang, Y. Quan, X. Gong, A. M. Al-Enizi, A. A. Elzatahry, L. Zhang, G. Zheng, *ACS Appl. Mater. Interfaces* **2016**, *8*, 12772.

[61] D. Liu, S. H. Hur, J. S. Chung, W. M. Choi, *Appl. Sci.* **2020**, *10*, 1.

[62] D. Liu, T. Van Tam, W. M. Choi, *RSC Adv.* **2022**, *12*, 3561.

[63] P. Liu, Y. Sun, S. Wang, H. Zhang, Y. Gong, F. Li, Y. Shi, Y. Du, X. Li, S. shang Guo, Q. Tai, C. Wang, X. Z. Zhao, *J. Power Sources* **2020**, *451*, 227825.

[64] A. Y. Goren, Y. K. Recepoglu, V. Vatanpour, Y. Yoon, A. Khataee, *Environ. Res.* **2023**, *223*, 115408.

[65] G. Li, Z. Lian, W. Wang, D. Zhang, H. Li, *Nano Energy* **2016**, *19*, 446.

[66] S. Pattnayak, U. Sahoo, S. Choudhury, G. Hota, *Colloids Surfaces A Physicochem. Eng.*

Asp. **2022**, *648*, 129377.

[67] W. Tang, H. Liu, W. Zhu, X. Wei, *Carbon N. Y.* **2023**, *207*, 305.

[68] M. Zhang, Y. Zhang, L. Tang, G. Zeng, J. Wang, Y. Zhu, C. Feng, Y. Deng, W. He, *J. Colloid Interface Sci.* **2019**, *539*, 654.

[69] M. H. Chan, C. W. Chen, I. J. Lee, Y. C. Chan, D. Tu, M. Hsiao, C. H. Chen, X. Chen, R. S. Liu, *Inorg. Chem.* **2016**, *55*, 10267.

[70] H. Liu, X. Lv, J. Qian, H. Li, Y. Qian, X. Wang, X. Meng, W. Lin, H. Wang, *ACS Nano* **2020**, *14*, 13304.

[71] X. He, Y. Liu, C. J. Butch, B. R. Lee, F. Guo, J. Wu, Z. Wang, Q. Lu, J. H. Jeong, Y. Wang, S. H. Park, *Small* **2019**, *15*, 1902735.

[72] X. Lin, D. Xu, R. Zhao, Y. Xi, L. Zhao, M. Song, H. Zhai, G. Che, L. Chang, *Sep. Purif. Technol.* **2017**, *178*, 163.

[73] X. Chen, Q. Liu, Q. Wu, P. Du, J. Zhu, S. Dai, S. Yang, *Adv. Funct. Mater.* **2016**, *26*, 1719.

[74] X. Pang, H. Bian, W. Wang, C. Liu, M. S. Khan, Q. Wang, J. Qi, Q. Wei, B. Du, *Biosens. Bioelectron.* **2017**, *91*, 456.

[75] Y. Zhan, Z. Liu, Q. Liu, D. Huang, Y. Wei, Y. Hu, X. Lian, C. Hu, *New J. Chem.* **2017**, *41*, 3930.

[76] C. Z. Li, Z. B. Wang, X. L. Sui, L. M. Zhang, D. M. Gu, *RSC Adv.* **2016**, *6*, 32290.

[77] X. Lin, D. Xu, J. Zheng, M. Song, G. Che, Y. Wang, Y. Yang, C. Liu, L. Zhao, L. Chang, *J. Alloys Compd.* **2016**, *688*, 891.

[78] J. Wu, S. Yang, J. Li, Y. Yang, G. Wang, X. Bu, P. He, J. Sun, J. Yang, Y. Deng, G. Ding, X. Xie, *Adv. Opt. Mater.* **2016**, *4*, 2095.

[79] H. Yang, Z. Jin, H. Hu, G. Lu, Y. Bi, *Catalysts* **2017**, *7*, 99.

[80] Q. Zhang, X. Quan, H. Wang, S. Chen, Y. Su, Z. Li, *Sci. Rep.* **2017**, *7*, 1.

[81] Q. Zhang, H. Wang, S. Chen, Y. Su, X. Quan, *RSC Adv.* **2017**, *7*, 13223.

[82] C. Liu, J. Wang, S. Yang, X. Li, X. Lin, *RSC Adv.* **2019**, *9*, 8065.

[83] Q. Cheng, Y. He, Y. Ge, J. Zhou, G. Song, *Microchim. Acta* **2018**, *185*, 1.

[84] A. Bandyopadhyay, D. Ghosh, N. M. Kaley, S. K. Pati, *J. Phys. Chem. C* **2017**, *121*, 1982.

[85] Y. Yin, Y. Zhang, T. Gao, T. Yao, J. Han, Z. Han, Z. Zhang, Q. Wu, B. Song, *Mater. Chem. Phys.* **2017**, *194*, 293.

[86] N. Wang, H. Fan, J. Sun, Z. Han, J. Dong, S. Ai, *Carbon N. Y.* **2016**, *109*, 141.

[87] Q. Liu, D. Zhu, M. Guo, Y. Yu, Y. Cao, *Chinese Chem. Lett.* **2019**, *30*, 1639.

[88] S. Yousefzadeh, N. Morovati, *Int. J. Hydrogen Energy* **2020**, *45*, 33512.

[89] M. K. Albolkany, Y. Wang, W. Li, S. Arooj, C. H. Chen, N. Wu, Y. Wang, R. Zbořil, R. A. Fischer, B. Liu, *Angew. Chemie - Int. Ed.* **2020**, *59*, 21499.

[90] Y. Su, B. Sun, S. Chen, H. Yu, J. Liu, *RSC Adv.* **2017**, *7*, 14832.

[91] B. Sun, N. Lu, Y. Su, H. Yu, X. Meng, Z. Gao, *Appl. Surf. Sci.* **2017**, *394*, 479.

[92] H. Wang, X. Yuan, H. Wang, X. Chen, Z. Wu, L. Jiang, W. Xiong, G. Zeng, *Appl. Catal. B Environ.* **2016**, *193*, 36.

[93] X. Wang, L. Wang, F. Zhao, C. Hu, Y. Zhao, Z. Zhang, S. Chen, G. Shi, L. Qu, *Nanoscale* **2015**, *7*, 3035.

[94] Q. Cui, J. Xu, X. Wang, L. Li, M. Antonietti, M. Shalom, *Angew. Chemie - Int. Ed.* **2016**, *55*, 3672.

[95] Q. Fang, B. Li, Y. Y. Li, W. Q. Huang, W. Peng, X. Fan, G. F. Huang, *Adv. Powder Technol.* **2019**, *30*, 1576.

[96] X. Pang, C. Cui, M. Su, Y. Wang, Q. Wei, W. Tan, *Nano Energy* **2018**, *46*, 101.

[97] W. Guan, W. Gu, L. Ye, C. Guo, S. Su, P. Xu, M. Xue, *Int. J. Nanomedicine* **2014**, *9*, 5071.

[98] H. Li, F. Q. Shao, H. Huang, J. J. Feng, A. J. Wang, *Sensors Actuators, B Chem.* **2016**, *226*, 506.

[99] S. Liu, J. Tian, L. Wang, Y. Luo, J. Zhai, X. Sun, *J. Mater. Chem.* **2011**, *21*, 11726.

[100] Q. Cheng, X. Liu, Y. He, Y. Ge, J. Zhou, G. Song, *J. Fluoresc.* **2019**, *29*, 719.

[101] R. Bayan, N. Karak, *ACS Omega* **2019**, *4*, 9219.

[102] S. Liu, L. Wang, J. Tian, J. Zhai, Y. Luo, W. Lu, X. Sun, *RSC Adv.* **2011**, *1*, 951.

[103] Y. Tang, Y. Su, N. Yang, L. Zhang, Y. Lv, *Anal. Chem.* **2014**, *86*, 4528.

[104] S. Barman, M. Sadhukhan, *J. Mater. Chem.* **2012**, *22*, 21832.

[105] X. Cao, J. Ma, Y. Lin, B. Yao, F. Li, W. Weng, X. Lin, *Spectrochim. Acta - Part A Mol. Biomol. Spectrosc.* **2015**, *151*, 875.

[106] S. Liu, J. Tian, L. Wang, Y. Luo, X. Sun, *RSC Adv.* **2012**, *2*, 411.

[107] D. Xiao, D. Yuan, H. He, J. Lu, *Luminescence* **2013**, *28*, 612.

[108] H. Abdolmohammad-Zadeh, E. Rahimpour, *Sensors Actuators B Chem.* **2016**, *225*, 258.

[109] D. Xiao, S. Li, S. Liu, H. He, J. Lu, *New J. Chem.* **2016**, *40*, 320.

[110] S. Chen, N. Hao, D. Jiang, X. Zhang, Z. Zhou, Y. Zhang, K. Wang, *J. Electroanal. Chem.*

2017, *787*, 66.

[111] X. Fan, Y. Su, D. Deng, Y. Lv, *RSC Adv.* **2016**, *6*, 76890.

[112] X. Fan, Y. Feng, Y. Su, L. Zhang, Y. Lv, *RSC Adv.* **2015**, *5*, 55158.

[113] G. Bai, Z. Song, H. Geng, D. Gao, K. Liu, S. Wu, W. Rao, L. Guo, J. Wang, *Adv. Mater.* **2017**, *29*, 1606843.

[114] J. Su, L. Zhu, P. Geng, G. Chen, *J. Hazard. Mater.* **2016**, *316*, 159.

[115] P. Fageria, S. Uppala, R. Nazir, S. Gangopadhyay, C. H. Chang, M. Basu, S. Pande, *Langmuir* **2016**, *32*, 10054.

[116] J. Su, L. Zhu, G. Chen, *Appl. Catal. B Environ.* **2016**, *186*, 127.

[117] J. Yu, J. Lei, L. Wang, C. Guillard, J. Zhang, Y. Liu, M. Anpo, *Res. Chem. Intermed.* **2019**, *45*, 4237.

[118] M. S. Nasir, G. Yang, I. Ayub, S. Wang, W. Yan, *Appl. Surf. Sci.* **2020**, *519*, 146208.

[119] U. A. Rani, L. Y. Ng, C. Y. Ng, E. Mahmoudi, *Adv. Colloid Interface Sci.* **2020**, *278*, 102124.

[120] A. Ghaffarkhah, E. Hosseini, M. Kamkar, A. A. Sehat, S. Dordanihaghighi, A. Allahbakhsh, C. van der Kuur, M. Arjmand, *Small* **2022**, *18*, 2102683.

[121] Y. Yan, J. Gong, J. Chen, Z. Zeng, W. Huang, K. Pu, J. Liu, P. Chen, *Adv. Mater.* **2019**, *31*, 1808283.

[122] H. Wang, X. Yuan, H. Wang, X. Chen, Z. Wu, L. Jiang, W. Xiong, G. Zeng, *Appl. Catal. B Environ.* **2016**, *193*, 36.

[123] X. Wu, L. Yang, L. Luo, G. Shi, X. Wei, F. Wang, *ACS Appl. Bio Mater.* **2019**, *2*, 1998.

[124] H. He, J. Li, Y. Liu, Q. Liu, F. Zhan, Y. Li, W. Li, J. Wen, *Nano* **2017**, *12*, 1750064.

[125] K. Patir, S. K. Gogoi, *ACS Sustain. Chem. Eng.* **2018**, *6*, 1732.

[126] S. Liu, J. Tian, L. Wang, Y. Luo, X. Sun, *RSC Adv.* **2011**, *2*, 411.

[127] O. J. Achadu, N. Revaprasadu, *Microchim. Acta* **2018**, *185*, 1.

[128] S. Gu, C. Te Hsieh, Y. Ashraf Gandomi, J. K. Chang, J. Li, J. Li, H. Zhang, Q. Guo, K. C. Lau, R. Pandey, *J. Mater. Chem. C* **2019**, *7*, 5468.

[129] T. Yuan, F. Yuan, X. Li, Y. Li, L. Fan, S. Yang, *Chem. Sci.* **2019**, *10*, 9801.

[130] W.-B. Luo, S.-L. Chou, J.-Z. Wang, Y.-C. Zhai, H.-K. Liu, *Small* **2015**, *11*, 2817.

[131] X. Chen, Q. Liu, Q. Wu, P. Du, J. Zhu, S. Dai, S. Yang, *Adv. Funct. Mater.* **2016**, *26*, 1719.

[132] R. Bai, H. Sun, P. Jin, J. Li, A. Peng, J. He, *RSC Adv.* **2021**, *11*, 24892.

[133] J. Xu, L. Zhang, R. Shi, Y. Zhu, *J. Mater. Chem. A* **2013**, *1*, 14766.

[134] Z. Xing, K. Dong, N. Pavlopoulos, Y. Chen, L. Amirav, *Angew. Chemie - Int. Ed.* **2021**, *60*, 19413.

[135] M. K. Bhunia, K. Yamauchi, K. Takanabe, *Angew. Chemie Int. Ed.* **2014**, *53*, 11001.

[136] K. Schwinghammer, M. B. Mesch, V. Duppel, C. Ziegler, J. Senker, B. V. Lotsch, *J. Am. Chem. Soc.* **2014**, *136*, 1730.

[137] G. Liao, S. Chen, X. Quan, H. Yu, H. Zhao, *J. Mater. Chem.* **2012**, *22*, 2721.

[138] Y.-C. Lu, J. Chen, A.-J. Wang, N. Bao, J.-J. Feng, W. Wang, L. Shao, *J. Mater. Chem. C* **2015**, *3*, 73.

[139] Q. Cui, J. Xu, X. Wang, L. Li, M. Antonietti, M. Shalom, *Angew. Chemie Int. Ed.* **2016**, *55*, 3672.

[140] R. Sekiya, Y. Uemura, H. Murakami, T. Haino, *Angew. Chemie Int. Ed.* **2014**, *53*, 5619.

[141] Y. J. Chung, B. Il Lee, J. W. Ko, C. B. Park, *Adv. Healthc. Mater.* **2016**, *5*, 1560.

[142] M. Li, B. Wang, X. An, Z. Li, H. Zhu, B. Mao, D. G. Calatayud, T. D. James, *Dye. Pigment.* **2019**, *170*, 107476.

[143] S. Stankovich, D. A. Dikin, R. D. Piner, K. A. Kohlhaas, A. Kleinhammes, Y. Jia, Y. Wu, S. T. Nguyen, R. S. Ruoff, *Carbon N. Y.* **2007**, *45*, 1558.

[144] Z. Song, T. Lin, L. Lin, S. Lin, F. Fu, X. Wang, L. Guo, *Angew. Chemie Int. Ed.* **2016**, *55*, 2773.

[145] A. Kundu, B. Park, J. Oh, K. V. Sankar, C. Ray, W. S. Kim, S. Chan Jun, *Carbon N. Y.* **2020**, *156*, 110.

[146] X. Lu, H. Qin, J. Cai, Y. Cui, L. Liao, F. Lv, C. Zhu, L. Wang, J. Liu, L. Long, W. Kong, F. Liu, *Nanomaterials* **2022**, *12*, DOI 10.3390/nano12162804.

[147] J. Dong, Y. Zhao, H. Chen, L. Liu, W. Zhang, B. Sun, M. Yang, Y. Wang, L. Dong, *New J. Chem.* **2018**, *42*, 14263.

[148] L. Yang, A. Qin, S. Chen, L. Liao, J. Qin, K. Zhang, *RSC Adv.* **2018**, *8*, 5902.

[149] C.-Z. Li, Z.-B. Wang, X.-L. Sui, L.-M. Zhang, D.-M. Gu, *RSC Adv.* **2016**, *6*, 32290.

[150] P. Yadav, S. T. Nishanthi, B. Purohit, A. Shanavas, K. Kailasam, *Carbon N. Y.* **2019**, *152*, 587.

[151] H. Liu, X. Wang, H. Wang, R. Nie, *J. Mater. Chem. B* **2019**, *7*, 5432.

[152] T. Gao, X. Wang, L. Y. Yang, H. He, X. X. Ba, J. Zhao, F. L. Jiang, Y. Liu, *ACS Appl.*

Mater. Interfaces **2017**, *9*, 24846.

[153] Y. Yan, J. Chen, N. Li, J. Tian, K. Li, J. Jiang, J. Liu, Q. Tian, P. Chen, *ACS Nano* **2018**, *12*, 3523.

[154] F. Yuan, Z. Wang, X. Li, Y. Li, Z. Tan, L. Fan, S. Yang, *Adv. Mater.* **2017**, *29*, DOI 10.1002/adma.201604436.

[155] H. Wang, C. Qian, Z. Yi, L. Rao, H. Liu, S. Zeng, **2013**, *2013*.

[156] J. Wang, F. Peng, Y. Lu, Y. Zhong, S. Wang, M. Xu, X. Ji, Y. Su, L. Liao, Y. He, *Adv. Opt. Mater.* **2015**, *3*, 103.

[157] W. Wang, S. Xu, N. Li, Z. Huang, B. Su, X. Chen, *Spectrochim. Acta - Part A Mol. Biomol. Spectrosc.* **2019**, *221*, DOI 10.1016/j.saa.2019.117211.

[158] L. Tang, R. Ji, X. Cao, J. Lin, H. Jiang, X. Li, K. S. Teng, C. M. Luk, S. Zeng, J. Hao, S. P. Lau, *ACS Nano* **2012**, *6*, 5102.

[159] M. M. Xavier, N. N. Adarsh, P. R. Nair, S. Mathew, *ACS Omega* **2021**, *6*, 22840.

[160] S. Liu, L. Wang, J. Tian, J. Zhai, Y. Luo, W. Lu, X. Sun, *RSC Adv.* **2011**, *1*, 951.

[161] D. Sengottuvelu, V. Kachwal, P. Raichure, T. Raghav, I. R. Laskar, *ACS Appl. Mater. Interfaces* **2020**, *12*, 31875.

[162] S. Dineshkumar, I. R. Laskar, *Polym. Chem.* **2018**, *9*, 5123.

[163] P. C. Raichure, V. Kachwal, D. Sengottuvelu, I. R. Laskar, *Macromolecules* **2022**, *55*, 10377.

[164] J. Wang, P. A. Tanner, *J. Am. Chem. Soc.* **2010**, *132*, 947.

[165] G. Chen, H. Liu, H. Liang, G. Somesfalean, Z. Zhang, *J. Phys. Chem. C* **2008**, *112*, 12030.

[166] M. Pollnau, D. R. Gamelin, S. R. Lüthi, H. U. Güdel, M. P. Hehlen, *Phys. Rev. B* **2000**, *61*, 3337.

[167] J. F. Suyver, A. Aebischer, S. García-Revilla, P. Gerner, H. U. Güdel, *Phys. Rev. B* **2005**, *71*, 125123.

[168] G. Chen, H. Qiu, P. N. Prasad, X. Chen, *Chem. Rev.* **2014**, *114*, 5161.

[169] D. Beljonne, Z. Shuai, G. Pourtois, J. L. Bredas, *J. Phys. Chem. A* **2001**, *105*, 3899.

[170] T. Lu, F. Chen, *J. Comput. Chem.* **2012**, *33*, 580.

[171] X. Ma, Y. Lv, J. Xu, Y. Liu, R. Zhang, Y. Zhu, *J. Phys. Chem. C* **2012**, *116*, 23485.

[172] G. Liu, P. Niu, C. Sun, S. C. Smith, Z. Chen, G. Q. (Max) Lu, H.-M. Cheng, *J. Am. Chem. Soc.* **2010**, *132*, 11642.

[173] Y. Zhang, T. Mori, J. Ye, M. Antonietti, *J. Am. Chem. Soc.* **2010**, *132*, 6294.

[174] A. Amedlous, M. Majdoub, E. Amaterz, Z. Anfar, A. Benlhachemi, *J. Photochem. Photobiol. A Chem.* **2021**, 113127.

[175] Y. Li, K. Lv, W. Ho, F. Dong, X. Wu, Y. Xia, *Appl. Catal. B Environ.* **2017**, *202*, 611.

[176] B. Sun, N. Lu, Y. Su, H. Yu, X. Meng, Z. Gao, *Appl. Surf. Sci.* **2017**, *394*, 479.

[177] M. Zarei, I. Mohammadzadeh, K. Saidi, H. Sheibani, *J. Mater. Sci. Mater. Electron.* **2021**, *32*, 26213.

[178] Z. Li, B. Li, S. Peng, D. Li, S. Yang, Y. Fang, *RSC Adv.* **2014**, *4*, 35144.

[179] T. Wang, X. Liu, Q. Men, W. Ma, Z. Liu, Y. Liu, C. Ma, P. Huo, Y. Yan, *Spectrochim. Acta Part A Mol. Biomol. Spectrosc.* **2019**, *213*, 19.

[180] M. Shorie, H. Kaur, G. Chadha, K. Singh, P. Sabherwal, *J. Hazard. Mater.* **2019**, *367*, 629.

[181] M. Yin, Y. Wan, S. Li, X. Zhao, W. Zhang, Y. Zhang, H. Wang, *J. Hazard. Mater.* **2021**, *408*, 124978.

[182] S. M. Hosseini, M. Ghiaci, H. Farrokhpour, *Mater. Res. Express* **2019**, *6*, 105079.

[183] M. Ghashghaee, Z. Azizi, M. Ghambarian, *Adsorption* **2020**, *26*, 429.

[184] Y. Li, J. Cai, F. Liu, H. Yu, F. Lin, H. Yang, Y. Lin, S. Li, *Microchim. Acta* **2018**, *185*, 1.

[185] H. Wang, Q. Lu, M. Li, H. Li, Y. Liu, H. Li, Y. Zhang, S. Yao, *Anal. Chim. Acta* **2018**, *1027*, 121.

[186] M. Rong, X. Song, T. Zhao, Q. Yao, Y. Wang, X. Chen, *J. Mater. Chem. C* **2015**, *3*, 10916.

[187] Q. Lu, H. Wang, Y. Liu, Y. Hou, H. Li, Y. Zhang, *Biosens. Bioelectron.* **2017**, *89*, 411.

[188] Y. L. T. Ngo, W. M. Choi, J. S. Chung, S. H. Hur, *Sensors Actuators B Chem.* **2019**, *282*, 36.

[189] Y. L. Thi Ngo, J. S. Chung, S. H. Hur, *Dye. Pigment.* **2019**, *168*, 180.

[190] J. Xian, Y. Weng, H. Guo, Y. Li, B. Yao, W. Weng, *Spectrochim. Acta Part A Mol. Biomol. Spectrosc.* **2019**, *215*, 218.

[191] O. J. Achadu, T. Nyokong, *Anal. Chim. Acta* **2017**, *991*, 113.

[192] O. J. Achadu, N. Revaprasadu, *Microchim. Acta* **2019**, *186*, 1.

[193] H. Wang, Q. Ma, Y. Wang, C. Wang, D. Qin, D. Shan, J. Chen, X. Lu, *Anal. Chim. Acta* **2017**, *973*, 34.

[194] X. Hu, J. Shi, Y. Shi, W. Li, M. Arslan, W. Zhang, X. Huang, Z. Li, Y. Xu, Y. Li, X. Zou, *Anal. Bioanal. Chem.* **2019**, *411*, 3341.

[195] H. Wang, Q. Chen, S. Zhou, *Chem. Soc. Rev.* **2018**, *47*, 4198.

[196] L. Chen, J. Song, *Adv. Funct. Mater.* **2017**, *27*, 1702695.

[197] E. Hutter, D. Maysinger, *Trends Pharmacol. Sci.* **2013**, *34*, 497.

[198] A. B. Foraker, C. M. Khantwal, P. W. Swaan, *Adv. Drug Deliv. Rev.* **2003**, *55*, 1467.

[199] A. Kundu, S. Nandi, R. K. Layek, A. K. Nandi, *ACS Appl. Mater. Interfaces* **2013**, *5*, 7392.

[200] F. Q. Schafer, G. R. Buettner, *Free Radic. Biol. Med.* **2001**, *30*, 1191.

[201] D. E. Hutter, B. G. Till, J. J. Greene, *Exp. Cell Res.* **1997**, *232*, 435.

[202] S. C. Lu, *Mol. Aspects Med.* **2009**, *30*, 42.

[203] L. Wang, C. Gong, Y. Shen, W. Ye, M. Xu, Y. Song, *Sensors Actuators B Chem.* **2017**, *242*, 625.

[204] H. Xie, Y. Fu, Q. Zhang, K. Yan, R. Yang, K. Mao, P. K. Chu, L. Liu, X. Wu, *Talanta* **2019**, *196*, 530.

[205] E. Makrantonaki, D. Jiang, A. M. Hossini, G. Nikolakis, M. Wlaschek, K. Scharffetter-Kochanek, C. C. Zouboulis, *Rev. Endocr. Metab. Disord. 2016 173* **2016**, *17*, 269.

[206] Y. Zhang, S. Meng, J. Ding, Q. Peng, Y. Yu, *Analyst* **2019**, *144*, 504.

[207] J. Chen, Y. Gao, X. Hu, Y. Xu, X. Lu, *Talanta* **2019**, *194*, 493.

[208] S. Pareek, S. Waheed, A. Rana, P. Sharma, S. Karak, *Nano Express* **2020**, *1*, DOI 10.1088/2632-959X/ab9b2f.

[209] L. Chen, D. Huang, S. Ren, T. Dong, Y. Chi, G. Chen, *Nanoscale* **2013**, *5*, 225.

[210] L. He, M. Fei, J. Chen, Y. Tian, Y. Jiang, Y. Huang, K. Xu, J. Hu, Z. Zhao, Q. Zhang, H. Ni, L. Chen, *Mater. Today* **2019**, *22*, 76.

[211] R. B. Fletcher, D. G. Lidzey, D. D. C. Bradley, S. Walker, M. Inbasekaran, E. P. Woo, *Synth. Met.* **2000**, *111–112*, 151.

[212] M.-C. Choi, Y. Kim, C.-S. Ha, *Prog. Polym. Sci.* **2008**, *33*, 581.

[213] F. Carpi, D. De Rossi, *Opt. Laser Technol.* **2006**, *38*, 292.

[214] C. R. Towns, I. Grizzi, M. Roberts, A. Wehrum, *J. Lumin.* **2007**, *122–123*, 976.

[215] A. Pron, P. Rannou, *Prog. Polym. Sci.* **2002**, *27*, 135.

[216] P.-A. Will, S. Reineke, in *Woodhead Publ. Ser. Electron. Opt. Mater.* (Ed.: O. B. T.-H. of O. M. for E. and P. D. (Second E. Ostroverkhova), Woodhead Publishing, **2019**, pp. 695–726.

[217] N. Aizawa, Y.-J. Pu, M. Watanabe, T. Chiba, K. Ideta, N. Toyota, M. Igarashi, Y. Suzuri,

H. Sasabe, J. Kido, *Nat. Commun.* **2014**, *5*, 5756.

[218] Q. Fu, J. Chen, C. Shi, D. Ma, *ACS Appl. Mater. Interfaces* **2012**, *4*, 6579.

[219] Y.-C. Lin, M. Karlsson, M. Bettinelli, *Top. Curr. Chem.* **2016**, *374*, 21.

[220] H. Zhang, J. A. Rogers, *Adv. Opt. Mater.* **2019**, *7*, 1800936.

[221] D. Chen, Y. Wada, Y. Kusakabe, L. Sun, E. Kayahara, K. Suzuki, H. Tanaka, S. Yamago, H. Kaji, E. Zysman-Colman, *Org. Lett.* **2023**, *25*, 998.

[222] P. Murto, S. Tang, C. Larsen, X. Xu, A. Sandström, J. Pietarinen, B. Bagemihl, B. A. Abdulahi, W. Mammo, M. R. Andersson, E. Wang, L. Edman, *ACS Appl. Energy Mater.* **2018**, *1*, 1753.

[223] P. Ledwon, *Org. Electron.* **2019**, *75*, 105422.

[224] K. Ji, M. Anaya, A. Abfalterer, S. D. Stranks, *Adv. Opt. Mater.* **2021**, *9*, 2002128.

[225] Y. Liu, Y. Dong, T. Zhu, D. Ma, A. Proppe, B. Chen, C. Zheng, Y. Hou, S. Lee, B. Sun, E. H. Jung, F. Yuan, Y. Wang, L. K. Sagar, S. Hoogland, F. P. García de Arquer, M.-J. Choi, K. Singh, S. O. Kelley, O. Voznyy, Z.-H. Lu, E. H. Sargent, *J. Am. Chem. Soc.* **2021**, *143*, 15606.

[226] L. Zhang, C. Sun, T. He, Y. Jiang, J. Wei, Y. Huang, M. Yuan, *Light Sci. Appl.* **2021**, *10*, 61.

[227] S. Dineshkumar, A. Raj, A. Srivastava, S. Mukherjee, S. S. Pasha, V. Kachwal, L. Fageria, R. Chowdhury, I. R. Laskar, *ACS Appl. Mater. Interfaces* **2019**, *11*, DOI 10.1021/acsami.9b07664.

[228] M. Xu, G. Yang, H. Bi, J. Xu, L. Feng, D. Yang, Q. Sun, S. Gai, F. He, Y. Dai, C. Zhong, P. Yang, *Chem. Eng. J.* **2019**, *360*, 866.

[229] S. Pandey, P. Choudhary, V. Gajbhiye, S. Jadhav, D. Bodas, *Cancer Nanotechnol.* **2023**, *14*, 30.

[230] U. Resch-Genger, M. Grabolle, S. Cavaliere-Jaricot, R. Nitschke, T. Nann, *Nat. Methods* **2008**, *5*, 763.

[231] W. Wu, G. C. Bazan, B. Liu, *Chem* **2017**, *2*, 760.

[232] P. Zhang, K. Qin, A. Lopez, Z. Li, J. Liu, *Anal. Chem.* **2022**, *94*, 15456.

[233] Q. Zhuang, P. Guo, S. Zheng, Q. Lin, Y. Lin, Y. Wang, Y. Ni, *Talanta* **2018**, *188*, 35.

[234] P. Y. Liyanage, R. M. Graham, R. R. Pandey, C. C. Chusuei, K. J. Mintz, Y. Zhou, J. K. Harper, W. Wu, A. H. Wikramanayake, S. Vanni, R. M. Leblanc, *Bioconjug. Chem.* **2019**,

30, 111.

[235] M. B. T.-B. A. R. Monici, Elsevier, **2005**, pp. 227–256.

[236] S. Zhu, Y. Song, X. Zhao, J. Shao, J. Zhang, B. Yang, *Nano Res.* **2015**, *8*, 355.

[237] M. Nurunnabi, Z. Khatun, K. M. Huh, S. Y. Park, D. Y. Lee, K. J. Cho, Y. K. Lee, *ACS Nano* **2013**, *7*, 6858.

[238] H. Lu, W. Li, H. Dong, M. Wei, *Small* **2019**, *15*, 1902136.

[239] X. Gao, Y. Cui, R. M. Levenson, L. W. K. Chung, S. Nie, *Nat. Biotechnol.* **2004**, *22*, 969.

[240] Y. Xing, Z. Xia, J. Rao, *IEEE Trans. Nanobioscience* **2009**, *8*, 4.

[241] B. Uprety, H. Abrahamse, *Front. Chem.* **2022**, *10*.

[242] J. Dong, Y. Zhao, K. Wang, H. Chen, L. Liu, B. Sun, M. Yang, L. Sun, Y. Wang, X. Yu, L. Dong, *ChemistrySelect* **2018**, *3*, 12696.

[243] J. Ge, Q. Jia, W. Liu, L. Guo, Q. Liu, M. Lan, H. Zhang, X. Meng, P. Wang, *Adv. Mater.* **2015**, *27*, 4169.

[244] H. Liu, C. Li, Y. Qian, L. Hu, J. Fang, W. Tong, R. Nie, Q. Chen, H. Wang, *Biomaterials* **2020**, *232*, 119700.

[245] W. Tao, X. Ji, X. Zhu, L. Li, J. Wang, Y. Zhang, P. E. Saw, W. Li, N. Kong, M. A. Islam, T. Gan, X. Zeng, H. Zhang, M. Mahmoudi, G. J. Tearney, O. C. Farokhzad, *Adv. Mater.* **2018**, *30*, 1870283.

[246] W. Tao, X. Ji, X. Xu, M. A. Islam, Z. Li, S. Chen, P. E. Saw, H. Zhang, Z. Bharwani, Z. Guo, J. Shi, O. C. Farokhzad, *Angew. Chemie Int. Ed.* **2017**, *56*, 11896.

[247] X. Ji, N. Kong, J. Wang, W. Li, Y. Xiao, S. T. Gan, Y. Zhang, Y. Li, X. Song, Q. Xiong, S. Shi, Z. Li, W. Tao, H. Zhang, L. Mei, J. Shi, *Adv. Mater.* **2018**, *30*, 1870268.

[248] J. Zhou, Y. Yang, C. Y. Zhang, *Chem. Commun.* **2013**, *49*, 8605.